

**RESOLUTION OF THE CONTROL ROD CUSPING PROBLEM
FOR NODAL METHODS**

by

Han-Sem Joo

B.S., Seoul National University
(1972)

M.E., Texas A&M University
(1980)

Submitted to the Department of Nuclear Engineering
in Partial Fulfillment of the Requirements for the
Degree of

DOCTOR OF PHILOSOPHY

at the

MASSACHUSETTS INSTITUTE OF TECHNOLOGY

February 1984

© Massachusetts Institute of Technology 1984

Signature of Author _____
Department of Nuclear Engineering
January 12, 1984

Certified by _____
Professor Allan F. Henry,
Thesis Supervisor

Accepted by _____
Professor Allan F. Henry,
Chairman, Departmental Graduate Committee
MASSACHUSETTS INSTITUTE
OF TECHNOLOGY ARCHIVES

APR 09 1984

LIBRARIES

RESOLUTION OF THE CONTROL ROD CUSPING PROBLEM
FOR NODAL METHODS

by

HAN-SEM JOO

Submitted to the Department of Nuclear Engineering
on January 12, 1984 in partial fulfillment of the
requirements for the degree of Doctor of Philosophy in
Nuclear Engineering

ABSTRACT

The objective of this research is to develop an accurate, systematic, inexpensive and reliable procedure for resolving the control rod cusping problem for nodal methods in light water reactor calculations. This cusping problem arises if the presence of a control rod partially inserted in a large spatial mesh node is represented by homogeneous cross sections of magnitudes proportional to the volume of control rod material present. A plot of reactivity vs. control rod position then exhibits unphysical cusps as the rod is withdrawn from node to node.

It is first shown that the presence of control rods partially inserted in a node accounted for by homogenized cross sections found by conventional procedures leads to incorrect nodal power distribution and reactor eigenvalue. Several new solution methods are then developed for determining accurate homogenization parameters for a partially rodded node: a tabulation-interpolation scheme, a volume-weighted cross section method, and an axial flux reconstruction scheme (called the Collector-Predictor method). The Collector-Predictor method can collect nodal solution information to predict the axial flux shape within a partially rodded node, and thereby determine flux-weighted cross sections and flux discontinuity factors.

The Collector-Predictor method is shown to be more accurate and systematic than the other schemes. It is incorporated into the QUANDRY nodal code, and tested for several benchmark problems. Results obtained are compared with those of conventional solution methods: for static problems, errors in eigenvalue and nodal power are reduced by a factor of 5 to 10, and for transient problems, they are reduced by a factor of ~10, the maximum error in power density being less than 2% in most cases. This method is found to be systematic, problem-independent, consistent and inexpensive for providing a satisfactory resolution of the control rod cusping problem.

Thesis Supervisor: Allan F. Henry
Title: Professor of Nuclear Engineering

ACKNOWLEDGEMENTS

I would like to express my sincere appreciation to many people who helped me to complete this thesis. Much advice, criticism and encouragement were forthcoming from my thesis supervisor, Professor Allan F. Henry. He has always listened to my questions, ideas and problems, and has answered with sound advice and intelligent guidance. I will not forget the extra time he took to analyze my work and writing. I would also like to thank him for the special effort he made to help me to obtain the financial aid for my study at M.I.T.

Appreciation is also extended to Professor Michael J. Driscoll who served as reader for this thesis and provided kind technical guidance and constructive criticism.

I am especially grateful to my parents for their devoted encouragement, financial support and praying for me throughout the period of my graduate studies. The love and emotional support provided by my sisters and brothers defy verbal description, and will always be remembered.

Lastly, but by no means least, my appreciation goes to my wife, who has assisted so much in the final preparation of this thesis, and our daughter Sharlene for their love and understanding.

TABLE OF CONTENTS

	<u>Page</u>
ABSTRACT.	2
ACKNOWLEDGEMENTS.	3
TABLE OF CONTENTS	4
LIST OF FIGURES	9
LIST OF TABLES.	12
Chapter 1. INTRODUCTION.	15
1.1 Motivation and Overview	15
1.2 Reactor Physics Solution Methods.	16
1.3 Nodal Methods	18
1.3.1 Heuristic Nodal Methods.	19
1.3.2 Systematic Nodal Methods	20
1.4 The Control Rod Cusping Problem	22
1.5 Objective and Summary	24
Chapter 2. NODAL EQUIVALENCE THEORY AND THE ANALYTIC NODAL METHOD.	26
2.1 Introduction.	26
2.2 Nodal Equivalence Theory.	27
2.2.1 Notation	27
2.2.2 Static Nodal Balance Equation.	28
2.2.3 Time-Dependent Nodal Equation.	36
2.3 Nodal Homogenization Parameters	41
2.3.1 Determination of the Parameters.	41
2.3.2 Approximate Methods.	43

TABLE OF CONTENTS
(continued)

	<u>Page</u>
2.4 The QUANDRY Nodal Model	48
2.4.1 Fundamental QUANDRY Equations.	49
2.4.2 The Theta Method and the Frequency Transformation Method.	53
2.4.3 The Application of QUANDRY to Light Water Reactor Analyses	56
2.5 Summary	57
 Chapter 3. THE CONTROL ROD CUSPING PROBLEM	 59
3.1 Introduction.	59
3.2 Causes of the Cusping Problem	59
3.2.1 Partially Rodded Node.	59
3.2.2 Homogenization Parameters for a Partially Rodded Node.	63
3.3 Conventional Solution Methods	66
3.3.1 Tabulation of the Cross Sections of the Partially Rodded Node.	66
3.3.2 Flux Expansion in Polynomials.	67
3.4 Equivalence Theory Approaches	70
3.4.1 Tabulation and Interpolation of the Homogenization Parameters.	74
3.4.2 Volume-Weighted Cross Sections and Axial Discontinuity Factors.	82
3.4.3 An Asymptotic Method	84
3.5 Summary	92

TABLE OF CONTENTS
(continued)

	<u>Page</u>
Chapter 4. THE COLLECTOR-PREDICTOR METHOD.	94
4.1 Introduction.	94
4.2 Description of Two Methods.	95
4.2.1 Method 1	95
4.2.2 Method 2	97
4.3 De-Homogenization and Prediction.	100
4.3.1 De-Homogenization Yielding the Axial Flux Shapes.	101
4.3.2 FWC and Axial Discontinuity Factors. .	106
4.3.3 Radial Discontinuity Factors	108
4.4 Transverse Leakage from a Partially Rodded Node	116
4.4.1 Finding Transverse Leakages for Two Subnodes of a Partially Rodded Node	116
4.4.2 Partially Rodded Surface-Nodes	122
4.5 The QUANDRY Code and the Collector-Predictor Method.	124
4.5.1 The QUANDRY Code	124
4.5.2 The Transient Routine and its Extension.	126
4.6 Summary	128
Chapter 5. APPLICATION OF THE COLLECTOR-PREDICTOR METHOD.	130
5.1 Introduction.	130
5.2 Three-Dimensional Models.	131

TABLE OF CONTENTS
(continued)

	<u>Page</u>
5.2.1 The CC3-PWR Model	131
5.2.2 BWR Models	134
5.3 Numerical Standards	140
5.3.1 Spatial Convergence	140
5.3.2 Temporal Stability	145
5.4 Application to Steady-State Problem	146
5.4.1 The CISE-BWR Problem	146
5.4.2 The TRD-BWR Problem	149
5.4.3 The CC3-PWR Problem	154
5.5 Time-Dependent Problems	160
5.5.1 The TRD-BWR Rod Drop	161
5.5.2 The CC3-PWR Rod Insertion	165
5.5.3 The CC3-PWR Rod Ejection	168
5.6 Summary	182
 Chapter 6. SUMMARY AND CONCLUSION	185
6.1 Overview of the Thesis	185
6.2 Results and Conclusion	187
6.3 Recommendations for Future Work	191
 REFERENCES	194

TABLE OF CONTENTS
(continued)

	<u>Page</u>
Appendix 1. The Homogenization Parameters for a Partially Rodded Node.	199
A1.1 Flux-Weighted Cross Sections for a 3 X 3 X 3 System	199
A1.2 Interpolations of the Axial Discontinuity Factors.	200
A1.2.1 A Cubic Polynomial Interpolation .	200
A1.2.2 A Cubic Spline Interpolation . . .	202
A1.3 Volume-Weighted Cross Sections and Corresponding Axial Discontinuity Factors.	203
Appendix 2. A Quadratic Expansion for Transverse Leakages and Corresponding Homogenized Surface Flux	208
A2.1 Expansion Coefficients for a Quadratic Transverse Leakage Approximation	208
A2.2 A Particular Solution for the Axial Flux .	209
A2.3 Homogenized Surface Flux	211
Appendix 3. Cross Sections and Mesh Layout for the CC3-PWR.	216
Appendix 4. Cross Sections and Mesh Layout for BWR Models	224
Appendix 5. Temporal Truncation Error for the CC3-PWR.	237

LIST OF FIGURES

<u>Figure</u>	<u>Page</u>
3.1 Partially rodded nodes	61
3.2 The cause of the control rod cusping (PWR)	64
3.3 A 3 X 3 X 3 node model with rodded central assembly surrounded by eight unrodded assemblies in symmetric layout	71
3.4 Relative difference of ΣFWC and ΣVWC vs. control rod tip position (h_c), and quadratically interpolated approximations. . . .	75
3.5 Interpolations of axial discontinuity factors at $h_c = 7.5$ and 15 cm for the PRN of a 3 X 3 X 3 node system	78
3.6 Axial discontinuity factors vs. control rod tip position, h_c , for three different axial node widths of the PRN of the 3 X 3 X 3 node system shown in Fig. 3.3a . . .	80
3.7 An asymmetric 3 X 3 X 3 system with three rodded assemblies.	83
3.8 Nodal variables of the PRN in a 3 X 3 X 3 symmetric system as a function of control rod tip position, h_c	89
4.1 Method 1 of the Collector-Predictor scheme . .	96
4.2 Method 2 of the Collector-Predictor scheme . .	99
4.3 Axial currents and average transverse leakages from the nodes in a rodded assembly	117
4.4 Average transverse leakage from the nodes in the rodded assembly of a 3 X 3 X 3 symmetric system	119
4.5 The Collector-Predictor method	127
5.1 Horizontal and vertical sections of the 4 X 4 X 8 CC3-PWR model.	132

LIST OF FIGURES
(continued)

<u>Figure</u>	<u>Page</u>
5.2 Four heterogeneous quarter-assemblies (a single complete assembly) for the CC3-PWR model.	133
5.3 The 3 X 3 X 3 CISE-BWR model	136
5.4 Core layout for the TRD-BWR.	137
5.5 Comparison of PDQ-7 and QUANDRY solutions for a two-dimensional, heterogeneous, rodded 2 X 4 nodal plane of the CC3-PWR. . . .	142
5.6 An axial configuration of the TRD-BWR with an internal PRN	152
5.7 Comparisons of k_{eff} and ΔP for the TRD-BWR.	152
5.8 An axial configuration of the TRD-BWR with a shallow PRN	155
5.9 Comparisons of k_{eff} and errors in nodal power for the TRD-BWR.	155
5.10 Comparisons of k_{eff} and nodal power of the CC3-PWR.	159
5.11 Comparison of transient power predictions for the TRD-BWR.	164
5.12 Total reactor power during a CC3-PWR transient.	171
5.13 Errors in total power predictions during a CC3-PWR transient.	172
5.14 Nodal power densities of the PRN during a CC3-PWR transient.	176
5.15 Differences in total power levels between 2 X 4 X 17 and 2 X 4 X 23 mesh calculations for a CC3-PWR transient.	179

LIST OF FIGURES
(continued)

<u>Figure</u>	<u>Page</u>
5.16 Normalized power distributions for the CC3-PWR model at time step 7 during a rod withdrawal	181
A3.1 The 16 X 32 mesh layout of rodded plane of the CC3-PWR model	217
A3.2 Axial mesh layout used to test unity axial discontinuity factors for the CC3-PWR benchmark problem.	222
A4.1 Heterogeneous quarter assembly of the TRD-BWR model	225
A4.2 Horizontal section of the TRD-BWR model	228
A5.1 Control rod tip position (z) vs. time steps for 2 X 4 X 17 CC3-PWR mesh system. . . .	238

LIST OF TABLES

<u>Table</u>	<u>Page</u>
3.1 Homogenized Nodal Cross Sections for 3 X 3 X 3 Node Models.	72
3.2 Comparison of 3 X 3 X 3 Symmetric System Calculations.	73
3.3 Discontinuity Factors of the PRN in Figure 3.3 as a Function of Control Rod Tip Position, h_C	77
3.4 Results of 3 X 3 X 3 Asymmetric Calcula- tions with FWC's and Discontinuity Factors of the Symmetric System.	83
3.5 Asymptotic Method Results of 3 X 3 X 3 Symmetric System Calculations.	91
4.1 The Volume-Flux-Weighted Radial Discon- tinuity Factors for a PRN of a 3 X 3 X 3 Symmetric System	113
4.2 Radial Discontinuity Factors for Three PRN's of a 3 X 3 X 3 Asymmetric System.	114
4.3 Test of the Use of Volume-Flux-Weighted Radial Discontinuity Factors (VFWRDF) along with FWC and Axial Discontinuity Factors.	115
5.1 Test Results for Method 1 and the Volume- Flux-Weighted Radial Discontinuity Factors (VFWRDF) for the CISE-BWR.	148
5.2 Comparisons of k_{eff} and Nodal Powers of a CISE-BWR Static Problem with Non-Uniform Control Blade Levels	150
5.3 Comparison of k_{eff} and Nodal Power Errors for a TRD-BWR Static Problem with an Internal PRN.	153
5.4 Comparison of k_{eff} and Nodal Power Errors for a TRD-BWR Static Problem with a PRN Next to the Bottom Reflector	156

LIST OF TABLES
(continued)

<u>Table</u>	<u>Page</u>
5.5 Error in k_{eff} and Maximum Nodal Power Error (ΔP) for the CC3-PWR Model	158
5.6 Comparison of Total Power Changes during a TRD-BWR Rod Drop Event	163
5.7 Comparisons of Power Levels for the CC3-PWR during Rod Insertion from 100 to 80 cm	166
5.8 Comparison of Total Reactor Power for a CC3-PWR Transient with a Control Rod Withdrawn from $z = 100$ cm to 120 cm.	169
5.9 Comparison of Nodal Power Density of the PRN for a CC3-PWR Transient with Control Rod Withdrawn from 100 cm to 120 cm	174
5.10 Comparison of Total Reactor Powers from Two Fine-Mesh QUANDRY Reference Solutions for a CC3-PWR Transient.	178
5.11 Axial Power Distributions for the CC3-PWR with the Rod Tip at 114 cm	180
A1.1 Flux-Weighted Cross Sections vs. Control Rod Tip Position for a Partially Rodded Node in a 3 X 3 X 3 System	199
A1.2 The Axial Discontinuity Factors Inter- polated by a Cubic Polynomial for a Partially Rodded Node in a 3 X 3 X 3 System	201
A1.3 The Axial Discontinuity Factors Inter- polated by a Natural Cubic Spline Func- tion for a Partially Rodded Node in a 3 X 3 X 3 System	204
A3.1 Heterogeneous, Two-Group Cross Sections for Pin Cells of the CC3-PWR	216
A3.2 Flux-Weighted Cross Sections and Radial Discontinuity Factors for the CC3-PWR.	218

LIST OF TABLES
(continued)

<u>Table</u>	<u>Page</u>
A3.3 Comparison of Nodal Power Densities from QUANDRY Solutions for the 2 X 4 X 8 and 2 X 4 X 22 Mesh Systems with Unity Axial Discontinuity Factors.	223
A4.1 AXS and ADF for the 3 X 3 X 3 CISE Model . . .	224
A4.2 Heterogeneous, Two-Group Cross Sections for the TRD-BWR Model.	226
A4.3 FWC and ADF of Nodes of the TRD-BWR Model. FWC and ADF are Found from Two-Dimensional 24 X 24 Fine-Mesh Calculations	229
A5.1 Delayed-Neutron Data	239
A5.2 Comparison of Total Power Transient for CC3-PWR for Different Time Step Sizes.	240
A5.3 Comparisons of Total Power for CC3-PWR Transient for Time Step = 2.5 msec	241

Chapter 1

INTRODUCTION

1.1 Motivation and Overview

Accurate information about the behavior and distribution in space, energy and time of the neutron population in a nuclear reactor is essential for design and operation. Such knowledge is required for reactor safety studies, fuel management strategies and reactor thermal hydraulics analyses. Consequently, there continues to be a strong economic and safety incentive to develop efficient computational methods for accurate prediction of neutron behavior for a variety of situations throughout reactor lifetime. Accordingly, various kinds of computational methods have been developed to predict multi-dimensional, time-dependent neutron behavior in reactors. The accurate predictions of reactor behavior by rigorous, exact computational methods are costly (and thus impractical) because they involve the determination of three-dimensional power distributions throughout a large and often geometrically complicated reactor core. Thus, more efficient methods are desirable [L-1].

Unfortunately, many of the more efficient methods being used rely on empirical adjustments to improve accuracy. As a result they may fail to predict accurate solutions if they are applied to three-dimensional, kinetic problems

involving control rod motion. The purpose of the present study is to investigate the dependence of homogenization parameters on control rod motion, and then to develop systematic and reliable procedures for accurate prediction of transient reactor power level and control rod reactivity worths in light water reactors. The detailed problem will be explained later in this chapter after a review of computational solution methods is given.

1.2 Reactor Physics Solution Methods

Extremely accurate neutron behavior in a reactor is described by the Boltzmann transport equation. The solution of this equation gives the directional flux density. However, finding numerical values of the directional flux density as a function of energy, position and time is a practical impossibility except for a few simplified special cases. Hence, the variables have to be discretized to solve the transport equation numerically. The energy range and time variable can be discretized in a straightforward manner. On the other hand, the spatial variables (angle and space) can be treated by several methods. The different ways of dealing with the spatial variables have given rise to well-known methods such as the discrete-ordinates (S_N) method, the Monte Carlo method, a Fourier-transform approach and the spherical-

harmonics (P_N) method [H-1].

If one is interested in relatively strong local flux variations within small systems, the size of a pin-cell, the method of collision probabilities can be applied. For intermediate-sized systems, such as a fuel assembly, it is advantageous to use a low-order S_N method or a Monte Carlo method. For reactor design the P_N method for N greater than 1 is of little value as it involves numerically complicated equations for geometries of practical importance.

Fortunately, the P_1 approximation is adequate for many purposes, and introduction of transport-corrected isotropic scattering into the P_1 approximation yields the diffusion equation. This is the most widely-used approximation to the transport equation, and is routinely solved by finite-difference approximations [C-1, F-1]. Its validity breaks down for strong flux gradients, but it is well suited for large systems. It can predict quite accurately group fluxes and interaction rates when averaged over artificially homogenized pin-cells, provided that cell homogenization methods are available and that the diffusion theory cross sections are known for every type of pin-cell.

For realistic reactor geometries, the large number of spatial meshes required for accuracy makes the finite-

difference method for solving the neutron diffusion equations quite inefficient and costly. As a result, a number of more efficient alternative methods have been developed. These include finite-element methods [S-1], spatial flux synthesis methods [S-2], response matrix methods [W-1], and nodal methods [D-1]. Except for the nodal methods, these schemes are not widely used for realistic, multi-dimensional reactor problems. There are a variety of reasons for this fact [H-1]. The overriding one is that the nodal methods appear to provide the best combination of economy and reliable accuracy.

1.3 Nodal Methods

For light water reactors (LWR's), for reasons of computational efficiency, reactor physics calculations start at the multi-group library group level with pin cells, then proceed in stages to larger areas with less spatial detail but higher dimensionality. In the final stage the number of neutron energy groups is reduced normally to one or two while spatially the core is divided into large homogenized nodes. A node is usually a vertical section of a fuel assembly or a quarter of this and its height is often chosen such that its shape is close to a cube. The essential idea of nodal methods is to relate neutron currents across an interface between two nodes

to the average flux levels in those two nodes [A-1]. The manner in which this relationship is derived distinguishes different nodal methods, and can fall into two classes: the first one is primarily heuristic, and the second is more systematic.

1.3.1 Heuristic Nodal Methods

In most of the simple and earlier nodal methods applied to LWR's, the inter-nodal coupling relationships are specified in the fast group only because of the important role of fast neutrons for inter-nodal coupling. The thermal group is (at best) appended as a correction, which leads to one-and-a-half ($1\frac{1}{2}$) group equations for each node. Nodal neutron populations are customarily coupled only to nearest neighbors. Thus, the inter-nodal currents are related to the nodal fluxes using escape kernels or fitting parameters. These kernels or parameters almost always need adjustment (tuning) so that their nodal solution matches a higher order reference solution. Among the tunable nodal programs are FLARE [D-2], TRILUX [G-1] and PRESTO [B-1]. The first two are based on the response matrix method and the last one involves a coarse-mesh model of the diffusion equation.

The advantages of the heuristic nodal methods include the small number of unknowns, low computer storage requirements, fast running time and accurate prediction of nodal

power distribution. Despite these advantages, their attractiveness is limited by the need for adjustment of the fitting parameters to improve accuracy. Adjusting the parameters requires experience and is costly, and some adjustments are strongly problem-dependent. Also errors in power prediction for some of the nodes (generally low power ones) can be in the range of 10-15%.

1.3.2 Systematic Nodal Methods

A straightforward mathematical manipulation of the conventional group diffusion equation can derive more systematic nodal diffusion theory schemes. These advanced methods depend on systematic procedures for determination of the nodal coupling relations. The first step in deriving most of the systematic nodal schemes is the same, and consists of reducing the three-dimensional neutron balance equation in each node to three auxiliary, one-dimensional, ordinary, differential equations which are needed to relate the nodal surface currents and nodal volume fluxes. One-dimensional equations are obtained for each direction by integrating over the two other transverse directions of the node, and as a consequence spatially dependent transverse leakage terms appear. The transverse leakage shapes in the modern systematic nodal methods are generally approximated by quadratic expansion across each node. Several variants of the systematic nodal methods can

be distinguished by different approximations for the transverse leakages and different methods used for solving the one-dimensional diffusion equations.

Several systematic nodal methods have been devised for light water reactors, and they include the QUABOX-CUBBOX model [L-2], the nodal expansion method [F-2], the nodal Green's function method [L-3] and the analytic nodal method [S-3, G-2, F-3].

The QUABOX-CUBBOX and nodal expansion methods expand the one-dimensional flux or interface current shapes as polynomials in the directional variable of interest, and the coefficients of the polynomials are determined by a weighted-residual procedure. The nodal Green's function and analytic nodal methods in effect solve analytically the one-dimensional diffusion equations with the transverse leakage approximated by quadratic polynomials. The analytic nodal method developed at M.I.T. and implemented in the QUANDRY code makes fewer approximations but accommodates only two energy groups, whereas the other methods are readily extendable. In this thesis the analytic nodal method will be used.

Smith [S-4, S-5] has shown that the QUANDRY model is capable of predicting accurate values of nodal fluxes in multi-dimensional problems with homogeneous nodes. Moreover, running time can be two or three orders of

magnitude shorter than that required for a finite-difference solution of the same accuracy. With two groups represented explicitly, problem running time should be about twice that of the conventional nodal codes. The QUANDRY model also has been applied with impressive accuracy both to heterogeneous two-dimensional problems and to homogeneous three-dimensional problems [C-2, F-4].

Another advantage of the QUANDRY model is that it can be extended directly to the analysis of transient problems [S-6], and it has been successfully tested against several homogeneous problems [S-4]. However, its accuracy for three-dimensional transient problems with both radial and axial heterogeneities has not been extensively studied. Smith encountered some difficulty with transient problems involving control rod motions, and has suggested further investigation.

1.4 The Control Rod Cusping Problem

When a reactor is represented by a nodal model, it is customary to homogenize the cross sections over a whole node. The presence of control rods partially inserted in a node causes an axial heterogeneity, and creates a homogenization problem. If the homogenized cross sections for the node are found by a simple volume-averaging procedure, the resultant nodal power distribution

and reactor multiplication factor are incorrect. The difficulty is particularly serious for transient problems during which a control rod is being withdrawn. This way of representing a partially rodded node leads to a phenomenon known as "the control rod cusping problem," so called because the curve of the change in reactivity or in power level versus control rod position exhibits unphysical cusps.

It is of course possible to circumvent this difficulty by requiring that there be horizontal nodal interface planes positioned at every control rod tip position. However, if one is dealing with part-length or stuck rods or is performing a search for the control rod bank position corresponding to the critical condition, this node size subdivision procedure can become complicated. For reactor transients during which control rods are moving, and particularly power-dependent feedback effects (due to Xe, Sm, thermal-hydraulics, etc.) are being accounted for, complications become even more severe. Thus, there is considerable motivation for locating axial nodal interfaces at fixed horizontal planes and dealing with the partially rodded node as a single homogenized node.

Because the modeling of the volume-weighted cross sections causes the control rod cusping problem, alternate models such as flux-weighted cross sections can be used

for nodes with partially inserted control rods. Smith [S-4] has examined an axial flux expansion method to determine the flux-weighted homogenized cross sections, and has found that flux expansion in quadratic polynomials reduces the control rod cusping error by ~50% in many cases. However, for some situations that amount of error is still uncomfortably large.

1.5 Objective and Summary

This chapter has considered the reactor physics calculations associated with the determination of the global distribution of neutrons in a reactor core. The solution of the neutron diffusion equations by the finite-difference method is standard. However, obtaining the full-core solution by this method is expensive and computationally inefficient, especially for transient situations. An excellent alternative is the analytic nodal method developed at M.I.T. and embodied in the QUANDRY code. Finally, the need was described for accurate methods of resolving the control rod cusping problem in QUANDRY transient calculation.

The objective of this thesis is to develop and examine accurate, reliable and systematic procedures for resolution of the control rod cusping problem. Solution methods are to be based on the analytic nodal method, and will

be incorporated into the QUANDRY code.

Chapter 2 reviews nodal equivalence theory and the analytic nodal method. Also the homogenization parameters based on equivalence theory and the QUANDRY nodal model are reviewed because of their importance to resolution of the control rod cusping problem. Extensive discussion of the control rod cusping problem is presented in Chapter 3. The causes of the cusping problem are analyzed, and several new solution methods based on equivalence theory are introduced. Chapter 4 describes a new solution scheme, called the Collector-Predictor method, developed for systematic determination of homogenization parameters of a partially rodded node. An overall procedure for incorporation of the Collector-Predictor method into QUANDRY model is explained there. In Chapter 5, the Collector-Predictor methods are employed to solve the control rod cusping problems in steady-state and transient calculations, and results are presented for several light water reactor benchmark problems. Finally, Chapter 6 gives a summary of the investigation and provides recommendations for future research.

Chapter 2

NODAL EQUIVALENCE THEORY AND THE ANALYTIC NODAL METHOD

2.1 Introduction

Analytic nodal method, nodal equivalence theory and node homogenization methods are discussed in this chapter. Equivalence theory and the node homogenization methods yield the equivalent homogenized parameters needed for nodal diffusion theory model. The nodal model is then used to predict criticality and nodal power distribution for light water reactors (LWR's).

First, nodal equivalence theory for both static and time-dependent cases is presented (Section 2). Then several homogenization methods based on nodal equivalence theory are discussed in Section 3. Finally, equations and approximations leading to the QUANDRY model will be reviewed along with various test results (Section 4). Although a more complete description of the analytic nodal method and the QUANDRY nodal balance equations was presented by Smith [S-4], the theory and the methods will be reviewed here because they are essential to an understanding of the control rod cusping problem and to the development of new solution methods.

2.2 Nodal Equivalence Theory

2.2.1 Notation

All the problems are treated in three-dimensional Cartesian geometry. The general notation x , y and z represents coordinate directions, while notation u , v and w is used to represent generalized coordinate subscripts of the coordinates x , y and z . The spatial domain of all problems is divided into a set of nodes. The node (i,j,k) is defined by

$$\begin{aligned}x &\in [x_i, x_{i+1}] \\y &\in [y_j, y_{j+1}] \\z &\in [z_k, z_{k+1}].\end{aligned}$$

The nodal mesh intervals are

$$\begin{aligned}h_x^i &= x_{i+1} - x_i \\h_y^j &= y_{j+1} - y_j \\h_z^k &= z_{k+1} - z_k\end{aligned}$$

and the nodal volume is

$$V_{i,j,k} = h_x^i h_y^j h_z^k.$$

The control rod cusping problem is known to be significant even in the case of steady-state calculations of a reactor with partially rodded nodes. Hence, the

steady-state neutron balance equations are discussed in the next section, followed by a discussion of the time-dependent equations.

2.2.2 Static Nodal Balance Equation

The steady-state Boltzmann transport equation [H-1] states an exact neutron balance in the phase volume $dEd\Omega dV$ around the point $(E, \underline{\Omega}, \underline{x})$ of phase space written as

$$\begin{aligned} & \underline{\Omega} \cdot \nabla \Psi(\underline{x}, \underline{\Omega}, E) + \Sigma_t(\underline{x}, E) \Psi(\underline{x}, \underline{\Omega}, E) \\ &= \int_0^\infty dE' \int d\Omega' \left[\frac{1}{k_{\text{eff}}} \sum_j \chi^j(E) v^j \Sigma_f^j(\underline{x}, E') + \right. \\ & \quad \left. \Sigma_s(\underline{x}, \underline{\Omega}' \rightarrow \underline{\Omega}, E' \rightarrow E) \right] \Psi(\underline{x}, \underline{\Omega}', E') \end{aligned} \quad (2.1)$$

where

$\Psi(\underline{x}, \underline{\Omega}, E)$ = directional flux density at point \underline{x} , direction $\underline{\Omega}$ and energy E ,

$\chi^j(E)$ = fission spectrum for isotope j at energy E ,

k_{eff} = reactor eigenvalue,

and the cross section notation is standard.

If we assume that the differential scattering term is a function only of the relative angle between the in-coming and out-going directions of neutron travel ($\mu_0 = \underline{\Omega}' \cdot \underline{\Omega}$) and neglect the isotope j for sake of notational simplicity, then one may integrate Eq. 2.1 over all directions of neutron travel and over an energy range $\Delta E_g \equiv E_{g+1} - E_g$

($g = 1, 2, \dots, G$) to obtain a set of formally exact G equations

$$\begin{aligned} \nabla \cdot \mathbf{j}_g(\mathbf{x}) + \sum_{g'} \mathbf{t}_{g'}(\mathbf{x}) \psi_{g'}(\mathbf{x}) \\ = \sum_{g'=1}^G \left(\frac{1}{k_{\text{eff}}} \chi_g \nu \Sigma_{f_{g'}}(\mathbf{x}) + \Sigma_{gg'}(\mathbf{x}) \right) \psi_{g'}(\mathbf{x}) \end{aligned} \quad (2.2)$$

where

$$\begin{aligned} \mathbf{j}_g(\mathbf{x}) &\equiv \int d\Omega \int_{\Delta E_g} \Psi(\mathbf{x}, \underline{\Omega}, E) dE \\ \psi_g(\mathbf{x}) &\equiv \int d\Omega \int_{\Delta E_g} \Psi(\mathbf{x}, \underline{\Omega}, E) dE \\ \Sigma_{\alpha g}(\mathbf{x}) \psi_g(\mathbf{x}) &\equiv \int d\Omega \int_{\Delta E_g} \Sigma_\alpha(\mathbf{x}, E) \Psi(\mathbf{x}, \underline{\Omega}, E) dE \quad (\alpha = t, f) \\ \chi_g &\equiv \int_{\Delta E_g} \chi(E) dE \\ \Sigma_{gg'}(\mathbf{x}) \psi_{g'}(\mathbf{x}) &\equiv \int_{\Delta E_g} dE \int_{\Delta E_{g'}} \left[\int_{-1}^1 \frac{d\mu_0}{2} \Sigma_s(\mathbf{x}, E' \rightarrow E, \mu_0) \int d\Omega' \right. \\ &\quad \left. \Psi(\mathbf{x}, \underline{\Omega}', E') \right] dE' \end{aligned}$$

The problem of finding the integrated cross-sections is not trivial. However, this problem will not be discussed here and it is assumed that these cross sections are known.

Integration of Eq. 2.2 over a nodal volume $V_{i,j,k}$, and application of the divergence theorem yield the exact nodal balance equation

$$\begin{aligned}
& h_y^j h_z^k \left(\hat{j}_g^x_{i+1,j,k} - \hat{j}_g^x_{i,j,k} \right) + \\
& h_x^i h_z^k \left(\hat{j}_g^y_{i,j+1,k} - \hat{j}_g^y_{i,j,k} \right) + \\
& h_x^i h_y^j \left(\hat{j}_g^z_{i,j,k+1} - \hat{j}_g^z_{i,j,k} \right) + \\
& v_{i,j,k} \sum_{g=1}^{G_{\text{eff}}} \hat{\psi}_{g,i,j,k} \\
& = v_{i,j,k} \sum_{g=1}^{G_{\text{eff}}} \left[\frac{1}{k_{\text{eff}}} \chi_g \left(\hat{\Sigma}_{f,g}^{i,j,k} + \hat{\Sigma}_{gg'}^{i,j,k} \right) \hat{\psi}_{g',i,j,k} \right] \quad (2.3)
\end{aligned}$$

where the node-averaged quantities are represented by a circumflex (^ or ̂), and are formally defined by

$$\hat{\psi}_{g,i,j,k} \equiv \frac{1}{v_{i,j,k}} \int_{v_{i,j,k}} \psi_g(\mathbf{x}) dV \quad (2.4)$$

$$\hat{\Sigma}_{\alpha g}^{i,j,k} \equiv \frac{1}{v_{i,j,k} \hat{\psi}_{g,i,j,k}} \int_{v_{i,j,k}} \Sigma_{\alpha g}(\mathbf{x}) \psi_g(\mathbf{x}) dV \quad (\alpha=t,f)$$

$$\hat{\Sigma}_{gg'}^{i,j,k} \equiv \frac{1}{v_{i,j,k} \hat{\psi}_{g',i,j,k}} \int_{v_{i,j,k}} \Sigma_{gg'}(\mathbf{x}) \psi_{g'}(\mathbf{x}) dV$$

$$\hat{j}_g^x_{i,j,k} \equiv \frac{1}{h_y^j h_z^k} \int_{y_j}^{y_{j+1}} dy \int_{z_k}^{z_{k+1}} dz j_g(x_i, y, z)$$

$$\left. \begin{aligned} \hat{j}_g_{i,j,k}^y &= \frac{1}{h_x^i h_z^k} \int_{x_i}^{x_{i+1}} dx \int_{z_k}^{z_{k+1}} dz j_g(x, y_j, z) \\ \hat{j}_g_{i,j,k}^z &= \frac{1}{h_x^i h_y^j} \int_{x_i}^{x_{i+1}} dx \int_{y_j}^{y_{j+1}} dy j_g(x, y, z_k) \end{aligned} \right\} \quad (2.5)$$

In a nodal approximation, because the variables of interest are the node-averaged quantities, the information content of the space dependent variables, $j_g(\underline{x})$, $\psi_g(\underline{x})$ and $\Sigma_\alpha g(\underline{x})$, is reduced even further by integrating over large nodes within which the heterogeneous properties are characterized by uniform "homogenized" cross sections in each node.

Let us consider a mathematical problem which is defined in the same domain as the real problem represented by Eq. 2.2 and has spatially uniform nodal cross sections. The governing balance equations for this problem are

$$\begin{aligned} \nabla \cdot \underline{J}_g(\underline{x}) + \bar{\Sigma}_{t_g} \phi_g(\underline{x}) \\ = \sum_{g'=1}^G \left[\frac{1}{k_{\text{eff}}} \chi_g v \bar{\Sigma}_{f_g} + \bar{\Sigma}_{gg'} \right] \phi_{g'}(\underline{x}) \end{aligned} \quad (2.6)$$

where the homogenized cross sections and the effective multiplication constant that results from their use are

labeled with a bar. Integrating over the nodal volume $V_{i,j,k}$ gives

$$\begin{aligned}
 & h_y^j h_z^k \left(\bar{j}_g^x_{i+1,j,k} - \bar{j}_g^x_{i,j,k} \right) + \\
 & h_x^i h_z^k \left(\bar{j}_g^y_{i,j+1,k} - \bar{j}_g^y_{i,j,k} \right) + \\
 & h_x^i h_y^j \left(\bar{j}_g^z_{i,j,k+1} - \bar{j}_g^z_{i,j,k} \right) + \\
 & v_{i,j,k} \sum_{g=1}^{G_{\text{eff}}} \bar{\Sigma}_{t_g}^{i,j,k} \phi_g^{i,j,k} \\
 & = v_{i,j,k} \sum_{g'=1}^{G_{\text{eff}}} \left(\frac{1}{k_{\text{eff}}} \chi_g v \sum_{f_g}^{i,j,k} + \sum_{gg'}^{i,j,k} \phi_{g'}^{i,j,k} \right)
 \end{aligned} \tag{2.7}$$

where the node-averaged flux and current are defined in analogy with Eqs. 2.4 and 2.5, respectively. Comparison of Eqs. 2.3 and 2.7 shows that if one wishes there to be a nodal equivalence condition such that the homogenized solution of Eq. 2.7 simultaneously reproduces the reactor eigenvalue, surface-averaged group currents and node-averaged group reaction rates provided by the exact nodal solution of Eq. 2.3, then it is sufficient to require the homogenized cross sections obey

$$\hat{\Sigma}_{\alpha g}^{i,j,k} = \sum_{\alpha g}^{i,j,k} \quad (\alpha = \text{all reactions}) \tag{2.8a}$$

and that the node-averaged group fluxes obey

$$\hat{\psi}_g^{i,j,k} = \phi_g^{i,j,k} \quad (2.8b)$$

When the homogenized cross sections and the homogenized nodal fluxes are restrained as in Eq. 2.8, adjacent nodes can be coupled to obtain the global nodal solution of the homogenized nodal problem by imposing continuity of the node-surface-averaged quantities. The continuity condition for the surface currents at the nodal interface is a physical requirement. However, because the problem under consideration is an artificially homogenized one, there is no reason that the homogenized node-surface-averaged fluxes should be continuous across the nodal interfaces. Nevertheless, some relationship between the face-averaged fluxes on the interface is still necessary for solving a global nodal problem.

One method which leads to an auxiliary equation from which the spatial coupling of Eq. 2.7 can be determined is to treat the directions one at a time. Since only the surface-averaged currents are to be preserved, Eq. 2.6 is first averaged over the two nodal dimensions transverse to each coordinate direction. If Fick's law is assumed to be true, then integration of Eq. 2.6 over the two directions transverse to the direction u of interest yields a one-dimensional second-order differential equation

for the homogenized flux shape in node (ℓ, m, n) :

$$-\bar{D}_{g_{\ell,m,n}}^{\ell,m,n} \frac{d^2}{du^2} \bar{\phi}_{g_{\ell,m,n}}^{\ell,m,n}(u) + \bar{\Sigma}_{t_g}^{\ell,m,n} \bar{\phi}_{g_{\ell,m,n}}^{\ell,m,n}(u) - \sum_{g'=1}^G \left[\frac{1}{k_{\text{eff}}} \chi_g v \bar{\Sigma}_{f_g}^{\ell,m,n} + \bar{\Sigma}_{gg'}^{\ell,m,n} \right] \bar{\phi}_{g'}^{\ell,m,n}(u) = -S_{g_{\ell,m,n}}^{v,w}(u) \quad (2.9)$$

where

$$\begin{aligned} \bar{\phi}_{g_{\ell,m,n}}^{\ell,m,n}(u) &= \frac{1}{h_v^m h_w^n} \int_{v_m}^{v_{m+1}} dv \int_{w_n}^{w_{n+1}} dw \bar{\phi}_g(x) \\ L_{g_{\ell,m,n}}^u(u) &= \frac{1}{h_w^n} \int_{v_m}^{v_{m+1}} dv \int_{w_n}^{w_{n+1}} \left[\frac{\partial}{\partial v} \bar{J}_g^v(x) \right] dw \\ S_{g_{\ell,m,n}}^{v,w}(u) &= \frac{1}{h_v^m} L_{g_{\ell,m,n}}^v(u) + \frac{1}{h_w^n} L_{g_{\ell,m,n}}^w(u) \end{aligned} \quad (2.10)$$

and the bars are used to represent homogenized quantities.

In the equation, $S_{g_{\ell,m,n}}^{v,w}(u)$ represents the net leakage rate in the directions transverse to direction u , and the nodal cross sections $\bar{\Sigma}_{ag}^{\ell,m,n}$ are equal to their reference counterparts. This nonhomogeneous differential equation could be easily solved for $\bar{\phi}_{g_{\ell,m,n}}(u)$ subject to proper boundary condition, if the right-hand side term $S_{g_{\ell,m,n}}^{v,w}(u)$ were known.

If, according to the equivalence condition, one of the boundary conditions is chosen to be $\hat{j}_{g_{\ell,m,n}}^u = \bar{J}_{g_{\ell,m,n}}^u$ on the u -directed faces of each node, then

$\bar{\phi}_{g_{\ell,m,n}}^{\ell,m,n}(u)$ preserves the continuity of the surface-averaged

currents. When integrated over h_u^l , the solution $\bar{\phi}_{g_{\ell,m,n}}^{-u}(u)$ is required to reproduce the exact node-averaged flux $\hat{\psi}_{g_{\ell,m,n}}^l$ and eigenvalue k_{eff} . However, there is no reason, in general, to expect the homogenized surface fluxes obtained by solving Eq. 2.9 for two adjacent nodes to be continuous at the nodal interface separating these two nodes. In fact, only by permitting this surface-averaged flux to be discontinuous can the results of the heterogeneous reference problem be reproduced.

One simple approach to specify this required discontinuity is to introduce two additional homogenization parameters in each node per direction per group. Based on the concept of the "heterogeneity factors" of Koebke [K-1], Smith [S-5] suggested the discontinuity of the homogenized surface-averaged fluxes be expressed in terms of discontinuity factors which are defined for node (ℓ, m, n) in each direction u as

$$f_{g_{\ell,m,n}}^{u+} = \frac{\hat{\psi}_{g_{\ell,m,n}}^l(u_{\ell+1})}{\bar{\phi}_{g_{\ell,m,n}}^{-u}(u_{\ell+1})} \quad (2.11a)$$

and

$$f_{g_{\ell,m,n}}^{u-} = \frac{\hat{\psi}_{g_{\ell,m,n}}^l(u_\ell)}{\bar{\phi}_{g_{\ell,m,n}}^{-u}(u_\ell)} \quad (2.11b)$$

where $\hat{\psi}_{g_{\ell,m,n}}^l(u_\ell)$ is the heterogeneous surface flux at u_ℓ .

These discontinuity factors are regarded as parameters needed to satisfy the equivalence condition described earlier. By virtue of the continuity of the heterogeneous surface-averaged fluxes at nodal interfaces, the relationship between homogenized surface-averaged fluxes across the interface at $u=u_\ell$ (separating nodes $(\ell-1,m,n)$ and (ℓ,m,n)) is required to satisfy

$$f_g^{u+}_{\ell-1,m,n} \bar{\phi}_g^u_{\ell-1,m,n}(u_\ell) = f_g^{u-}_{\ell,m,n} \bar{\phi}_g^u_{\ell,m,n}(u_\ell) \quad (2.12)$$

Thus, a complete set of homogenization parameters consists of flux-weighted cross sections and flux discontinuity factors. Once these parameters are determined for each node, the global homogenized problem (Eq. 2.9) can be solved for homogenized nodal solution which will preserve the following: reactor eigenvalue, group node-surface-averaged currents and group nodal reaction rates. A detailed discussion of the homogenization parameters will be presented after reviewing the time-dependent nodal equations in the next section.

2.2.3 Time-Dependent Nodal Equation

A set of space-and time-dependent neutron balance equations can be derived from the Boltzmann equation. These equations include delayed neutron and precursor

terms as follows:

$$\begin{aligned} \nabla \cdot J_g(x, t) + \sum_t t_g(x, t) \psi_g(x, t) \\ - \sum_{g'=1}^G \left[(1-\beta) \chi_g^P - \nu \sum_f f_{g'}(x, t) + \sum_{gg'} \gamma_{gg'}(x, t) \right] \psi_{g'}(x, t) \\ - \sum_{d=1}^N \lambda_d \chi_g^d C_d(x, t) = -\frac{1}{v_g} \frac{\partial}{\partial t} \psi_g(x, t) \end{aligned} \quad (2.13a)$$

$$\beta_d \sum_{g=1}^G \nu \sum_f f_g(x, t) \psi_g(x, t) - \lambda_d C_d(x, t) = \frac{\partial}{\partial t} C_d(x, t) \quad (2.13b)$$

$g = 1, 2, \dots, G$

$d = 1, 2, \dots, N$

where

C_d = density of delayed neutron precursor family d

χ_g^P = prompt fission neutron spectrum for group g

χ_g^d = delayed neutron spectrum for family d in group g

ν = mean number of neutrons emitted per fission

λ_d = decay constant for delayed neutron precursor family d

β_d = fractional yield of delayed neutron precursor family d per fission

$\beta = \sum_{d=1}^N \beta_d$ (N = number of delayed neutron precursor family)

v_g = neutron speed for group g

Other terms included in the equations are standard in reactor physics. The time-dependent nodal balance equations are found by integrating Eq. 2.13 over the volume of a node (i, j, k) . Integrating over (i, j, k) and imposing the equivalence conditions given in Eq. 2.8 yield

$$\begin{aligned}
 & h_y^j h_z^k \left[\bar{J}_g^x_{i+1,j,k}(t) - \bar{J}_g^x_{i,j,k}(t) \right] + \\
 & h_x^i h_z^k \left[\bar{J}_g^y_{i,j+1,k}(t) - \bar{J}_g^y_{i,j,k}(t) \right] + \\
 & h_x^i h_y^j \left[\bar{J}_g^z_{i,j,k+1}(t) - \bar{J}_g^z_{i,j,k}(t) \right] + v_{i,j,k} \sum_t \bar{\phi}_{g'}^{i,j,k}(t) \bar{\phi}_g^{i,j,k}(t) \\
 & -v_{i,j,k} \sum_{g'=1}^G \left[(1-\beta) \chi_g^P + v \sum_f \bar{\phi}_{g'}^{i,j,k}(t) + \sum_{gg'} \bar{\phi}_{g'}^{i,j,k}(t) \right] \bar{\phi}_{g'}^{i,j,k}(t) \\
 & -v_{i,j,k} \sum_{d=1}^N \lambda_d \chi_g^d \bar{C}_d^{i,j,k}(t) = -v_{i,j,k} \frac{1}{v_g} \frac{\partial}{\partial t} \bar{\phi}_g^{i,j,k}(t)
 \end{aligned}
 \tag{2.14a}$$

and

$$\beta_d \sum_{g=1}^G v \sum_f \bar{\phi}_{g'}^{i,j,k}(t) \bar{\phi}_g^{i,j,k}(t) - \lambda_d \bar{C}_d^{i,j,k}(t) = \frac{\partial}{\partial t} \bar{C}_d^{i,j,k}(t)
 \tag{2.14b}$$

where

$$\bar{C}_d^{i,j,k}(t) \equiv \frac{1}{v_{i,j,k}} \int_{x_i}^{x_{i+1}} dx \int_{y_j}^{y_{j+1}} dy \int_{z_k}^{z_{k+1}} dz C_d(x, y, z, t)$$

and other terms are defined in complete analogy with their steady-state counterparts.

A time-dependent, one-dimensional diffusion equation from which the spatial coupling of Eq. 2.14 can be determined can be derived in the same way as in the steady-state case with the time derivatives for each node replaced by

$$\frac{\partial}{\partial t} \bar{\phi}_{g_{\ell,m,n}}^u(u,t) = w_{g_{\ell,m,n}}^p(t) \bar{\phi}_{g_{\ell,m,n}}^u(u,t) \quad (2.15a)$$

$$\frac{\partial}{\partial t} \bar{c}_{d_{\ell,m,n}}^u(u,t) = w_{d_{\ell,m,n}}^d(t) \bar{c}_{d_{\ell,m,n}}^u(u,t) \quad (2.15b)$$

where

$$\bar{\phi}_{g_{\ell,m,n}}^u(u,t) \equiv \frac{1}{h_v^m h_w^n} \int_{v_m}^{v_{m+1}} dv \int_{w_n}^{w_{n+1}} dw \bar{\phi}_{g_{\ell,m,n}}(r, t)$$

$$\bar{c}_{d_{\ell,m,n}}^u(u,t) \equiv \frac{1}{h_v^m h_w^n} \int_{v_m}^{v_{m+1}} dv \int_{w_n}^{w_{n+1}} dw c_{d_{\ell,m,n}}(r, t)$$

Terms $w_{g_{\ell,m,n}}^p(t)$ and $w_{d_{\ell,m,n}}^d(t)$ represent the prompt flux and leakage extrapolation frequency magnitude and the delayed neutron precursor frequency magnitude for a node (ℓ, m, n) at time t . One of the practical methods for estimating frequencies will be presented in Section 2.4.

Assuming Fick's law and integrating a homogeneous counterpart of Eq. 2.13 over the two directions transverse to the direction u , one can obtain an equation for one-

dimensional flux $\bar{\phi}_{g_{\ell,m,n}}^u(u,t)$ within a node (ℓ,m,n) :

$$\begin{aligned}
 & -\bar{D}_{g_{\ell,m,n}}(t) \frac{d^2}{du^2} \bar{\phi}_{g_{\ell,m,n}}^u(u,t) + \left[\bar{\Sigma}_{t_g}^{\ell,m,n}(t) + \right. \\
 & \left. \frac{1}{v_g} w_{g_{\ell,m,n}}^p(t) \right] \bar{\phi}_{g_{\ell,m,n}}^u(u,t) - \left[\sum_{d=1}^N \frac{\lambda_d \beta_d x_g^d}{w_{\ell,m,n}^d(t) + \lambda_d} + \right. \\
 & \left. (1-\beta) x_g^p \right] \sum_{g'=1}^G v \bar{\Sigma}_{f_{g'}}^{\ell,m,n}(t) \bar{\phi}_{g',m,n}^u(u,t) \\
 & - \sum_{g'=1}^G \bar{\Sigma}_{gg'}^{\ell,m,n}(t) \bar{\phi}_{g',m,n}^u(u,t) = -S_{g_{\ell,m,n}}^{v,w}(u,t) \quad (2.16a)
 \end{aligned}$$

where $S_{g_{\ell,m,n}}^{v,w}(u,t)$ is the same as Eq. 2.10 except for its time dependence. Rewriting in two-group form for a homogenized node, we obtain (with $x_1=1.0$ and $x_2=0.0$)

$$\begin{aligned}
 & -\bar{D}_1(t) \frac{d^2}{du^2} \bar{\phi}_1(u,t) + \left[\bar{\Sigma}_{t_1}(t) + \frac{w_1^p}{v_1} \right] \bar{\phi}_1(u,t) \\
 & - \left[(1-\beta) + \sum_{d=1}^N \frac{\lambda_d \beta_d}{w_d(t) + \lambda_d} \right] \sum_{g'=1}^2 v \bar{\Sigma}_{f_{g'}}(t) \bar{\phi}_{g'}(u,t) = -S_1^{v,w}(u,t) \quad (2.16b)
 \end{aligned}$$

$$\begin{aligned}
 & -\bar{D}_2(t) \frac{d^2}{du^2} \bar{\phi}_2(u,t) + \left[\bar{\Sigma}_{t_2}(t) + \frac{w_2^p}{v_2} \right] \bar{\phi}_2(u,t) - \bar{\Sigma}_{21}(t) \bar{\phi}_1(u,t) \\
 & = -S_2^{v,w}(u,t) \quad (2.16c)
 \end{aligned}$$

The ordinary differential equation, Eq. 2.16, is the transient counterpart to the steady-state coupling equation, (2.9). For a fixed time t , Eq. 2.16 can be solved in the same manner as for the steady-state case, provided

that the prompt and delayed neutron frequencies w_g^p and w_g^d are known for each node. Discontinuity factors can again be introduced to couple neighboring nodes in an exact manner.

Thus, for either static or transient cases, the use of equivalence theory homogenization parameters can reproduce an exact reference solution, provided that an exact reference solution is used to determine the homogenized nodal cross sections and corresponding discontinuity factors (and also provided that time-dependent discontinuity factors are employed).

The next section deals with the methods for estimating these homogenization parameters without making use of an exact reference solution.

2.3 Nodal Homogenization Parameters

2.3.1 Determination of the Parameters

Equivalent nodal homogenization theory requires that the group parameters be spatially homogenized in such a way as to insure the preservation of reactor eigenvalue, nodal reaction rates and nodal surface currents.

In order to preserve the reaction rates while at the same time preserving volume-averaged fluxes, the exact homogenized cross sections must be defined as

$$\bar{\Sigma}_{\alpha g}^{\ell, m, n} = \frac{\int_{V_{\ell, m, n}} \Sigma_{\alpha g}(x) \psi_g(x) dV}{\int_{V_{\ell, m, n}} \psi_g(x) dV} \quad (2.17)$$

To evaluate integrations, the shape of the reference flux, represented by $\psi_g(x)$, must be known beforehand.

The homogenized diffusion coefficient can be estimated by

$$\bar{D}_g^{\ell, m, n} = \left[\frac{\int_{V_{\ell, m, n}} \frac{1}{D_g(x)} \psi_g(x) dV}{\int_{V_{\ell, m, n}} \psi_g(x) dV} \right]^{-1} \quad (2.18)$$

where $D_g(x)$ is heterogeneous diffusion coefficient. This approximation is based on the fact that the inverse of $D_g(x)$ is proportional to the group transport cross section. The expression cannot be justified theoretically. However, any errors introduced by its use can be accounted for by the use of the discontinuity factors [S-7].

If the exact reference flux, $\psi_g(x)$, is known, then one can use this flux to determine all homogenized nodal cross sections and diffusion coefficients in accordance with Eqs. 2.17 and 2.18, respectively. When the reference currents on the nodal surfaces are known in addition to the reference flux shapes, one can also find exact

values of the discontinuity factors. However, it is not practical to determine the exact reference solution for the full core geometry. Thus, for practical applications, approximations for determination of homogeneous cross sections and diffusion coefficients and surface flux discontinuity factors are necessary.

2.3.2 Approximate Methods

The determination of homogenized parameters is seen from Eqs. 2.17 and 2.18 to require knowledge of the exact reference reaction rates and information about heterogeneous fluxes. The most common approach to approximating reference flux shapes is to solve the diffusion equation within each local node with approximate boundary conditions. Two methods, the second more accurate but more expensive than the first, are currently in use.

The first method is simple and non-iterative. Typically $\psi_g(x)$ is found from two-dimensional, fine-mesh assembly calculation with zero net-current boundary conditions (provided that the nuclear compositions and physical dimensions are uniform in axial direction within a node). This is based upon the fact that the homogenized parameters are much more dependent on the compositions and dimensions of the particular heterogeneous node rather than the location of that node in the reactor. Thus, for each different kind of assembly, two-dimensional critical

flux shapes throughout that assembly are determined, and the resultant fluxes are integrated with the heterogeneous cross sections to find approximate homogenized cross sections. This type of homogenized cross section is called "assembly homogenized cross section (AXS)." The AXS can be used to solve the homogenized nodal equation, Eq. 2.9, for the homogenized flux shape in the interior of that node with the same zero net-current boundary conditions on all surfaces. The homogenized fluxes on the surfaces and the corresponding heterogeneous surface fluxes will determine the discontinuity factors of that node according to Eq. 2.11. The discontinuity factors determined in this manner are called "assembly discontinuity factors" (ADF). Even though these approximate parameters differ little from those found using the exact reference flux shapes, the precision obtained using them is for some situations only marginally acceptable [S-5]. The inaccuracies of AXS and ADF arise from the zero net-current boundary conditions imposed on the assembly interfaces. Because of this approximation, many of the inter-assembly effects are not taken into account.

To improve the accuracy of the homogenized parameters by taking inter-assembly effects into account, Hoxie [H-2] tested the use of extended assembly computations. He imposed the zero net-current boundary condition not

on the boundary of a single isolated assembly but on a cluster of assembly-sized regions consisting of the assembly in question and its nearest neighbors. He obtained greatly improved accuracy. This method can be applied to situations involving significant heterogeneities such as PWR (pressurized water reactor) core-baffle-reflector interfaces or BWR (boiling water reactor) fuel assemblies disturbed by control blades. However, the number and size of the auxiliary calculations required make this method unattractive.

Another alternative method for evaluation of the nodal homogenization parameters is to perform calculations with zero net-current boundary conditions imposed at color set boundaries. Color sets are assembly-sized regions composed of four quadrants of four adjacent assemblies. This approach is particularly useful for calculation of homogenization parameters for baffle-reflector nodes because the assembly calculation method cannot be applied to non-multiplying nodes such as baffle-reflector region. The imposition of zero net-current conditions across interior assembly planes is generally a better approximation than their imposition at assembly boundaries. Each color set computation can be used to obtain homogenization parameters for four quarter-assemblies. Khalil [K-2] applied the color set scheme to fuel depletion and detailed

flux reconstruction problems, and showed that color set calculation for homogenized baffle constants is a practical and accurate procedure. The main drawback of this method is the large number of color set calculations that must be run. However, its accuracy and usefulness for detailed flux reconstruction problems are major advantages.

The second method which has been developed for estimating homogenized equivalence parameters is an iterative scheme based on iterations between the global calculations and local fixed-source calculations. The basic idea is that if exact boundary conditions for an assembly were known, then a fixed-source local calculation could be performed to estimate exact homogenized parameters. To do this, we may devise an iterative scheme in which the boundary conditions needed for local calculation at each iteration are obtained from the global solution of the previous iteration.

Cheng [C-3] and Finck [F-5] in their iterative procedures made use of pre-tabulated response matrices in order to reduce the number of auxiliary fixed-source local calculations. They examined the use of surface-current response matrices (both partial and net currents) and surface-flux response matrices, and found that the results were often very good but do not appear to be totally consistent. Furthermore, Cheng found that the local-global

iteration process often failed to converge. The other drawback to the iterative scheme is the cost of determining the response matrices and storage problem if flux reconstruction is desired (However, once the response matrices are determined, a detailed heterogeneous flux shape can be found at a cost much less than that required for a full core finite-difference computations.).

Although these methods, either non-iterative or iterative method, have been applied efficiently with impressive accuracy to two- or three-dimensional problems with homogeneous nodes, their accuracy for three-dimensional problem with both radial and axial heterogeneities depends strongly on the axial homogenization parameters and axial node layout.

The simplest method for solving problems with axial heterogeneities is to choose the z-direction node boundaries to coincide with material discontinuities. In this manner, each node is relatively homogeneous in the axial direction and, consequently, homogenization procedures need only be applied in two dimensions. However, two-dimensional assembly shapes provide no systematic way of estimating surface flux discontinuity factors at node boundaries in z-direction. Fortunately, the choice of axial mesh boundaries at axial material discontinuities makes the assumption of homogenized axial flux continuity (i.e.,

unity discontinuity factor) at these boundaries a good approximation. Khalil [K-2] and Finck [F-5] tested PWR and BWR problems with unity discontinuity factors at axial node boundaries. In both tests, it was found that the use of unity discontinuity factors at an axial nodal interface where there is a significant change in assembly characteristics such as the tip of a control rod, seems satisfactory. Thus, in the course of the investigation of the control rod cusping problem, unity discontinuity factors will be considered at the axial faces of a node if the nodal interface coincides the material discontinuities. And either two-dimensional assembly calculations or a full plane fine-mesh calculation will be performed to determine node-wise homogenization parameters.

2.4 The QUANDRY Nodal Model

The nodal computer code QUANDRY, was developed to solve analytically the nodal equations corresponding to equivalence theory which was described in the previous section. QUANDRY determines the nodal solution using analytic methods for a two-energy-group model, with the group constants assumed to be spatially constant in each node. In this section it is assumed that these constants are known. The fundamental equations for the time-independent problem will first be presented. Then, for the time-dependent

solution, an explanation of a time integration scheme, the theta method, will follow. Previous test results for QUANDRY applied to LWR analyses also will be presented.

2.4.1 Fundamental QUANDRY Equations

There are two equations that are fundamental to equivalence theory upon which QUANDRY is based. These are:

1. The nodal neutron balance equation
2. The flux-current spatial coupling equations

The balance condition is stated by Eq. 2.7; it is an exact neutron balance relationship within each node and each energy group g ($g = 1, 2, \dots, G$), and can be rewritten in a matrix form for all nodes as

$$\begin{aligned} & h_y^j h_z^k ([\bar{J}_{i+1,j,k}^x] - [\bar{J}_{i,j,k}^x]) + h_x^i h_z^k ([\bar{J}_{i,j+1,k}^y] - [\bar{J}_{i,j,k}^y]) \\ & + h_x^i h_y^j ([\bar{J}_{i,j,k+1}^z] - [\bar{J}_{i,j,k}^z]) + v_{i,j,k} [\Sigma_{i,j,k}] [\bar{\phi}_{i,j,k}] \\ & = \frac{1}{k_{\text{eff}}} v_{i,j,k} [X] [\Sigma_f_{i,j,k}]^T [\bar{\phi}_{i,j,k}] \end{aligned} \quad (2.19)$$

where

$[\bar{J}_{\ell,m,n}^u]$ is a column vector of length G containing surface-averaged current across the surface at $u = u_\ell$,

$[\bar{\phi}_{i,j,k}]$ is a column vector of length G containing
 the average group flux for node (i,j,k) ,
 $\bar{\phi}_g^{i,j,k}$,
 $[\Sigma_{i,j,k}]$ is G X G matrix containing the total-minus-
 scattering cross section of a homogenized
 node (i,j,k) , $\bar{\Sigma}_{t_g}^{i,j,k} - \bar{\Sigma}_{gg'}^{i,j,k}$,
 $[\nu\Sigma_{f_{i,j,k}}]$ is a column vector of length G containing
 the $\nu\Sigma_{fg}^{i,j,k}$ for node (i,j,k) , and
 $[\chi]$ is a column vector of length G containing
 the neutron fission spectrum.

Solution of this neutron balance equation requires
 an additional relationship which can be derived from
 the second-order differential equations, Eq. 2.9. These
 equations are one-dimensional, and can be put into a
 matrix form as

$$\begin{aligned}
 & -[D_{\ell,m,n}] \frac{d^2}{du^2} [\bar{\phi}_{\ell,m,n}^u(u)] + \\
 & \left([\Sigma_{\ell,m,n}] - \frac{1}{k_{\text{eff}}} [\chi] [\nu\Sigma_{f_{\ell,m,n}}]^T \right) [\bar{\phi}_{\ell,m,n}^u(u)] \\
 & = [S_{\ell,m,n}^{v,w}(u)] \quad u=x,y,z
 \end{aligned} \tag{2.20}$$

where the matrices are defined with elements given in
 Eq. 2.10 as

- $[\bar{\phi}_{\ell,m,n}^u(u)]$ is a column vector of length G containing
 $\bar{\phi}_{g_{\ell,m,n}}^u(u)$,
 $[D_{\ell,m,n}]$ is a diagonal G X G matrix containing
 $\bar{D}_{g_{\ell,m,n}}^{\ell,m,n}$ and
 $[S_{\ell,m,n}^{v,w}(u)]$ is a column vector of length G containing
 $S_{g_{\ell,m,n}}^{v,w}(u)$.

Unfortunately, the shape of the net transverse leakage term, $[S_{\ell,m,n}^{v,w}(u)]$, is not known; only its average over u, $[\bar{S}_{\ell,m,n}^{v,w}]$, is known. Thus the spatial shape of the transverse leakage term must be approximated so that the spatial coupling equation can be solved for $[\bar{\phi}_{\ell,m,n}^u(u)]$. This approximation is the only approximation inherent in the analytic nodal method embedded in the QUANDRY. Two approximations have been examined: flat and quadratic. The flat transverse leakage is equal to its average value, and the quadratic shape is determined so that the integrals of the approximated shapes over a node of interest and its two adjacent nodes preserve the average transverse leakages of these three nodes. Thus, $[S_{\ell,m,n}^{v,w}(u)]$ is approximated as

$$\begin{aligned}
 [S_{\ell,m,n}^{v,w}(u)] &\approx [\bar{S}_{\ell-1,m,n}^{v,w}] \rho_{\ell-1}(u) + [\bar{S}_{\ell,m,n}^{v,w}] \rho_\ell(u) \\
 &\quad + [\bar{S}_{\ell+1,m,n}^{v,w}] \rho_{\ell+1}(u) \quad u = x, y, z
 \end{aligned} \tag{2.21}$$

where the expansion functions $\rho(u)$ are quadratic polynomials

in u , and are uniquely determined by mesh spacings in direction u .

Once the quadratic functions $\rho(u)$ are determined, solution of Eq. 2.20 is straightforward. Thus, one can obtain $[\bar{\phi}_{\ell,m,n}^u(u)]$ for any u in the interval u_ℓ to $u_{\ell+1}$ in terms of $[\bar{\phi}_{\ell,m,n}^u(u_{\ell+1})]$, $[\bar{J}_{\ell,m,n}^u(u_{\ell+1})]$, $[\bar{S}_{\ell-1,m,n}^{v,w}]$, $[\bar{S}_{\ell,m,n}^{v,w}]$, and $[\bar{S}_{\ell+1,m,n}^{v,w}]$. Integration of $[\bar{\phi}_{\ell,m,n}^u(u)]$ over u from u_ℓ to $u_{\ell+1}$ to obtain $[\bar{\bar{\phi}}_{\ell,m,n}]$ results in a linear relationship between the surface-averaged fluxes $[\bar{\phi}_{\ell,m,n}^u(u_{\ell+1})]$ and the other terms, $[\bar{J}_{\ell,m,n}^u(u_{\ell+1})]$, $[\bar{\bar{\phi}}_{\ell,m,n}]$, $[\bar{S}_{\ell-1,m,n}^{v,w}]$, $[\bar{S}_{\ell,m,n}^{v,w}]$ and $[\bar{S}_{\ell+1,m,n}^{v,w}]$. Similarly, one can obtain $[\bar{\phi}_{\ell+1,m,n}^u(u_{\ell+1})]$ in terms of $[\bar{J}_{\ell+1,m,n}^u(u_{\ell+1})]$, $[\bar{\bar{\phi}}_{\ell+1,m,n}]$, $[\bar{S}_{\ell,m,n}^{v,w}]$, $[\bar{S}_{\ell+1,m,n}^{v,w}]$, and $[\bar{S}_{\ell+2,m,n}^{v,w}]$ by integrating from $u_{\ell+1}$ to $u_{\ell+2}$. In equivalence theory, the flux discontinuity factors defined by Eq. 2.11 must be imposed at $u = u_{\ell+1}$ to eliminate the surface-averaged fluxes at $u = u_{\ell+1}$. On physical grounds, one may require surface current continuity,

$$[\bar{J}_{\ell,m,n}^u(u_{\ell+1})] = [\bar{J}_{\ell+1,m,n}^u(u_{\ell+1})]$$

to obtain nodal coupling equations relating the surface-averaged currents, $[\bar{J}_{\ell,m,n}^u(u_{\ell+1})]$, to the two volume-averaged fluxes, $[\bar{\bar{\phi}}_{\ell,m,n}]$ and $[\bar{\bar{\phi}}_{\ell+1,m,n}]$, four transverse leakages, $[\bar{S}_{\ell-1,m,n}^{v,w}]$, $[\bar{S}_{\ell,m,n}^{v,w}]$, $[\bar{S}_{\ell+1,m,n}^{v,w}]$ and $[\bar{S}_{\ell+2,m,n}^{v,w}]$, and the discontinuity factors at $u = u_{\ell+1}$.

By an analogous procedure one can find $[\bar{J}_{\ell,m,n}^u(u_\ell)]$. Thus we can express the net leakage rate, $([J_{\ell+1,m,n}^u] - [J_{\ell,m,n}^u])$, as a linear function of the volume-averaged fluxes, transverse leakages and discontinuity factors. Substituting this net leakage term into the nodal balance equation, Eq. 2.19, we can finally solve for volume-averaged fluxes $[\bar{\phi}_{i,j,k}]$ for all nodes of the time-independent nodal problem.

In the time-dependent nodal equations presented in the previous section, we found that the time-dependent volume-averaged fluxes $[\bar{\phi}_{i,j,k}(t)]$ can be determined through the same procedure as for the time-independent case if the solutions are desired only at discrete time steps. However, the temporal derivatives of Eq. 2.14 need to be approximated by a time integration scheme. Here a finite-difference approximation to the temporal derivatives can be used. Also it is necessary to estimate the frequencies, $w_{g_{\ell,m,n}}^P(t)$ and $w_{\ell,m,n}^d(t)$, to determine a complete time-dependent solution.

2.4.2 The Theta Method and the Frequency Transformation Method

In order to obtain the time-difference form of Eq. 2.14, one may consider a sequence of times $t_0, t_1, t_2, \dots, t_n, \dots$, where t_0 is the initial time, and define the time intervals as

$$\Delta t_n = t_{n+1} - t_n.$$

Then, one may approximate the time derivatives¹ for
 $t_{n+1} < t < t_n$ as

$$\frac{\partial}{\partial t} \bar{\phi}_g^{i,j,k}(t) \approx \frac{1}{\Delta t_n} \left(\bar{\phi}_g^{i,j,k}(t_{n+1}) - \bar{\phi}_g^{i,j,k}(t_n) \right) \quad (2.22a)$$

$$\frac{\partial}{\partial t} \bar{C}_d^{i,j,k}(t) \approx \frac{1}{\Delta t_n} \left(\bar{C}_d^{i,j,k}(t_{n+1}) - \bar{C}_d^{i,j,k}(t_n) \right) \quad (2.22b)$$

The time-dependent reaction rates can be approximated by the θ -difference formulation [V-1] as the following for $t_n \leq t \leq t_{n+1}$:

$$\begin{aligned} \bar{J}_{g_{\ell,m,n}}^u(t) &\approx \theta_p \bar{J}_{g_{\ell,m,n}}^u(t_{n+1}) + (1 - \theta_p) \bar{J}_{g_{\ell,m,n}}^u(t_n) \\ \bar{\Sigma}_{\alpha g}^{i,j,k}(t) \bar{\phi}_g^{i,j,k}(t) &\approx \theta_p \bar{\Sigma}_{\alpha g}^{i,j,k}(t_{n+1}) \bar{\phi}_g^{i,j,k}(t_{n+1}) + \\ &\quad (1 - \theta_p) \bar{\Sigma}_{\alpha g}^{i,j,k}(t_n) \bar{\phi}_g^{i,j,k}(t_n). \quad (\alpha = \text{all}) \end{aligned}$$

and

$$\bar{C}_d^{i,j,k}(t) \approx \theta_d \bar{C}_d^{i,j,k}(t_{n+1}) + (1 - \theta_d) \bar{C}_d^{i,j,k}(t_n)$$

where the θ 's, θ_p for the prompt source terms and θ_d for the delayed source terms, are introduced to increase the stability and accuracy of the numerical method.

¹This approximation is not implanted in the QUANDRY code.

In general, these constants can differ at every node for each term in Eq. 2.14, and can change for each time step. QUANDRY does not make use of this complete generality, and instead it takes arbitrary constants between 0.0 and 1.0 for both θ_p and θ_d . For most calculations the value 1.0 is recommended, and 1.0 will be used through the control rod cusping problem calculations to avoid potential oscillations in extrapolation procedure [S-4].

In transient calculations, to advance the solution from one time step to the next requires that all the time-dependent constants (cross-sections, discontinuity factors, etc.) be updated at each time step. In fact, for problems of control rod motions without feedback effect, only the homogenization parameters for a node of interest and the local $w_{g_{\ell,m,n}}^P(t_n)$ and $w_{\ell,m,n}^d(t_n)$ of Eq. 2.15 are required to be updated. The frequencies w_g^P and w^d are identical with those required in the Frequency Transformation Methods [F-6], and can be estimated by the equations

$$w_{g_{i,j,k}}^P(t_n) = \frac{1}{\Delta t_{n-1}} \ln \left[\frac{\phi_{g_{i,j,k}}(t_n)}{\phi_{g_{i,j,k}}(t_{n-1})} \right] \quad (2.23a)$$

and

$$w_{i,j,k}^d(t_n) = \frac{1}{\Delta t_{n-1}} \ln \left[\frac{\bar{c}_{i,j,k}^d(t_n)}{\bar{c}_{i,j,k}^d(t_{n-1})} \right] \quad (2.23b)$$

Since the frequencies change quite slowly except for rapidly changing transient, the frequency updating is usually performed every 3 to 10 time steps in QUANDRY.

2.4.3 The Application of QUANDRY to Light Water Reactor Analyses

The basic unknown in QUANDRY is the volume-averaged nodal flux. For ideal models of light water reactors composed of large nuclearly homogeneous nodes of about 20 cm on a side, QUANDRY predicts the values of the nodal volume fluxes that are usually within 2% of those found from very fine mesh finite-difference solutions even if the discontinuity factors are taken to be unity [S-4]. For real power reactors composed of heterogeneous nodes, making use of AXS and ADF's has yielded maximum errors in nodal or assembly power densities of less than 2-3%, and reactor eigenvalue accurate to within about 0.05% [H-2, K-2, F-5]. Moreover, running time has been shown to be at least two orders of magnitude shorter than that required for a finite-difference solution of the same accuracy.

QUANDRY may be used to analyze three-dimensional problems in which the control rods play an important

role. Previous investigations [K-2] show that when the tip of a control rod resides exactly at the axial nodal interfaces the accuracy of nodal power distributions is comparable to that of a problem without a control rod. However, analyzing a transient problem in which the control rods are moving and thus partially inserted into some nodes has led to serious errors in nodal power distribution. This problem has been more pronounced when feedback is present.

Most methods for reducing the errors caused by moving control rods in QUANDRY rely on generating better homogenization parameters for the partially rodded nodes. Some of them are crude fix-ups while others are somewhat impractical. It is therefore desirable to make an attempt to provide accurate homogenization parameters for partially rodded nodes using methods that are systematic and practical.

2.5 Summary

In this chapter the nodal equivalence theory was first described in both steady-state and time-dependent cases. Approximate methods for estimating the homogenized cross sections and discontinuity factors were then presented. Finally, the nodal code QUANDRY was described with its fundamental equations and approximations for static and transient analyses of light water reactors. Also some QUANDRY test results and the problem associated with

the control rod were mentioned. In the next chapter, the causes, characteristics and solution methods of the problem in QUANDRY associated with control rod operation during reactor transients will be explored.

Chapter 3

THE CONTROL ROD CUSPING PROBLEM

3.1 Introduction

Because the spatial heterogeneity of LWR's in the radial planes is usually more severe than the axial heterogeneity, most homogenization procedures for nodal applications are restricted to radial planes. However, there exists an exception, the axial heterogeneity caused by the presence of control rods. This raises the control rod cusping problem. Several methods have been used in QUANDRY to circumvent the problem, but they have not resulted in satisfactory solutions for a partially rodded node.

In this chapter, the nature and the causes of the control rod cusping problem will be investigated, and several new techniques based on equivalence theory by which the cusping difficulty can be reduced will be suggested and examined.

3.2 Causes of the Cusping Problem

3.2.1 Partially Rodded Node

The axial heterogeneities caused by the presence of control rods create a problem for nodal methods when a rod is partially inserted in a node. A partially rodded

node (PRN) is present whenever the control rod tip locations do not match exactly the axial nodal interfaces. Control rod positions are varied to compensate for fuel depletion and temperature effects as well as to execute changes in the power level and to shut down the reactor. Control rods may be classified as subgroups of regulating, shim, or safety rods, depending on their functions. Regulating rods are used to maintain fine control on reactor power levels and compensate for the effects of changes in temperature and fuel depletion. Shim rods are used to bring the reactor critical and for coarse power level control; they are normally completely out of the core when the reactor is at full power. Also separate safety rods are provided to shut the reactor down. These rods are kept in a cocked position outside the fueled-core while it is critical. Among these rods, only the regulating or shim rods give rise to the control rod cusping problem.

In a typical LWR, regulating or shim rods move notch by notch, the size of the notch being about 1 cm. Hence, with axial node size of 15-30 cm, most three-dimensional nodal configurations will include several partially rodded nodes in either steady-state or transient situations. Thus the partially-rodded, two-zone node shown in Fig. 3.1 is formed when the tip of the control rod fails to reside

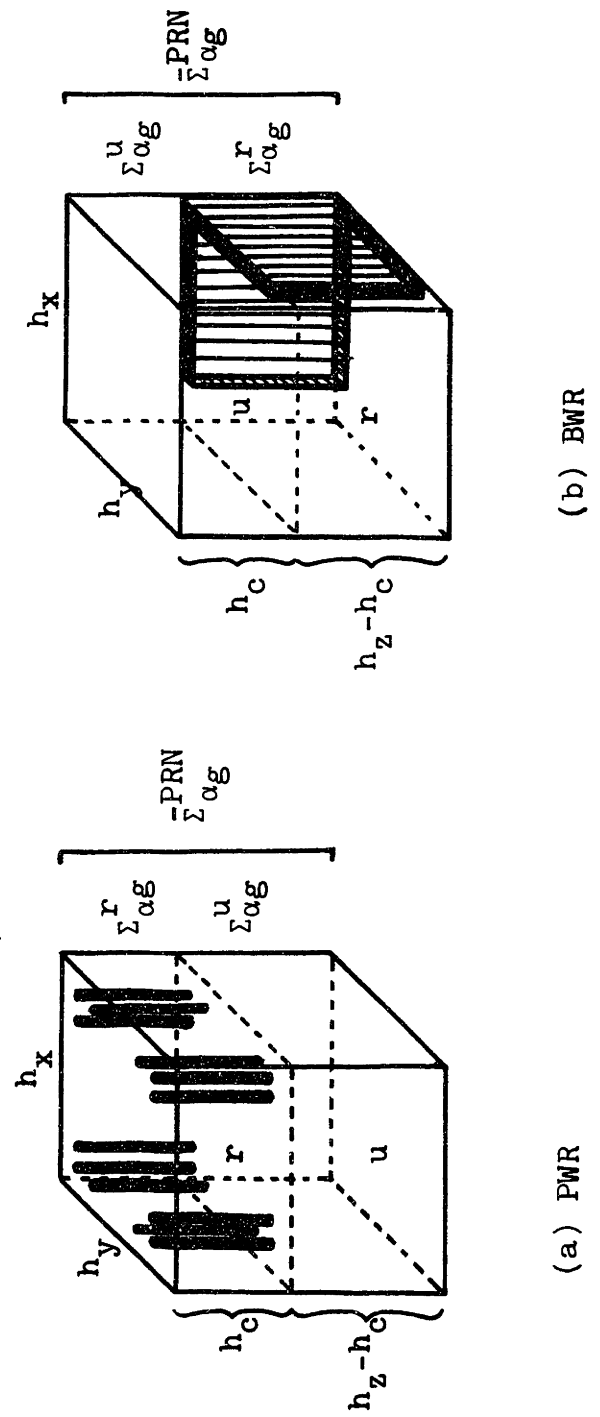


Figure 3.1 Partially rodded nodes.

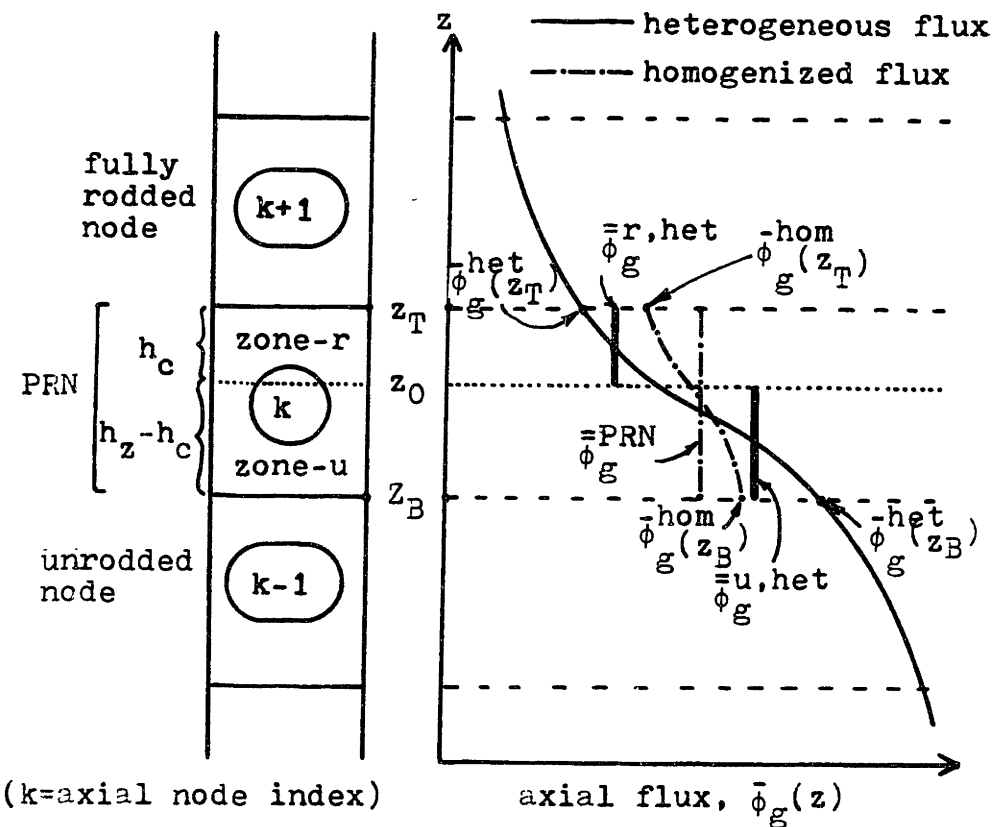
at an axial nodal interface and is inserted to h_c . Homogenized group cross sections (including the discontinuity factors if equivalence theory is applied) are given for the rodded zone ($\Sigma_{\alpha g}^r$ in zone-r) and for the unrodded zone ($\Sigma_{\alpha g}^u$ in zone-u). However, nodal methods need a single set of homogenized cross sections for the entire partially-rodded, two-zone node ($\bar{\Sigma}_{\alpha g}^{PRN}$). The only direct way of avoiding the homogenization of the PRN is to separate the PRN into two smaller nodes, one fully rodded and the other unrodded, and then solve a new nodal problem which has a larger number of axial nodes. This approach raises a problem if, as is often the case, a nodal method requires uniform axial node sizes. If variable axial mesh spacings are allowed but if control rod tips are not aligned, the total number of nodes in a three-dimensional system will increase. And this increase can be substantial for transient cases where a large number of additional, axial nodes of the size of control rod displacement per time step or smaller are needed.

Because of the extra calculational cost of dealing with many axial mesh intervals, the axial homogenization of a partially rodded node provides a highly desirable solution to the control rod cusping problem.

3.2.2 Homogenization Parameters for a Partially Rodded Node

The causes of the control rod cusp are explored in Fig. 3.2. This figure shows a PRN with neighboring fully rodded node (FRN) and an unrodded node (URN); axial group flux shapes within the PRN are shown qualitatively. When the control rods are inserted to $z=z_0$ through the axial nodal interface $z=z_T$, then the node extended from z_B to z_T forms a PRN composed of the roddeed zone ($z_0 \sim z_T$) and the unroddeed zone ($z_B \sim z_0$). The flux $\bar{\phi}_g(z)$ represents a one-dimensional flux shape integrated over radial directions, x and y . $\bar{\phi}_g^{het}(z)$ represents the true axial flux shape obtained by solving the problem in which both the roddeed zone and unroddeed zone of the PRN are treated as two separate nodes, and $\bar{\phi}_g^{hom}(z)$ is its counterpart obtained by treating the PRN as a homogenized node. $\bar{\phi}_g^{hom}$ is the volume-averaged flux of $\bar{\phi}_g^{hom}(z)$ over the PRN, and $\bar{\phi}_g^{r,het}$ and $\bar{\phi}_g^{u,het}$ are the volume-averaged group fluxes of $\bar{\phi}_g^{het}(z)$ over the roddeed and unroddeed zones within the PRN, respectively.

If we are given the exact heterogeneous quantities in both zone-r and zone-u, then the homogenized cross-sections can be determined by preserving the reaction rates as



(a) axial nodes of a rodded assembly

(b) qualitative axial group flux shapes within a PRN extended from $z=z_B$ to $z=z_T$. Control rod tip at $z=z_0$.

Figure 3.2 The cause of the control rod cusping (PWR).

$$\bar{\Sigma}_{\alpha g}^{\text{PRN}} = \frac{h_c \sum_{\alpha g}^{r, \text{het}} + (h_z - h_c) \sum_{\alpha g}^{u, \text{het}}}{h_c \sum_{\alpha g}^{r, \text{het}} + (h_z - h_c) \sum_{\alpha g}^{u, \text{het}}} \quad (3.1a)$$

$$\bar{D}_g^{\text{PRN}} = \left[\frac{h_c \sum_{\alpha g}^{r, \text{het}} / D_g^r + (h_z - h_c) \sum_{\alpha g}^{u, \text{het}} / D_g^u}{h_c \sum_{\alpha g}^{r, \text{het}} + (h_z - h_c) \sum_{\alpha g}^{u, \text{het}}} \right]^{-1} \quad (3.1b)$$

With both homogenized cross sections determined exactly and leakage rates across all the six faces of the PRN known from the exact heterogeneous solution, one may solve the homogenized neutron balance equation for the homogenized group flux $\bar{\phi}_g^{\text{hom}}(z)$ within the PRN. Then the discontinuity factors on the z-directed faces can be found from

$$f_g^{\text{PRN}}(z_B) = \frac{\bar{\phi}_g^{\text{het}}(z_B)}{\bar{\phi}_g^{\text{hom}}(z_B)}$$

$$f_g^{\text{PRN}}(z_T) = \frac{\bar{\phi}_g^{\text{het}}(z_T)}{\bar{\phi}_g^{\text{hom}}(z_T)} \quad (3.2)$$

When the discontinuity factor on the x- or y- directed face of either zone-r or zone-u is not unity, the same procedure can be used to find f_g^{PRN} on the x- and y- directed nodal faces. If there is a way to predict the exact values of $\bar{\phi}_g^{r, \text{het}}$ and $\bar{\phi}_g^{u, \text{het}}$ along with the leakage rates out of the PRN, then the exact equivalence theory parameters

shown in Eqs. 3.1 and 3.2 can be determined. Using these parameters will eliminate the control rod cusping problem. However, the exact solution is generally not available, so that solving the control rod cusping problem requires approximations.

The simplest approximation is to assume that $\bar{\phi}_g^{r,\text{het}} = \bar{\phi}_g^{u,\text{het}}$ and $f_g^{\text{PRN}} = 1$. This is simply the volume-weighted cross section case. Because, in general, $\bar{\phi}_g^{r,\text{het}}$ is smaller than $\bar{\phi}_g^{u,\text{het}}$, the volume-weighted absorption cross sections are overestimated and result in underestimation of the flux level in the PRN, and consequently in the power level. Also using the unity discontinuity factors will cause errors in the reaction rates, not only in the PRN, but also in the neighboring nodes. In fact it is this approximation that has been found to cause the control rod cusping problem. Several alternatives have accordingly been introduced and examined. The next section will describe conventional methods which do not make use of the discontinuity factors.

3.3 Conventional Solution Methods

3.3.1 Tabulation of the Cross Sections of the Partailly Rodded Node

Many nodal methods are created with either cross section data files or separate computer codes for determining

homogenized macroscopic cross sections from microscopic cross sections and nuclide densities. For two-dimensional problems, the homogenized nodal cross sections are usually determined from two-dimensional assembly calculations based on a zero net-current boundary condition. When there exists no severe axial heterogeneity, it is standard to use the homogenized cross sections from the two-dimensional assembly calculations for the three-dimensional global nodal calculation. However, when axial heterogeneities caused by partially inserted control rods or axially varying void fractions are present, one need to find and store the homogenized cross sections for the axially altered node by solving the three-dimensional assembly problem. This approach is, however, impractical especially during a transient when a large number of control rod tip positions must be considered.

3.3.2 Flux Expansions in Polynomials

In order to correct systematically the control rod cusping problem, an alternate model can be used for the PRN. To do so, the axial shapes of the fluxes in the node k (PRN) shown in the Fig. 3.2 are expanded in polynomial functions. This flux expansion method is used in many nodal methods to treat axial or radial heterogeneities. The nodal expansion method (NEM) treats the control rod cusping problem in this manner. In the space-time kinetics

code IQSBOX [B-2, F-7], axial heterogeneity caused by control rods partially inserted into nodes is resolved by fourth-order polynomial expansions where the higher order coefficients are obtained by the weighted-residual scheme. The gain in accuracy is substantial, especially in difficult problems like the LRA-BWR benchmark [W-2]. Smith approximated the shape by the following quadratic polynomials,

$$\bar{\phi}_g^k(z) \approx \bar{\phi}_g^{k-1} \rho_{k-1}(z) + \bar{\phi}_g^k \rho_k(z) + \bar{\phi}_g^{k+1} \rho_{k+1}(z) \quad (3.3)$$

where the expansion functions $\rho(z)$ are identical with those utilized in the quadratic transverse leakage approximation of Eq. 2.21. This expansion possesses the property that the one-dimensional fluxes preserve the average fluxes in each of the three adjacent nodes $k-1$, k and $k+1$. Also, it must be noticed that $\bar{\phi}_g^k(z)$ is valid only in the node k extended from z_B to z_T . The homogenized cross sections of the PRN are then determined from Eq. 3.1 by requiring that

$$\bar{\phi}_g^{r,\text{het}} \approx \frac{1}{(z_T - z_O)} \int_{z_O}^{z_T} \bar{\phi}_g^k(z) dz$$

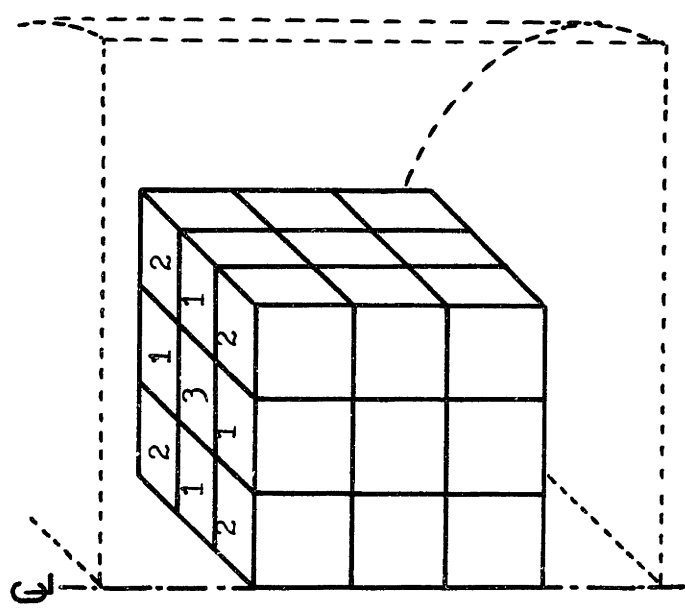
$$\bar{\phi}_g^{u,\text{het}} \approx \frac{1}{(z_O - z_B)} \int_{z_B}^{z_O} \bar{\phi}_g^k(z) dz$$

The homogenized cross sections are then used as the spatially uniform cross sections in the next time step for the transient calculation. Smith's results [S-4] indicate that this approximation reduces the cusping error by approximately 50% for various sizes of the transient time steps. This marginal error reduction shows that even the quadratic expansion of the axial flux shape is not adequate when a node contains partially inserted control rods. To reflect this control rod tip effect in approximating axial flux shape, one can employ higher order approximations such as cubic polynomials, cubic spline interpolations or much higher polynomials [L-2]. Those approximations, however, require additional conditions to determine the expansion functions, do not represent accurate axial flux shapes, and occasionally cause an oscillation problem. The quadratic polynomial expansion method will be examined in Chapter 5 for transient problems.

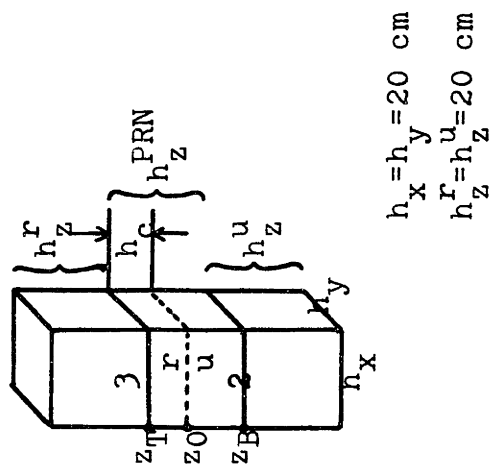
Since the basic cause of the cusp is considered to be an inaccurate homogenization procedure for a partially rodded node, the cusping problem can be cured if both flux-weighted cross sections and the discontinuity factors are determined accurately for a partially rodded node. The next section will introduce several ideas for predicting equivalence theory parameters for a partially rodded node.

3.4 Equivalence Theory Approaches

The use of discontinuity factors to get rid of the control rod cusping problem is examined in this section. Static problems without any thermal hydraulic feedback effect are explored for the simple three-dimensional system shown in Fig. 3.3. The symmetric system is characterized by a simple rodded assembly surrounded by eight homogeneous unrodded assemblies. Zero net-current boundary conditions are imposed on all the external nodal faces. The homogenized cross sections for all nodes except the partially rodded node are assumed to be known, and given in Table 3.1 for compositions of two fuel types and two control rod types. A $3 \times 3 \times 4$ system is created by slicing the partially rodded node in two at $z = z_0$ in Fig. 3.3b; the resultant system thus consists of all homogeneous nodes. The QUANDRY solution for the $3 \times 3 \times 4$ system is then used as a reference. Table 3.2 gives numerical errors in k_{eff} 's and the power densities for the partially rodded node for three different ways of homogenizing the PRN. The tip of the control rod is inserted to the halfway point of the PRN. Taking the volume-weighted constants (VWC) and the unity discontinuity factors (UDF) as the homogenized parameters of the PRN yields the largest error. Using flux-weighted constants (FWC) and unity discontinuity factors (UDF)



(a) a $3 \times 3 \times 3$ node system as a part
of a $1/4$ core



(b) central rodded assembly

Figure 3.3 A $3 \times 3 \times 3$ node model with rodded central assembly surrounded by eight unrodded assemblies in symmetric layout. A zero net current boundary condition is imposed upon all the six external faces. The numbers on the nodes represent node composition types shown in Table 3.1.

Table 3.1 Homogenized Nodal Cross Sections for 3 X 3 X 3 Node Models.

node composi- tion type	node composi- tion	group g	D _g (cm)	Σt_r^g (cm ⁻¹)	Σr_g^g (cm ⁻¹)	$\nu \Sigma f_g^g$ (cm ⁻¹)	Σf_g^g (cm ⁻¹)	
1	fuel 1 + water	1	1.513	0.03323	0.02113	0.006012	0.002405	
		2	0.3950	0.1684	0.0	0.2186	0.08745	
2	fuel 2 + water	1	1.513	0.03045	0.02113	0.004625	0.001850	
		2	0.3951	0.1414	0.0	0.1645	0.0658	
3	fuel 2 control rod 1	1	1.463	0.03422	0.02129	0.004633	0.001853	
		2	0.3772	0.1921	0.0	0.1707	0.06829	
4	fuel 1 control rod 1	1	1.463	0.0370	0.02129	0.006022	0.002409	
		2	0.3763	0.2223	0.0	0.2271	0.09084	
$\Sigma t_1 = \Sigma a_1 + \Sigma 21$				$\Sigma r_1 = \Sigma 21$		$\Sigma r_2 = \Sigma 12$		
$\Sigma t_2 = \Sigma a_2$								

**Table 3.2 Comparison of $3 \times 3 \times 3$ Symmetric System Calculations
($h_c = 10$ cm case and percent error in the parenthesis).**

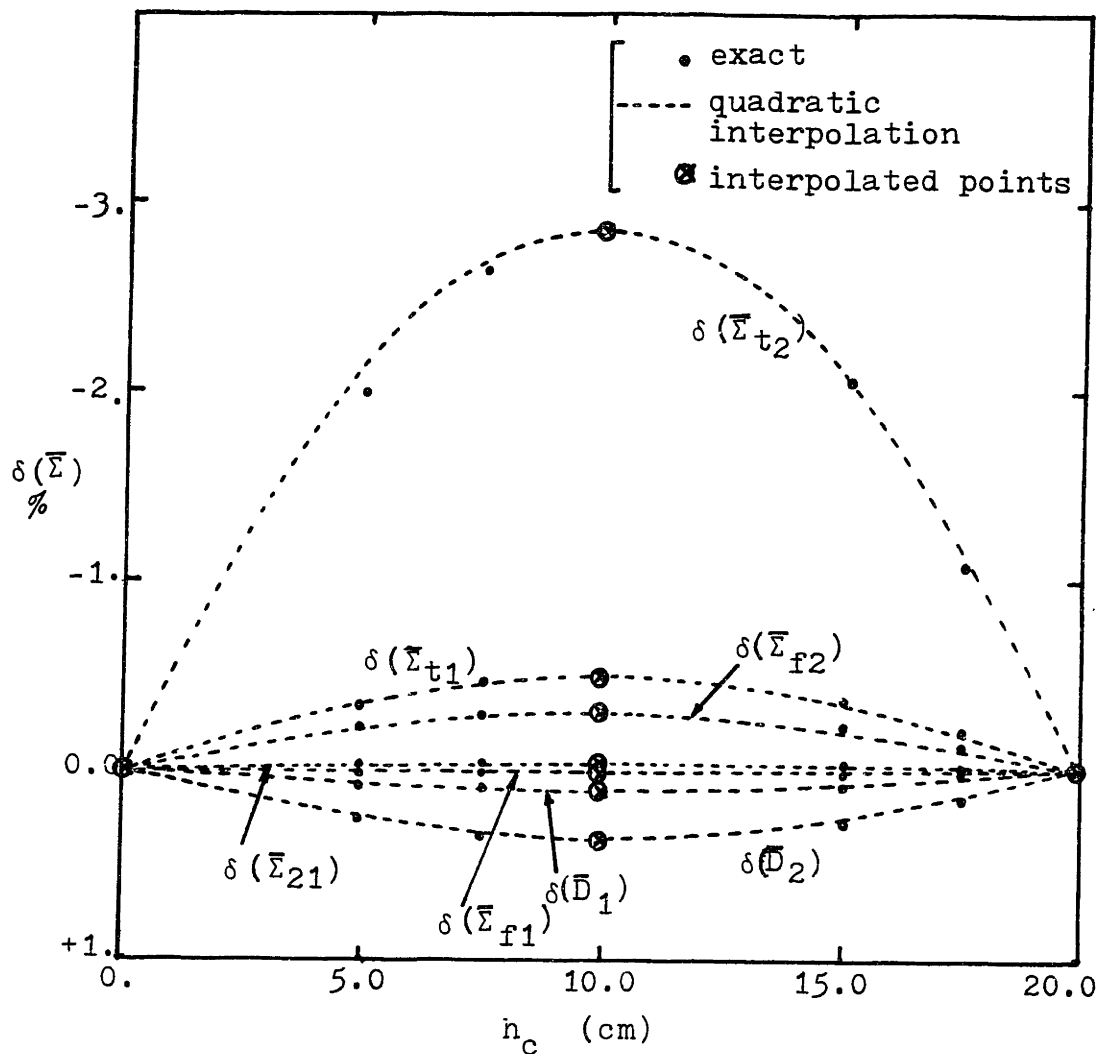
methods	κ_{eff}	rodded assembly power	PRN power	power of fully rodded top node	power of completely unrodded bottom node
reference $3 \times 3 \times 4$ calc.	0.969535	0.78417	0.77246	0.56384	1.01620
VWC + UDF	0.968602 (-0.10%)	0.77290 (-1.4%)	0.75009 (-2.9%)	0.58097 (3.0%)	0.98766 (-2.8%)
FWC + UDF	0.969286 (-0.026%)	0.78110 (-0.39%)	0.77116 (-0.17%)	0.58253 (3.3%)	0.98961 (-2.6%)
FWC + RDF	0.969535 (0%)	0.78417 (0%)	0.77246 (0%)	0.56384 (0%)	1.01620 (0%)

also results in significant errors in k_{eff} and the nodal power levels, especially in the neighboring top and bottom nodes.

When the discontinuity factors for the rodded node (i.e. the reference discontinuity factors, RDF) generated from the standard 3 X 3 X 4 QUANDRY calculation are used along with the FWC, QUANDRY, as expected, reproduces the 3 X 3 X 4 result. This test result shows that if the exact equivalence theory parameters, FWC and RDF, could be found for PRN, the control rod cusping problem could be eliminated. In the following sections, several approaches are attempted to determine these equivalence theory parameters.

3.4.1 Tabulation and Interpolation of the Homogenization Parameters

The same approach explained in Section 3.3.1 can be applied for estimation of the RDF and FWC for the PRN. Many test problems show that these equivalence theory parameters do not change uniformly as the position of the control rod tip, h_c , varies in the PRN. Hence, it is useful to compare the FWC and the VWC, because the VWC change uniformly and match the FWC exactly at the end points, z_B and z_T in Fig. 3.3b. The relative differences, $\delta(\bar{\Sigma})$, of various types of cross sections for several values of h_c are displayed in Fig. 3.4.



$$\delta(\bar{\Sigma}) \equiv 100 \frac{\bar{\Sigma}^{\text{FWC}} - \bar{\Sigma}^{\text{VWC}}}{\bar{\Sigma}^{\text{VWC}}} (\%)$$

Figure 3.4 Relative difference of $\bar{\Sigma}^{\text{FWC}}$ and $\bar{\Sigma}^{\text{VWC}}$ vs. control rod tip position (h_c), and quadratically interpolated approximations. Interpolations at $h_c = 0, 10$ and 20 cm. PRN of a central node of $3 \times 3 \times 3$ node system.

The result suggests the possibility that $\delta(\bar{\Sigma})$ can be approximated by quadratic polynomials (shown in dotted curves in Fig. 3.4) determined by computing one set of FWC's at $h_c = 1/2 h_z$. The figure shows that, except for $\bar{\Sigma}_{t2}$, the errors in the two group parameters as found by the quadratic fit are negligible.

Restarting QUANDRY with data from $3 \times 3 \times 4$ solutions of the system in Fig. 3.3a produces the exact axial discontinuity factors for the PRN of the $3 \times 3 \times 3$ system. These exact group discontinuity factors (radial and axial) of the PRN as a function of h_c are given in Table 3.3 and Fig. 3.5. The reason for the slight variations of f_{xg}^{\pm} from unity is that the equivalence equations are solved using the QUANDRY nodal approximation (i.e., quadratic transverse leakage). If the equivalence equations were solved in an exact manner, the values of the radial discontinuity factors would be unity for this problem. The curves of the thermal group discontinuity factors are skewed more than the fast group ones, and the fast group discontinuity factors show less variation than do the thermal group discontinuity factors. It has also been found that the general "shapes" of the f_g^{\pm} - curves are not altered much when the axial node size or cross sections are changed.

Table 3.3 Discontinuity Factors of the PRN in Figure 3.3 as a Function of Control Rod Tip Position, h_c .

disconti-nuity factor * f_{zg}^{\pm}	$h_c = 5\text{cm}$	$h_c = 7.5\text{cm}$	$h_c = 10\text{cm}$	$h_c = 15\text{cm}$	$h_c = 17.5\text{cm}$
f_{z1}^-	1.0456	1.0698	1.0850	1.0732	1.0381
f_{z2}^-	1.0961	1.1545	1.2077	1.2677	1.2211
f_{z1}^+	0.9172	0.9024	0.9051	0.9476	0.9812
f_{z2}^+	0.7528	0.7595	0.7867	0.8855	0.9530
f_{x1}^-	0.9999	0.9998	0.9998	0.9998	0.9999
f_{x2}^-	0.9974	0.9964	0.9959	0.9968	0.9983
f_{x1}^+	0.9999	0.9998	0.9998	0.9998	0.9999
f_{x2}^+	0.9974	0.9964	0.9959	0.9968	0.9983

* $f_{zg}^- \equiv f_{zg}^-(Z_B)$ and $f_{zg}^+ \equiv f_{zg}^+(Z_T)$
 $f_{xg}^- = f_{yg}^+$ for the symmetric $3 \times 3 \times 3$ node system.

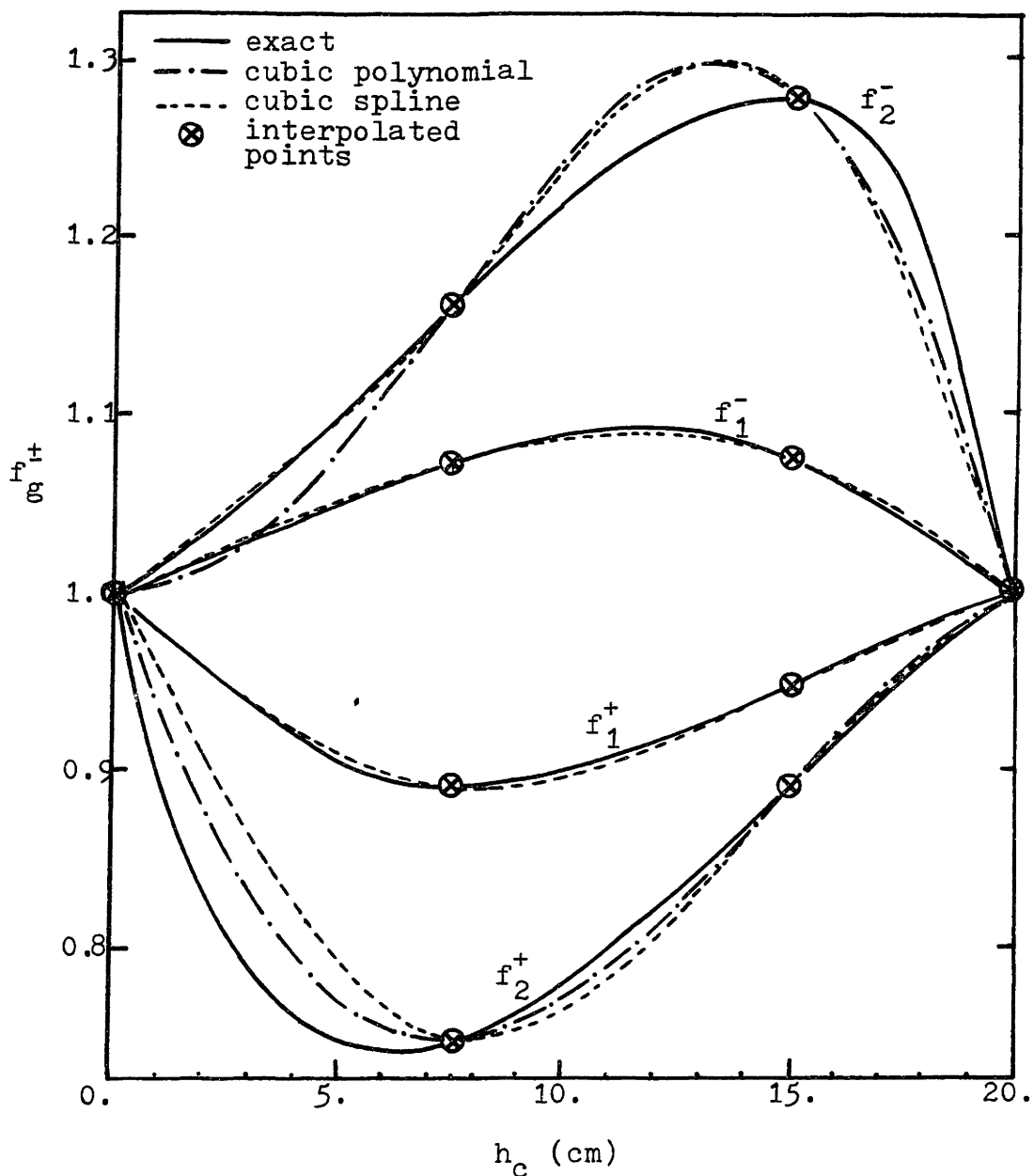


Figure 3.5 Interpolations of axial discontinuity factors at $h_c = 7.5$ and 15 cm for the PRN of a $3 \times 3 \times 3$ node system. Numerical values are tabulated in Appendix 1.2.

The axial node size dependence of the axial discontinuity factors is illustrated in Fig. 3.6. As the axial node size increases, the discontinuity factors of both groups become more significant, and it is noticeable that also the fast group discontinuity factors turn out to be as significant as the thermal group discontinuity factors when the axial node size is 40 cm as shown in Fig. 3.6c. In Fig. 3.6b, one sees that the fast group discontinuity factors are very close to unity with relatively small h_z^{PRN} . These facts suggest that the axial discontinuity factors play a very important role in the control rod cusping problem for both thermal and fast group nodal calculations when the axial nodal size is comparable to the distance between the grid spacers of an LWR assembly (20 ~ 40 cm in usual cases). Even though the general shapes of the f_g^\pm -curves are not very sensitive to the axial nodal size, the skewed f_g^\pm -curves are not amenable to quadratic polynomial interpolation. Instead, cubic polynomials and the region-wise cubic spline interpolations with two intermediate sets of data points (at $h_c = 7.5$ cm and 15 cm) have been used to fit them. The equations for interpolations are derived in Appendix 1.2, and the comparison is made in Fig. 3.5. Both approximations are relatively poor, especially in the thermal group, when the control rods are close to either nodal boundary. Also, greater errors can result if intervals between

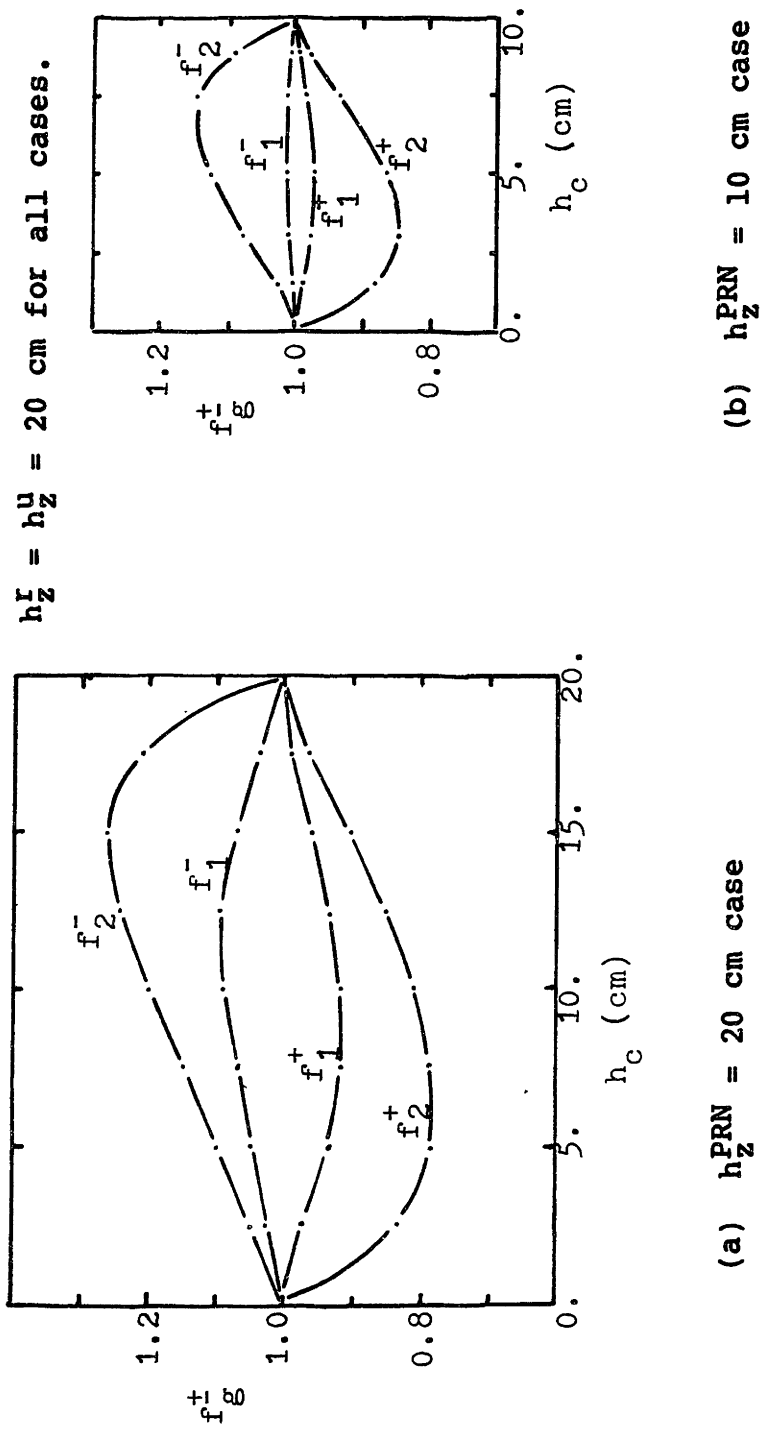


Figure 3.6 Axial discontinuity factors vs. control rod tip position, h_c^{Ω} , for three different axial node widths of the PRN of the $3 \times 3 \times 3$ node system shown in Fig. 3.3a.

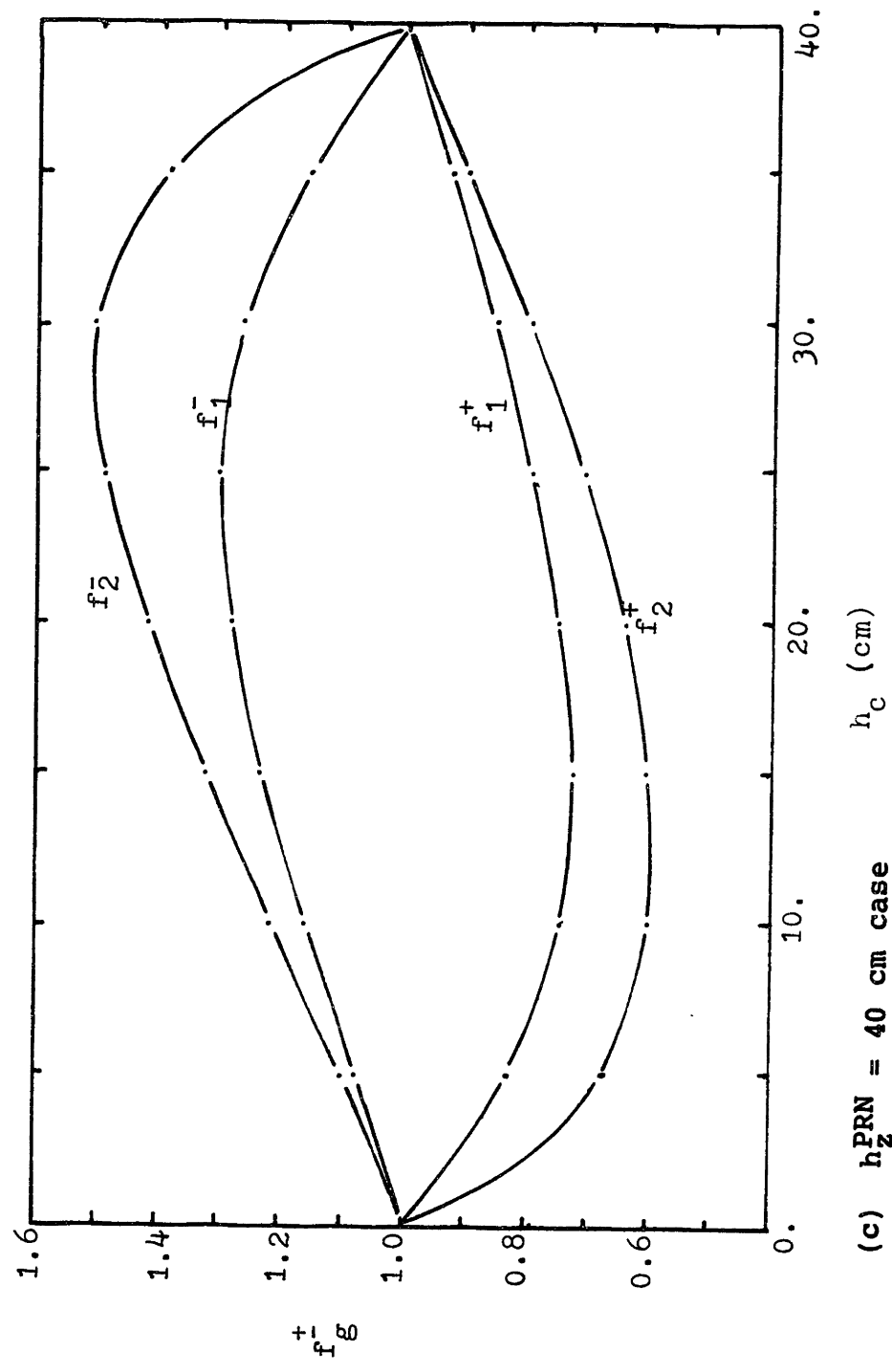


Figure 3.6 (continued)

data points are not properly chosen [J-1].

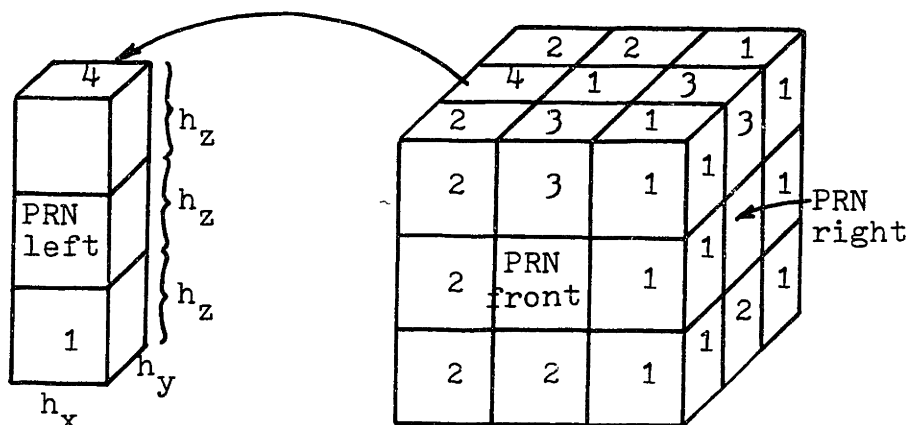
In order to examine whether axial discontinuity factors for a PRN for one condition can be used for a different condition, the exact f_g^{\pm} values for the PRN in the symmetric system (Fig. 3.3a), along with their FWC's, were used for the asymmetric system shown in Fig. 3.7. Results are given in Table 3.4 for three different control rod axial positions. They show that the equivalence theory parameters for the symmetric system are moderately accurate when used for an asymmetric system. The k_{eff} and nodal power density are calculated to within 0.03% and 0.8%, respectively. The largest error is found for the control rod tip position, h_c , near to the node midpoint. The adequacy of transferring FWC's and discontinuity factors for a specific PRN found under one set of conditions to that same PRN under another set of conditions is an important consideration, and will be recalled in the next chapter when a new method is introduced.

3.4.2 Volume-Weighted Cross Sections and Axial Discontinuity Factors

The volume-weighted cross sections (VWC's) provide the simplest choice for the homogenized cross sections of a PRN, since computing them does not require knowing the detailed flux shape within the PRN. When the VWC's are used, and if discontinuity factors (DF) which preserve

Table 3.4 Results of 3 X 3 X 3 Asymmetric Calculations with FWC's and Discontinuity Factors of the Symmetric System. Reference is a 3 X 3 X 4 Asymmetric Calculation.

error in	$h_c = 3\text{cm}$	$h_c = 10\text{cm}$	$h_c = 14\text{cm}$	
k_{eff}	-0.028%	-0.031%	-0.027%	
power density	{ front PRN right PRN left PRN	-0.41% -0.23% -0.25%	-0.74% -0.44% -0.53%	-0.61% -0.33% -0.42%
max. nodal power	1.6%	2.2%	2.1%	



$$h_x = h_y = h_z = 20 \text{ cm}$$

$$\mathbf{n} \cdot \mathbf{J}_g = 0 \text{ on all the surfaces}$$

Figure 3.7 An asymmetric 3 X 3 X 3 system with three rodded assemblies. The numbers represent node composition types given in Table 3.1.

the reactor eigenvalue, reactions rates and leakage rate of a PRN are available, one may eliminate the control rod cusping problem. A methodology of making use of VWC and DF is explained in Appendix 1.3.

It has been found that while VWC's and their corresponding exact discontinuity factors reproduce the correct nodal leakages and the exact k_{eff} , the "individual" reaction rates (and hence, power level) in the PRN are not preserved. Along with this drawback, the wide spread in the discontinuity factors (which have a value ~5.0 in the test problem in Appendix 1.3) provide a potential source of error when they must be computed approximately. Consequently, used in conjunction with the discontinuity factors, flux-weighted cross sections are expected to be more reliable than volume-weighted cross sections.

3.4.3 An Asymptotic Method

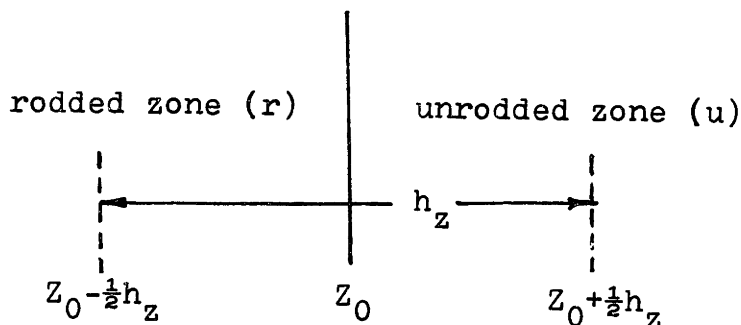
Since the tabulation and interpolation schemes that require a few additional reference solutions to provide the equivalence theory parameters of a PRN have been found to be impractical, it is desirable to consider analytic and system-independent methods which can provide the parameters from information about the material composition and dimensions of the regions around the tip of the control rods. The simplest approach is to consider an infinite system composed of two semi-infinite slabs of different

neutronic composition, one-half is the rodded region and the other half unrodded as shown in the diagram below. The length h_z is the axial node size of a PRN.

The basic idea is to solve a one-dimensional, two-group, two-region diffusion equation for group flux shapes around the interface of the two-region system by applying the asymptotic group flux ratios and by introducing some conditions available from the actual three-dimensional PRN of interest. To obtain two-group fluxes over the two regions, one may start with the two-group, two-region flux solutions given in the following form [H-1]:

$$\begin{bmatrix} \phi_1^k(z) \\ \phi_2^k(z) \end{bmatrix} = \begin{bmatrix} c_1^k & c_2^k & c_3^k & c_4^k \\ r^k c_1^k & r^k c_2^k & s^k c_3^k & s^k c_4^k \end{bmatrix} \begin{bmatrix} \sin K_k z_n \\ \cos K_k z_n \\ \sinh U_k z_n \\ \cosh U_k z_n \end{bmatrix} \quad (3.4)$$

where



$k = \text{region } r \text{ or } u$

$z_n \equiv z_0 - z \text{ for } k = r$

$\equiv z - z_0 \text{ for } k = u$

$$K^2 \equiv \frac{1}{2} \left[\frac{\Sigma_1}{D_1} + \frac{\Sigma_2}{D_2} \right] + \left[\left(\frac{\Sigma_2}{2D_2} - \frac{\Sigma_1}{2D_1} \right)^2 + \frac{\nu \Sigma f_2 \Sigma_{21}}{k_{\text{eff}} D_1 D_2} \right]^{1/2}$$

$$U^2 \equiv \frac{1}{2} \left[\frac{\Sigma_1}{D_1} + \frac{\Sigma_2}{D_2} \right] + \left[\left(\frac{\Sigma_2}{2D_2} - \frac{\Sigma_1}{2D_1} \right)^2 + \frac{\nu \Sigma f_2 \Sigma_{21}}{k_{\text{eff}} D_1 D_2} \right]^{1/2}$$

$$\Sigma_1 \equiv \Sigma_{t_1} - \frac{1}{k_{\text{eff}}} \nu \Sigma f_1$$

$$\Sigma_2 \equiv \Sigma_{t_2}$$

$$r \equiv \frac{\Sigma_{21}}{D_2 K^2 + \Sigma_2}$$

$$s \equiv \frac{\Sigma_{21}}{-D_2 U^2 + \Sigma_2}$$

for region r or u .

To solve for the eight unknown coefficients C_j^k in Eq. 3.4, one needs eight conditions. When the flux and current continuity conditions are applied for each energy group, one still needs four additional conditions. To obtain additional equations, we consider a small region between $z = z_0 - \frac{h_z}{2}$ and $z = z_0 + \frac{h_z}{2}$. If the size of h_z is longer than the usual neutron migration length ($\approx \sqrt{D_1 / \Sigma_{t_1}}$) of the homogenized nodes in typical LWR's, then the thermal-to-fast group flux ratios at $z = z_0 \pm \frac{h_z}{2}$ can be approximated by their asymptotic group flux ratios. The typical migration length with the homo-

genized nodes is in most cases not longer than about 10 cm, and if h_z is taken to be 20 cm, then one may approximate

$$\frac{\bar{\phi}_2^r (z_0 - \frac{h_z}{2})}{\bar{\phi}_1^r (z_0 - \frac{h_z}{2})} \approx r^r \quad (3.5a)$$

and

$$\frac{\bar{\phi}_2^u (z_0 + \frac{h_z}{2})}{\bar{\phi}_1^u (z_0 + \frac{h_z}{2})} \approx r^u \quad (3.5b)$$

Substituting these asymptotic relationships at $z = z_0 \pm \frac{1}{2}h_z$ to Eq. 3.4 yields

$$C_4^r \approx -C_3^r \tanh \left(U_r \frac{h_z}{2} \right)$$

$$C_4^u \approx -C_3^u \tanh \left(U_u \frac{h_z}{2} \right) .$$

In many LWR's, the typical magnitudes of U_r and U_u lie in the range $0.4 \sim 0.7$ [H-1]. Hence, from the fact that $\tanh 4 = 0.99933\dots$, one can get a relationship

$$C_4^k \approx -C_3^k$$

for both $k = r$ and $k = u$. Consequently, the number of

unknown coefficients is reduced to six. Applying the interface continuity conditions results in four nonhomogeneous equations for five unknowns, C_j^k , in terms of one remaining C_3^k as follows.

$$\begin{bmatrix} D_1^r & 0 & D_1^u & 0 & D_1^u & U_u \\ 0 & 1 & 0 & -1 & 1 & \\ D_2^r r^r & 0 & D_2^u r^u & 0 & D_2^u s^u U_u & \\ 0 & r^r & 0 & -r^u & s^u & \end{bmatrix} \begin{bmatrix} K_r C_1^r \\ C_2^r \\ K_u C_1^u \\ C_2^u \\ C_3^u \end{bmatrix} = \begin{bmatrix} -D_1^r U_r C_3^r \\ C_3^r \\ -D_2^r s^r U_r C_3^r \\ s^r C_3^r \end{bmatrix} \quad (3.6)$$

The coefficients C_1^r and C_1^u are written with K_r and K_u , respectively, to avoid imaginary variables in the elements of the matrix or column vectors.

We still need one more equation to solve for the two-group flux shape in terms of C_3^k . After several possible properties of a PRN were explored by solving the $3 \times 3 \times 3$ symmetric system (Fig. 3.3a) for various sizes of h_c , four conditions were found, which depend only weakly on the control rod tip position. Those are $\bar{\phi}_g(z_o)/\bar{J}_g(z_o)$ and $\bar{\phi}_g^r/\bar{\phi}_g^u$ within the PRN (for $g = 1, 2$) and their numerical values are shown in Fig. 3.8. It can be seen that these variables are very uniform for all h_c values. And this suggests that if one of them is known for a particular value of h_c , then it can provide the fifth condition determining the C_j^k . Solving Eq. 3.6

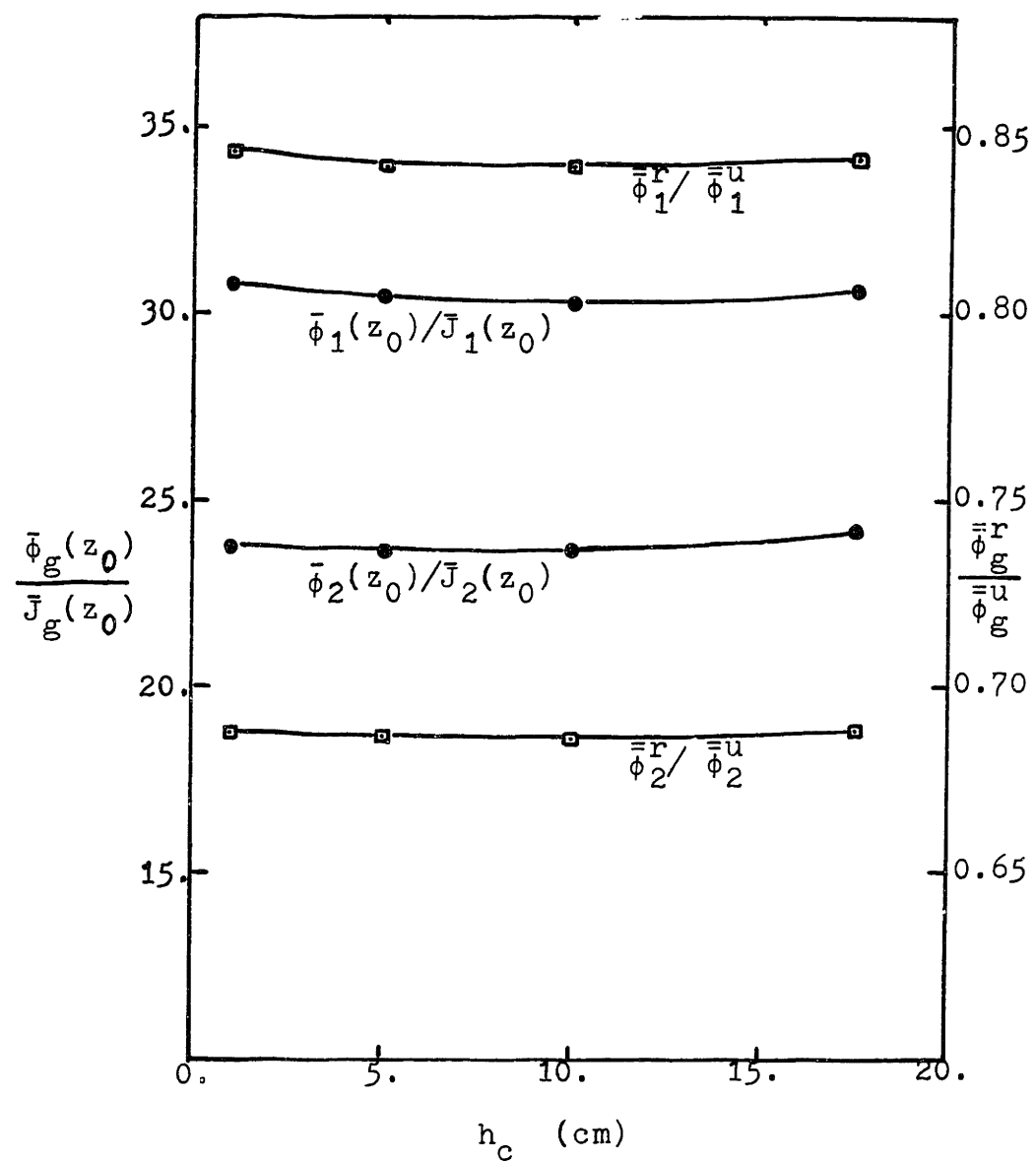


Figure 3.8 Nodal variables of the PRN in a 3 X 3 X 3 symmetric system as a function of control rod tip position, h_c .

and this fifth equation for the C_j^k determines the heterogeneous group flux shapes in the regions r and u near the interface. In carrying out this procedure, k_{eff} , is assumed to be unity.

The flux shape is then edited out for a new PRN of interest, and the corresponding flux-weighted cross sections are found. Using these flux-weighted cross sections and the boundary surface currents of the PRN determines the homogenized surface fluxes of the PRN, which ultimately yield the axial discontinuity factors. For testing this asymptotic method, the $\bar{\phi}_2^r/\bar{\phi}_2^u$ value at $h_c = 10$ cm was chosen from the $3 \times 3 \times 3$ symmetric model (Fig. 3.3a) calculation, and examined for two h_c values, 10 cm and 17.5 cm. Table 3.5 shows the result. The k_{eff} and nodal power densities for $h_c = 10$ cm have been predicted with negligible errors. However, for the case of $h_c = 17.5$ cm, the errors increase significantly. This fact reflects the fact that for $h_c = 17.5$ cm the width of the unrodded region is only 2.5 cm which is far less than the neutron migration length in the region, and the asymptotic flux shapes near the interface of the two different materials do not represent well the exact flux shapes. Use of the three other quantities shown on Fig. 3.8 to provide the fifth equation has shown similar results, with $\bar{\phi}_g(z_o)/\bar{J}_g(z_o)$ yielding the worst

Table 3.5 Asymptotic Method Results of 3 X 3 X 3 Symmetric System Calculations.

- exact $\frac{\bar{\phi}_2^r}{\bar{\phi}_2^u} = 0.682$ for $h_c = 10 \text{ cm}$
 $= 0.686$ for $h_c = 17.5 \text{ cm}$
- trial $\frac{\bar{\phi}_2^r}{\bar{\phi}_2^u} = 0.682$ for both $h_c = 10 \text{ cm}$
 $\text{and } h_c = 17.5 \text{ cm.}$

comparison		$h_c = 10 \text{ cm}$	$h_c = 17.5 \text{ cm}$
k_{eff}	exact	0.969535	0.966035
	asymptotic method	0.969522	0.965893
	error	-0.0012%	-0.015%
nodal power of FRN*	exact	0.56384	0.56884
	asymptotic method	0.56377	0.56881
	error	-0.012%	-0.005%
nodal power of PRN	exact	0.77246	0.67215
	asymptotic method	0.76904	0.66453
	error	-0.44%	-1.1%
nodal power of URN**	exact	1.0162	0.99619
	asymptotic method	1.0190	0.99918
	error	0.28%	0.30%

* FRN = fully rodded node on the top of the PRN.

** URN = fully unrodded node below the PRN.

result.

Also the $3 \times 3 \times 3$ asymmetric problem (Fig. 3.7) tested with this method showed that it is inadequate for real reactor analysis even if it has shown moderate errors for the very simple $3 \times 3 \times 3$ symmetric system. The main flaw of the one-dimensional asymptotic method is that the transverse leakages between radially adjacent nodes and the partially rodded node have not been considered.

The rodded fuel assemblies in a core are usually surrounded by unrodded fuel assemblies, and there exists strong neutron currents across the interfaces between the rodded subnode within a PRN and radially adjacent unrodded nodes or an axially adjacent unrodded subnode. Thus, the transverse leakages (in radial directions) must be taken into consideration in the course of predicting the axial group flux shapes within a PRN which is usually surrounded by five unrodded nodes. This idea will be systematically explained and examined in the following chapters.

3.5 Summary

There is considerable motivation for locating axial nodal interfaces at fixed planes and dealing with the intra-node axial discontinuities associated with partially inserted control rods by using some combination of non-unity

axial discontinuity factors and axially flux-weighted homogenized cross sections. In this chapter, the possibility of making use of tabulation-interpolation methods was examined, and the volume-weighted cross section approach with corresponding discontinuity factors was investigated. However, the results of the investigations showed that these methods are problem-dependent, requiring complete global calculation, and demand considerable machine memory space -- all unattractive features.

For estimation of approximate homogenized cross sections and axial discontinuity factors for a partially rodded node, an asymptotic axial flux construction method was introduced. This method was also found to be problem-dependent and inconsistent with actual core configurations. The axial flux construction method, however, does lead to an idea for the reconstruction of axial group flux shapes by taking the transverse leakage into account. The next chapter will explain this idea.

Chapter 4

THE COLLECTOR-PREDICTOR METHOD

4.1 Introduction

It has been demonstrated that use of exact homogenized flux-weighted cross sections (FWC) and corresponding discontinuity factors (DF) eliminates the control rod cusping problem. However, these equivalence theory parameters can be determined exactly only if an exact global solution is known. Because such an exact solution is not known, several approximate approaches were introduced and examined in the previous chapter. None of them were entirely satisfactory, and a simple systematic, problem-independent way to solve the cusping problem using data internal to a nodal method computer program is still desired.

Another scheme based on the asymptotic flux construction method will be explained in this chapter. The basic idea is to estimate (in a step called "Predictor") the axial flux shape within a partially rodded node (PRN) using information already available from the same system and collected in another step called "Collector". If the collecting and predicting is done correctly, the FWC and DF of the PRN will yield the exact reactor solution for both static and transient situations.

4.2 Description of Two Methods

Based on the asymptotic flux construction method, two axial flux reconstruction methods have been investigated even though the basic concepts are very similar. The first one is relatively simple but, for some situations, somewhat inaccurate. It may be useful in a steady-state case. The second one is more complicated, but is capable of performing more accurate predictions, and is adequate for transient calculations. For brevity the first is called "Method 1", and the second "Method 2". Radially homogenized cross sections and radial discontinuity factors for both the fully rodded node (FRN) and the completely unrodded node (URN) are assumed to have been found already, and will be considered as available for axial flux reconstruction purposes.

4.2.1 Method 1

This method is an extension of the asymptotic flux construction method described in the previous chapter, and makes use of the nodal flux shape information implicit in the QUANDRY solution for the case of the control rod tip positioned exactly at an axial nodal interface.

The one-dimensional axial flux shapes within two axially-adjacent nodes, one fully rodded (region-r) and the other completely unrodded (region-u) (see Fig. 4.1), are found using boundary currents on the axial faces

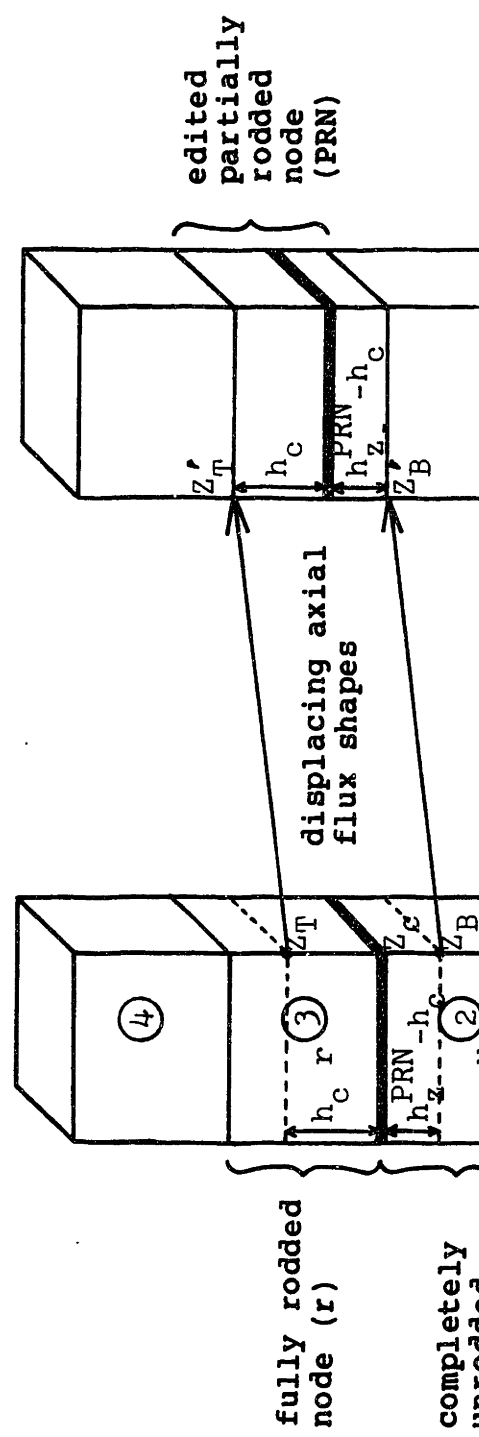


Figure 4.1 Method 1 of the Collector-Predictor scheme.

and transverse leakages known from the global QUANDRY solution. Transverse leakage terms can be approximated as quadratic in shape for QUANDRY application. Then the axial flux shapes for the two nodes are displaced (Fig. 4.1b) to predict an approximate flux shape within the partially rodded node. With this edited flux shape within the PRN, one can calculate the FWC of the PRN from the known homogeneous cross sections in r and u . This FWC and the surface currents at the axial faces at z'_B and z'_T of the edited PRN can be used to calculate the homogenized surface group fluxes at z'_B and z'_T . Thus the discontinuity factors for the PRN of interest can be found.

The extent of the control rod insertion is specified by h_C , and the appropriate flux shapes for various values of h_C in Fig. 4.1b can be approximated by editing the axial flux shapes reconstructed over the two nodes of Fig. 4.1a. The basic assumption of this method is that the axial flux shapes around the control rod tip do not vary significantly when the control rod travels the distance of one axial node.

4.2.2 Method 2

To improve Method 1, we can make use of the flux shapes reconstructed for a previously, partially rodded condition to predict the flux shapes within a PRN where

now the position of the control rod tip is changed slightly from the previous position. Thus we solve analytically a one-dimensional, three-region problem for axial flux shapes throughout the regions u , w and r of Fig. 4.2a. Then we edit out the axial flux shapes appropriate to the altered control rod tip position (h'_c in Fig. 4.2b) between z_B and z_T in Fig. 4.2a, and assume these flux shapes are valid in the new PRN composed of two regions r' and w' . For a displacement, $h_c - h'_c$, shorter than the axial node size, h_z , this second method will predict more accurate homogenization parameters than Method 1, and will be particularly useful for transient rod withdrawal problems. Another advantage of Method 2 over Method 1 is that it can be used in transient problems initiated with partially rodded nodes (provided the homogenization parameters at the starting point are given). Method 1 on the other hand, always requires that the starting problem have no partially rodded nodes anywhere. For a rod insertion problem, the same principle can be applied, however, the edit boundary (the points z_T and z_B) will move up rather than down.

In solving the three-region problem for the axial flux shapes in regions u , w and r , we require the average radial transverse leakage rates for each of those three regions. Unfortunately, the nodal method solution gives

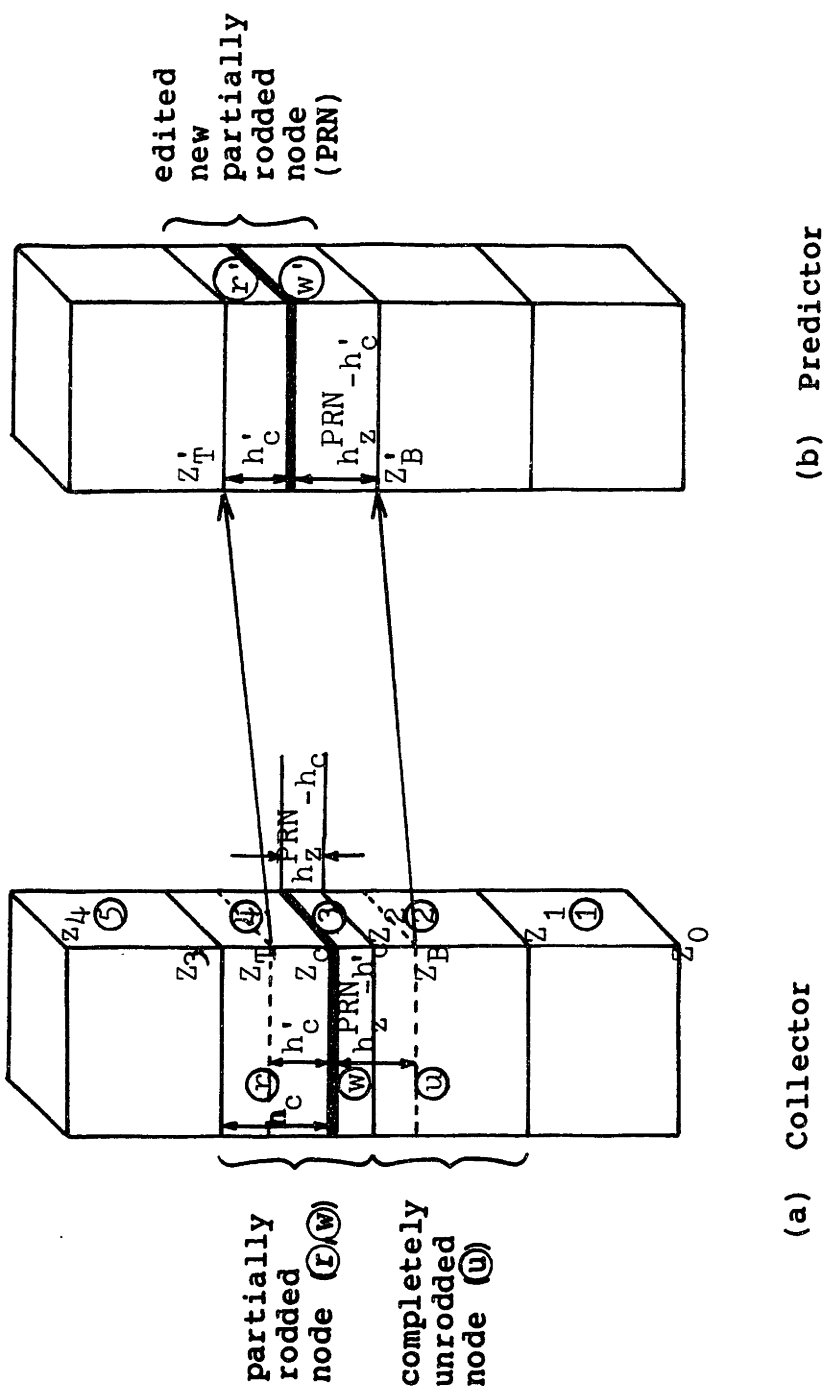


Figure 4.2 Method 2 of the Collector-Predictor scheme.

only the node-averaged transverse leakages of node u and of the PRN, and the individual transverse leakages of subnodes r and w are unknown. Several approaches for finding these transverse leakages will be described later; for the present these rates are assumed to be known.

Because Method 1 is a special case of Method 2 (i.e., when $z_c = z_2$ in Fig. 4.2a), only the flux reconstruction steps and predicting procedures associated with Method 2 will be analyzed in detail in the following sections.

4.3 De-Homogenization and Prediction

Predicting the axial flux shape within a PRN at the Predictor-stage requires axial flux reconstruction within a PRN at the Collector stage and its axially adjacent nodes (see Fig. 4.2). The flux iterations performed at each inner iteration of a time step (n) in a transient problem are identical with those of the steady-state problem. Hence, the steady-state equation (Eq. 2.9) can be solved for the axial flux shape at time step (n) making use of the global nodal solution at that time step. Rewriting Eq. 2.9 in two-group form gives

$$\begin{bmatrix} D_1^k \frac{d^2}{dz^2} - \Sigma_1^k & \frac{1}{k_{\text{eff}}} v \Sigma f_2 \\ \Sigma_{21}^k & D_2^k \frac{d^2}{dz^2} - \Sigma_2^k \end{bmatrix} \begin{bmatrix} \bar{\phi}_1^k(z) \\ \bar{\phi}_2^k(z) \end{bmatrix} = \begin{bmatrix} S_1^k(z) \\ S_2^k(z) \end{bmatrix} \quad (4.1)$$

where the superscript k represents one of the three regions of the Collector stage, u, w and r. The Σ_g^k has been defined by Eq. 3.4, and all the cross sections are homogenized ones. Approximation of the transverse leakage terms, $S_g^k(z)$, in QUANDRY-type quadratic polynomials yields

$$S_g^k(z) \approx \sum_{j=0}^2 Q_{g_j}^k z^j \quad (4.2)$$

The group expansion functions $Q_{g_j}^k$ are defined in Appendix 2.1.

4.3.1 De-Homogenization Yielding the Axial Flux Shapes

A general solution $\bar{\phi}_g^k(z)$ of the linear nonhomogeneous differential equation (4.1) is the sum of a general solution $H_g^k(z)$ of the corresponding homogeneous equation and an arbitrary particular solution $P_g^k(z)$ of Eq. 4.1. $H_g^k(z)$ has the same form as Eq. 3.4:

$$\begin{bmatrix} H_1^k(z) \\ H_2^k(z) \end{bmatrix} = \begin{bmatrix} 1 & 1 \\ r^k & s^k \end{bmatrix} \begin{bmatrix} C_1^k \sin[K_k z_n] + C_2^k \cos[K_k z_n] \\ C_3^k \sinh[U_k z_n] + C_4^k \cosh[U_k z_n] \end{bmatrix}$$

When the nonhomogeneous term $S_g^k(z)$ is given by Eq. 4.2, the method of undetermined coefficients can be used to find the $P_g^k(z)$ in terms of quadratic polynomials. The resulting particular solution is

$$\begin{bmatrix} P_1^k(z) \\ P_2^k(z) \end{bmatrix} = \begin{bmatrix} p_1^k & p_2^k \\ q_1^k & q_2^k \end{bmatrix} \begin{bmatrix} z^2 \\ z \end{bmatrix} + \begin{bmatrix} p_3^k \\ q_3^k \end{bmatrix}$$

where the coefficients p_i^k and q_i^k are functions of $Q_{g_j}^k$ and cross sections, and are given in Appendix 2.2. Hence, the general solution is

$$\begin{bmatrix} \bar{\phi}_1^k(z) \\ \bar{\phi}_2^k(z) \end{bmatrix} = \begin{bmatrix} H_1^k(z) \\ H_2^k(z) \end{bmatrix} + \begin{bmatrix} P_1^k(z) \\ P_2^k(z) \end{bmatrix} \quad k = r, u, w \quad (4.3)$$

where

$$\begin{aligned} z_n &= z_2 - z && \text{for } k = u \\ &= z_c - z && \text{for } k = w \\ &= z - z_c && \text{for } k = r \end{aligned}$$

are to be substituted for convenience.

The corresponding current solution is given by

$$\begin{bmatrix} \bar{J}_1^k(z) \\ \bar{J}_2^k(z) \end{bmatrix} = - \begin{bmatrix} D_1^k & D_1^k \\ D_2^k r^k & D_2^k s^k \end{bmatrix} \frac{d}{dz} \begin{bmatrix} C_1^k \sin[K_k z_n] + C_2^k \cos[K_k z_n] \\ C_3^k \sinh[U_k z_n] + C_4^k \cosh[U_k z_n] \end{bmatrix} - \begin{bmatrix} 2D_1^k p_1^k & D_1^k p_2^k \\ 2D_2^k q_1^k & D_2^k q_2^k \end{bmatrix} \begin{bmatrix} z \\ 1 \end{bmatrix} \quad (4.4)$$

To solve for the twelve constants C_j^k which yield fluxes in the three regions, we use eight equations from the flux and current continuities at two interfaces of the three regions, r , u and w , and four more equations from the boundary conditions at z_1 and z_3 . At these boundaries the surface-averaged currents known from the

available nodal solution are taken as the boundary conditions.

The flux continuity at the interfaces gives

$$\begin{aligned}
 & \left[\begin{array}{cc} 1 & 1 \\ r^u & s^u \end{array} \right] \left[\begin{array}{c} C_2^u \\ C_4^u \end{array} \right] - \left[\begin{array}{cc} 1 & 1 \\ r^w & s^w \end{array} \right] \left[\begin{array}{cc} \frac{1}{K_w} \sin [K_w(z_c - z_2)] & 0 \\ 0 & \sinh [U_w(z_c - z_2)] \end{array} \right] \left[\begin{array}{c} C_1^w K_w \\ C_3^w \end{array} \right] \\
 & - \left[\begin{array}{cc} 1 & 1 \\ r^w & s^w \end{array} \right] \left[\begin{array}{cc} \cos [K_w(z_c - z_2)] & 0 \\ 0 & \cosh [U_w(z_c - z_2)] \end{array} \right] \left[\begin{array}{c} C_2^w \\ C_4^w \end{array} \right] \\
 & = \left[\begin{array}{cc} p_1^w - p_1^u & p_2^w - p_2^u \\ q_1^w - q_1^u & q_2^w - q_2^u \end{array} \right] \left[\begin{array}{c} z_2^2 \\ z_2 \end{array} \right] + \left[\begin{array}{c} p_3^w - p_3^u \\ q_3^w - q_3^u \end{array} \right]
 \end{aligned} \tag{4.5a}$$

and

$$\left[\begin{array}{cc} 1 & 1 \\ r^w & s^w \end{array} \right] \left[\begin{array}{c} C_2^w \\ C_4^w \end{array} \right] - \left[\begin{array}{cc} 1 & 1 \\ r^r & s^r \end{array} \right] \left[\begin{array}{c} C_2^r \\ C_4^r \end{array} \right] = \left[\begin{array}{cc} p_1^r - p_1^w & p_2^r - p_2^w \\ q_1^r - q_1^w & q_2^r - q_2^w \end{array} \right] \left[\begin{array}{c} z_c^2 \\ z_c \end{array} \right] + \left[\begin{array}{c} p_3^r - p_3^w \\ q_3^r - q_3^w \end{array} \right]
 \tag{4.5b}$$

Also the current continuity yields

$$\begin{aligned}
 & \left[\begin{array}{cc} D_1^u & U_u D_1^u \\ r^u D_2^u & U_u s^u D_2^u \end{array} \right] \left[\begin{array}{c} C_1^u K_u \\ C_3^u \end{array} \right] - \left[\begin{array}{cc} D_1^w & U_w D_1^w \\ r^w D_2^w & U_w s^w D_2^w \end{array} \right] \times \\
 & \left[\begin{array}{cc} \cos [K_w(z_c - z_2)] & 0 \\ 0 & \cosh [U_w(z_c - z_2)] \end{array} \right] \left[\begin{array}{c} C_1^w K_w \\ C_3^w \end{array} \right] \\
 & - \left[\begin{array}{cc} D_1^w & U_w D_1^w \\ r^w D_2^w & U_w s^w D_2^w \end{array} \right] \left[\begin{array}{cc} -K_w \sin [K_w(z_c - z_2)] & 0 \\ 0 & \sinh [U_w(z_c - z_2)] \end{array} \right] \left[\begin{array}{c} C_2^w \\ C_4^w \end{array} \right]
 \end{aligned}$$

$$= \begin{bmatrix} D_1^u p_1^u - D_1^w p_1^w & D_1^u p_2^u - D_1^w p_2^w \\ D_2^u q_1^u - D_2^w q_1^w & D_2^u q_2^u - D_2^w q_2^w \end{bmatrix} \begin{bmatrix} 2z_2 \\ 1 \end{bmatrix} \quad (4.5c)$$

and

$$\begin{aligned} & \begin{bmatrix} D_1^w & U_w D_1^w \\ r^w D_2^w & U_w s^w D_2^w \end{bmatrix} \begin{bmatrix} C_1^w K_w \\ C_3^w \end{bmatrix} + \begin{bmatrix} D_1^r & U_r D_1^r \\ r^r D_2^r & U_r s^r D_2^r \end{bmatrix} \begin{bmatrix} C_1^r K_r \\ C_3^r \end{bmatrix} \\ & = \begin{bmatrix} D_1^w p_1^w - D_1^r p_1^r & D_1^w p_2^w - D_1^r p_2^r \\ D_2^w q_1^w - D_2^r q_1^r & D_2^w q_2^w - D_2^r q_2^r \end{bmatrix} \begin{bmatrix} 2z_c \\ 1 \end{bmatrix}. \end{aligned} \quad (4.5d)$$

The surface-averaged currents known at z_1 and z_3 give four additional conditions:

$$\begin{aligned} & - \begin{bmatrix} 1 & -U_u \\ r^u & -s^u U_u \end{bmatrix} \begin{bmatrix} K_u \sin [K_u(z_2 - z_1)] & 0 \\ 0 & \sinh [U_u(z_2 - z_1)] \end{bmatrix} \begin{bmatrix} C_2^u \\ C_4^u \end{bmatrix} \\ & + \begin{bmatrix} 1 & U_u \\ r^u & s^u U_u \end{bmatrix} \begin{bmatrix} \cos [K_u(z_2 - z_1)] & 0 \\ 0 & \cosh [U_u(z_2 - z_1)] \end{bmatrix} \begin{bmatrix} C_1^u K_u \\ C_3^u \end{bmatrix} \\ & = \begin{bmatrix} p_1^u & p_2^u \\ q_1^u & q_2^u \end{bmatrix} \begin{bmatrix} 2z_1 \\ 1 \end{bmatrix} + \begin{bmatrix} \bar{J}_1^u(z_1)/D_1^u \\ \bar{J}_2^u(z_1)/D_2^u \end{bmatrix} \end{aligned} \quad (4.5e)$$

and

$$- \begin{bmatrix} 1 & U_r \\ r^r & s^r U_r \end{bmatrix} \begin{bmatrix} \cos [K_r(z_3 - z_c)] & 0 \\ 0 & \cosh [U_r(z_3 - z_c)] \end{bmatrix} \begin{bmatrix} C_1^r K_r \\ C_3^r \end{bmatrix}$$

$$\begin{aligned}
& - \begin{bmatrix} 1 & U_r \\ r^r & s^r U_r \end{bmatrix} \begin{bmatrix} -K_r \sin [K_r(z_3 - z_c)] & 0 \\ 0 & \sinh [U_r(z_3 - z_c)] \end{bmatrix} \begin{bmatrix} C_2^r \\ C_4^r \end{bmatrix} \\
& = \begin{bmatrix} p_1^r & p_2^r \\ q_1^r & q_2^r \end{bmatrix} \begin{bmatrix} 2z_3 \\ 1 \end{bmatrix} + \begin{bmatrix} \bar{J}_1^r(z_3)/D_1^r \\ \bar{J}_2^r(z_3)/D_2^r \end{bmatrix}.
\end{aligned}$$

(4.5f)

where $C_j^k K_k$ are combined to avoid imaginary numbers. And there are six unknown two-element column vectors in six equations, Eq. 4.5:

$$\begin{bmatrix} C_1^u K_u \\ C_3^u \end{bmatrix}, \begin{bmatrix} C_2^u \\ C_4^u \end{bmatrix}, \begin{bmatrix} C_1^w K_w \\ C_3^w \end{bmatrix}, \begin{bmatrix} C_2^w \\ C_4^w \end{bmatrix}, \begin{bmatrix} C_1^r K_r \\ C_3^r \end{bmatrix} \text{ and } \begin{bmatrix} C_2^r \\ C_4^r \end{bmatrix},$$

The nonhomogeneous system, Eq. 4.5, is consistent, and the unique solution can be obtained directly by the Gaussian elimination method. Actually, all twelve C_j^k are determined by solving twelve linear equations (4.5), and unique axial group fluxes and currents within the regions r, u and w are found from Eqs. 4.3 and 4.4, respectively. As boundary conditions, the volume-averaged group nodal fluxes are also acceptable instead of the surface currents. One of these two boundary conditions

is arbitrarily used in the Collector-Predictor method.

4.3.2 FWC and Axial Discontinuity Factors

In reconstruction of the axial flux shapes in the three regions within $z_1 \sim z_3$, homogeneous cross sections in regions r, w and u have been explicitly represented, and in general they may not be the same. This fact must be accounted for in transferring the flux shapes and predicting FWC and DF, if the homogenized parameters in regions w and u in the Collector (see Fig. 4.2a) are not the same as those of region w' in the Predictor. When the axial flux shape from the Collector is edited out and transferred to the Predictor, the axial current at z_B' in the Predictor should be predicted from the flux (Eq. 4.3) and the diffusion coefficient of region w' (same as that of w) instead of the diffusion coefficient of region u. That is

$$\bar{J}_g^{\text{PRN}}(z_B') \approx -D_g^w \frac{d}{dz} \bar{\phi}_g^u(z) \Big|_{z=z_B'} \quad (4.6)$$

This correction is especially useful in BWR's where the void fraction distribution makes the axial homogenized cross sections non-uniform. Even in PWR's, this correction is desirable if axially non-uniform fuel depletion has occurred. If the distance, $z_2 - z_B$ (the displacement of the control rod per time step in the transient case),

is shorter compared to h_z^{PRN} , the estimated current at z'_B becomes more accurate.

The same idea can also be applied in determining FWC. Transferring only the axial flux shapes yields the FWC of the PRN in the Predictor (Fig. 4.2):

$$\bar{\Sigma}_{\alpha g}^{\text{PRN}} = \frac{\sum_{\alpha g}^W \left(\int_{z_B}^{z_2} \bar{\phi}_g^u(z) dz + \int_{z_2}^{z_C} \bar{\phi}_g^w(z) dz \right) + \sum_{\alpha g}^R \int_{z_C}^{z_T} \bar{\phi}_g^r(z) dz}{h_z \bar{\phi}_g^{\text{PRN}}} \quad (4.7)$$

where

$$\bar{\phi}_g^{\text{PRN}} = \frac{1}{h_z} \left(\int_{z_B}^{z_2} \bar{\phi}_g^u(z) dz + \int_{z_2}^{z_C} \bar{\phi}_g^w(z) dz + \int_{z_C}^{z_T} \bar{\phi}_g^r(z) dz \right) \quad (4.8)$$

Given $\bar{\Sigma}_{\alpha g}^{\text{PRN}}$, $\bar{\phi}_g^{\text{PRN}}$, $\bar{J}_g^{\text{PRN}}(z'_B)$ and $\bar{J}_g^{\text{PRN}}(z'_T)$, we can find homogenized surface fluxes at z'_B and z'_T if the corresponding transverse leakage shape within the new PRN were known. Finding the quadratic transverse leakage shape of the new PRN is not difficult if the average transverse leakages of the three regions (the rodded zone between z_T and z_3 , the unrodded zone between z_1 and z_B , and the new PRN between z_B and z_T as a homogenized node) are determined by partial integrations of the quadratic shapes that have already been found in the axial-flux reconstruction step. Then the transverse leakages in

Eq. 2.21 are replaced by

$$\begin{aligned}\bar{s}_{\ell-1} &= \frac{1}{z_B - z_1} \int_{z_1}^{z_B} s^u(z) dz \\ \bar{s}_{\ell+1} &= \frac{1}{z_3 - z_T} \int_{z_T}^{z_3} s^r(z) dz \\ \bar{s}_\ell &= \frac{1}{z_T - z_B} \left(\int_{z_B}^{z_2} s^u(z) dz + \int_{z_2}^{z_C} s^w(z) dz + \int_{z_C}^{z_T} s^r(z) dz \right)\end{aligned}\quad (4.9)$$

and the expansion functions, $\rho(u)$, are newly obtained from the three node sizes; $z_B - z_1$, $z_T - z_B$, and $z_3 - z_T$.

The resultant reaction rates (Eqs. 4.7 and 4.8) and surface leakage terms (Eqs. 4.6 and 4.9) of the new PRN are to be used to find the homogenized surface fluxes of the new PRN by preserving the reaction rates and the surface currents, and consequently the axial discontinuity factors. A complete set of equations are given in Appendix 2.3.

4.3.3 Radial Discontinuity Factors

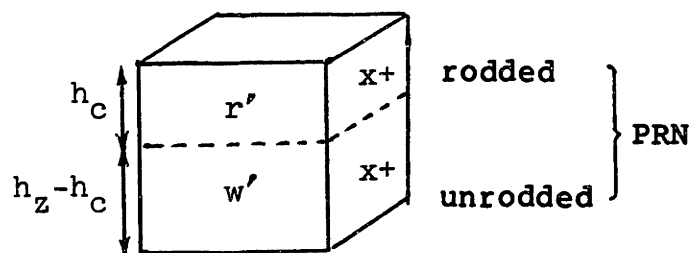
In addition to the homogenized cross sections and the axial discontinuity factors for the PRN, one needs to know the radial discontinuity factors. A rigorous three-dimensional problem for a system including the PRN could be solved for two-dimensional, radial flux

shapes to find the radial discontinuity factors. Fortunately, however, without any rigorous supplemental calculation, the radial discontinuity factors can be estimated by making use of the volume-averaged fluxes $\bar{\phi}_g^{r'}$ and $\bar{\phi}_g^{w'}$ for the two subregions of a PRN (r' and w' in Fig. 4.2b). As previously mentioned, the radially homogenized cross sections and discontinuity factors for an axially uniform node are assumed to have been given already. The PRN in Fig. 4.2b is reproduced below for derivation of the radial discontinuity factors.

By definition, the heterogeneous surface flux, $\bar{\phi}_{x+}^{r',\text{het}}$, and the homogenized surface flux, $\bar{\phi}_{x+}^{r',\text{hom}}$, on the surface $x+$ of the subnode r' are related by

$$\bar{\phi}_{x+}^{r',\text{het}} = f_{x+}^{r'} \bar{\phi}_{x+}^{r',\text{hom}} \quad (4.10a)$$

Similarly, for the unrodded subnode w' , we have



($x+$ designates positive-x-directed surface)

$$\bar{f}_{x+}^{w', \text{het}} = f_{x+}^{w'} - \bar{f}_{x+}^{w', \text{hom}}$$

(4.10b)

And for the complete PRN,

$$f_{x+}^{\text{PRN}} = \frac{\bar{f}_{x+}^{\text{PRN}, \text{het}}}{\bar{f}_{x+}^{\text{PRN}, \text{hom}}}$$

(4.10c)

The physically true heterogeneous surface flux on the surface $x+$ of the PRN can be expressed in terms of its counterparts for the subnodes r' and w' ,

$$\bar{f}_{x+}^{\text{PRN}, \text{het}} = \left(\frac{h_c}{h_z} \right) \bar{f}_{x+}^{r', \text{het}} + \left(1 - \frac{h_c}{h_z} \right) \bar{f}_{x+}^{w', \text{het}}$$

(4.11a)

For the homogenized surface fluxes, no such exact relationship exists. Nevertheless, we assume that the homogenized surface fluxes may be approximated by the same relationship as the heterogeneous surface fluxes:

$$\bar{f}_{x+}^{\text{PRN}, \text{hom}} \approx \left(\frac{h_c}{h_z} \right) \bar{f}_{x+}^{r', \text{hom}} + \left(1 - \frac{h_c}{h_z} \right) \bar{f}_{x+}^{w', \text{hom}}$$

(4.11b)

Thus, substitution of Eq. 4.11 into Eq. 4.10c yields

$$f_{x+}^{PRN} \approx \frac{f_{x+}^{r'} + \left(\frac{h_z}{h_c} - 1 \right) \left(\begin{array}{c} -w', \text{hom} \\ \phi_{x+}^r \end{array} \right) f_{x+}^{w'}}{1 + \left(\frac{h_z}{h_c} - 1 \right) \left(\begin{array}{c} -w', \text{hom} \\ \phi_{x+}^w \end{array} \right)}$$

(4.12)

As a practical matter, the radial discontinuity factors, $f_{x+}^{r'}$ and $f_{x+}^{w'}$, are assumed to be independent of h_c , and are provided as input data from the two-dimensional assembly calculations.

The ratio of homogenized surface fluxes in regions r' and w' is, however, not known. Accordingly, we assumed that the ratio of homogenized surface fluxes can be approximated by the ratio of corresponding volume-averaged fluxes:

$$\frac{\phi_{x+}^{-w', \text{hom}}}{\phi_{x+}^{-r', \text{hom}}} \approx \frac{\phi^{-w'}}{\phi^{-r'}}$$

Substituting this into Eq. 4.12 results in

$$f_{x+}^{PRN} \approx \frac{h_c f_{x+}^{r' = r'} + (h_z - h_c) f_{x+}^{w' = w'}}{h_z^{\phi = PRN}}$$

(4.13)

which is the sum of the radial discontinuity factors of the two subnodes weighted by the volume fluxes of those subnodes.

Many test results have shown that this approximation is acceptable. Two such tests are shown in Tables 4.1 and 4.2 for a 3 X 3 X 3 symmetric system (Fig. 3.3) and an asymmetric system (Fig. 3.7), respectively.

For these tests, the non-unity radial discontinuity factors in the x- and y- directions from the assembly calculations (ADF) were used in addition to the AXS given in Table 3.1. The accuracy of the volume-flux-weighted radial discontinuity factors has been found to be greater than 99% for most estimations for the PRN of the symmetric or asymmetric 3 X 3 X 3 systems.

As a first test of the overall scheme, an extended 3 X 3 X 4 symmetric system (axial node sizes = 10, 20, 20 and 10 cm from the bottom) with a control rod fully inserted into the upper two nodes was solved for information needed in Collector step, and then Method 1 was applied to obtain FWC and three-dimensional discontinuity factors for PRN's in 3 X 3 X 3 symmetric and asymmetric systems. Results are shown in Table 4.3. For either a symmetric or an asymmetric system, errors in eigenvalues are much less than 0.01% and the accuracy in nodal power is greater than 99%. The largest error occurs when the control

Table 4.1 The Volume-Flux-Weighted Radial Discontinuity Factors for a PRN of a 3 X 3 X 3 Symmetric System (Fig. 3.3).

control rod tip position h_c (cm)	group g	exact f_{xg}^{\pm}	volume- flux- weighted f_{xg}^{\pm}	error (%)
0.0	1	1.0030	1.0030	0.0
	2	0.9380	0.9380	0.0
5.0	1	1.0080	1.0078	-0.020
	2	0.9757	0.9750	-0.072
10.0	1	1.0132	1.0130	-0.020
	2	1.0191	1.0180	-0.110
15.0	1	1.0189	1.0188	-0.010
	2	1.0736	1.0726	-0.093
17.5	1	1.0219	1.0218	-0.010
	2	1.1056	1.1049	-0.063
20.0	1	1.0250	1.0250	0.0
	2	1.1390	1.1390	0.0

(Because of the symmetry of the system,
 $f_x^+ = f_x^-$, $f_y^+ = f_x^+$ and $f_y^- = f_x^-$ for
all energy groups and for all h_c .)

Table 4.2 Radial Discontinuity Factors for Three PRN's of a 3 X 3 X 3 Asymmetric System (Fig. 3.7).

control rod tip position h_c (cm)	location of PRN	group g	exact* f_{xg}^{\pm} or f_{yg}^{\pm}	volume-flux-weighted** $f_{xg}^{\pm}; f_{yg}^{\pm}$	max. error (%)
0.0	right	1	1.0030	1.0030	0.0
		2	0.9380	0.9380	0.0
	front	1	1.0030	1.0030	0.0
		2	0.9380	0.9380	0.0
	left	1	1.0030	1.0030	0.0
		2	0.9284	0.9284	0.0
10.0	right	1	1.0118 ~ 1.0135	1.0124	-0.11
		2	1.0123 ~ 1.0149	1.0125	-0.24
	front	1	1.0122 ~ 1.0125	1.0122	-0.03
		2	1.0109 ~ 1.0124	1.0109	-0.15
	left	1	1.0111 ~ 1.0131	1.0119	-0.12
		2	1.0004 ~ 1.0026	0.9999	-0.27
18.0	right	1	1.0220 ~ 1.0226	1.0222	-0.04
		2	1.1087 ~ 1.1100	1.1089	-0.10
	front	1	1.0218 ~ 1.0225	1.0221	-0.04
		2	1.1075 ~ 1.1092	1.1079	-0.12
	left	1	1.0211 ~ 1.0218	1.0213	-0.05
		2	1.0919 ~ 1.0934	1.0905	-0.27
20.0	right	1	1.0250	1.0250	0.0
		2	1.1390	1.1390	0.0
	front	1	1.0250	1.0250	0.0
		2	1.1390	1.1390	0.0
	left	1	1.0240	1.0240	0.0
		2	1.1210	1.1210	0.0

* $f_x^{\pm} = f_y^{\pm}$ for h_c and $h_c = 20$ cm from assembly calculations, and the ranges of f_x^{\pm} and f_y^{\pm} are shown for other values of h_c .

** $f_x^{\pm} = f_y^{\pm}$ for all h_c values and all energy groups.

Table 4.3 **Test of the Use of Volume-Flux-Weighted Radial Discontinuity Factors (VFWRDF) along with FWC and Axial Discontinuity Factors.**

system tested	h_c (cm)	k_{eff}			max. error in nodal power
		exact	VFWRDF	error	
symmetric $3 \times 3 \times 3$	10.0	0.97006	0.97004	-0.002%	0.32%
	17.5	0.96671	0.96671	0.0	0.17%
asymmetric $3 \times 3 \times 3$ *	10.0	0.95210	0.95202	-0.008%	0.95%
	18.0	0.94185	0.94184	-0.001%	0.46%
asymmetric $3 \times 3 \times 3$ **		0.95205	0.95203	-0.002%	0.65%

*with all three control rods at the same level.

**The control rod levels in three PRN's are different; $h_c = 10, 18,$ and 3 cm for left, front, and right, respectively (see Fig. 3.7).

rod is inserted to around the midpoint of the PRN. The remarkable accuracy resulting from use of volume-flux-weighted radial discontinuity factors will also be demonstrated for realistic problems in the next chapter.

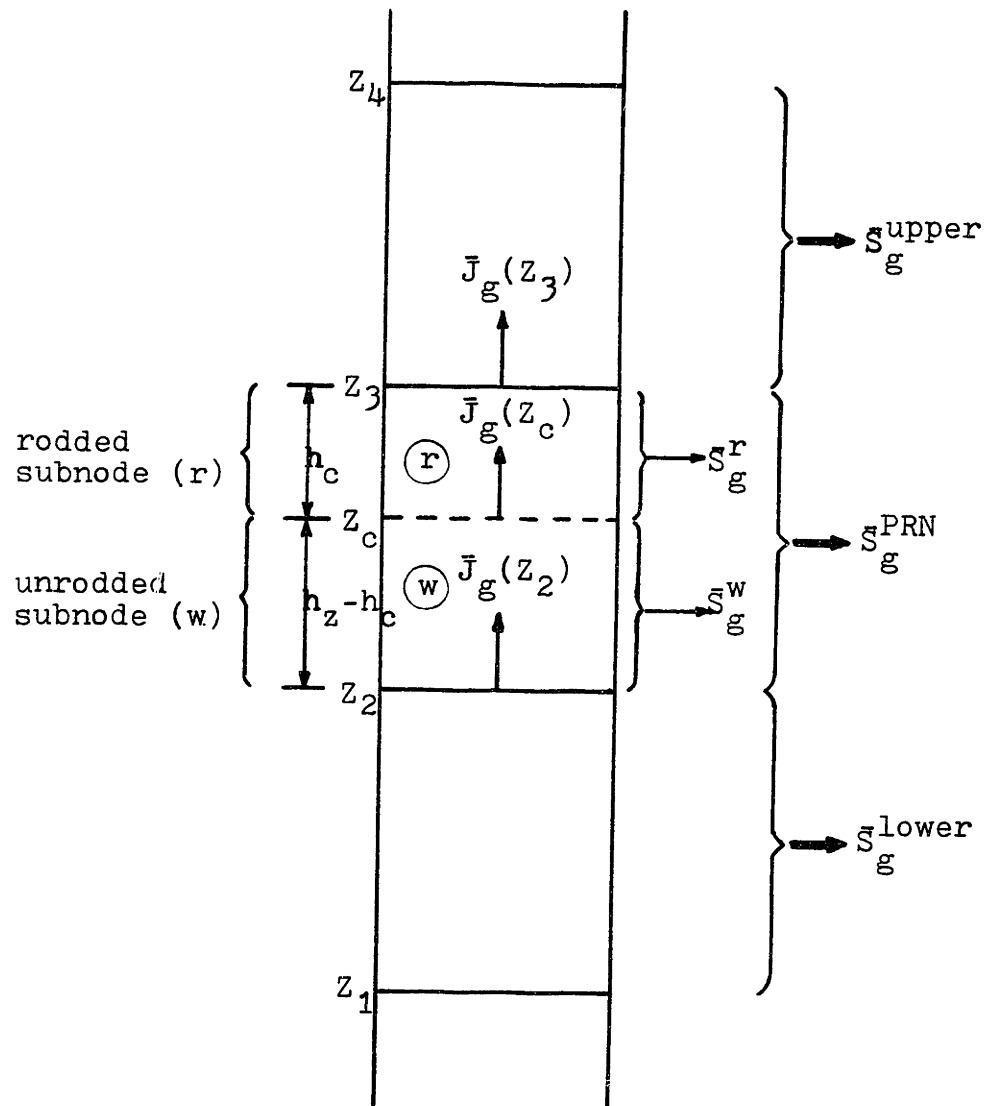
4.4 Transverse Leakage from a Partially Rodded Node

The quadratic shaped-transverse leakage has been used for axial flux reconstruction within a PRN under the assumption that the average transverse leakages from the adjacent five nodes (including two subnodes in the PRN) are known. Actually, among these five nodes, the average transverse leakages from the two subnodes of the PRN (r and w in Fig. 4.2a) cannot be found directly from the global nodal solution. Only the average leakage from the whole PRN is known.

4.4.1 Finding Transverse Leakages for Two Subnodes of a Partially Rodded Node

In solving Eq. 4.1 for axial flux shapes, the average transverse leakages \bar{S}_g^r and \bar{S}_g^w from the subnodes r and w are not known (Fig. 4.3). Four approximations for finding them will be considered.

The simplest approximation is to assume that \bar{S}_g^r and \bar{S}_g^w are spatially flat and equal to the average radial leakage, \bar{S}_g^{PRN} , from the PRN (called Method 2F). The sudden changes in the transverse leakages at the vicinity of



g =energy group

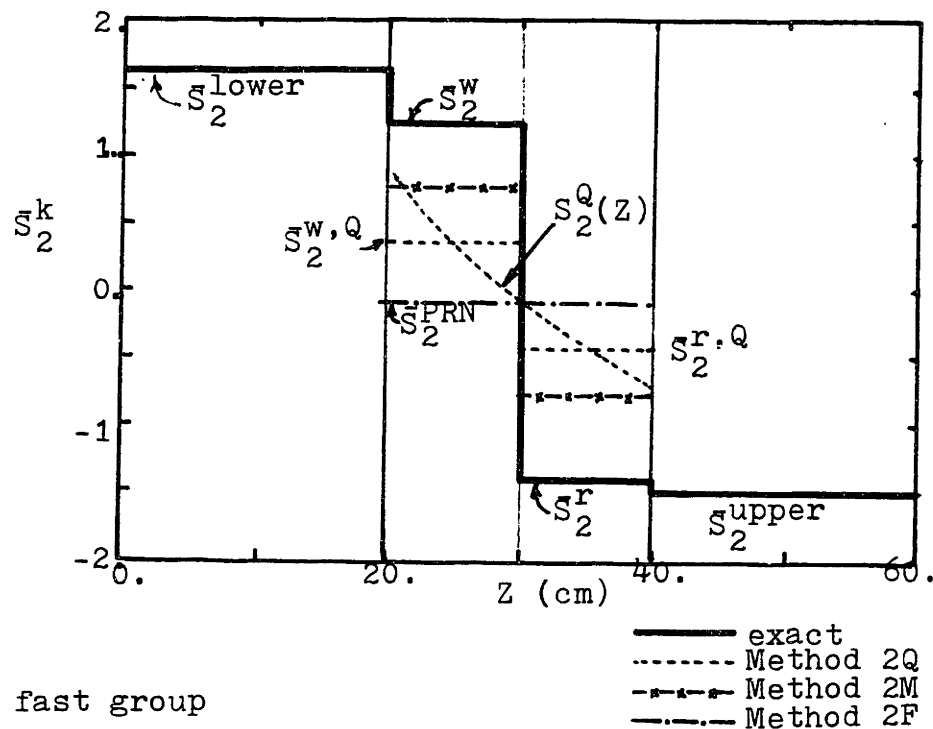
Figure 4.3 Axial currents and average transverse leakages from the nodes in a rodded assembly.

the control rod tip makes this approximation unattractive.

An alternative to this flat approximation is to consider a quadratic approximation (Eq. 2.21) for the shape of the transverse leakage of the PRN based on the transverse leakages from the PRN and its lower and upper neighbors. One then can integrate the quadratic shape over each of the two subnodes r and w to estimate \bar{S}_g^r and \bar{S}_g^w . This method is called "Method 2Q".

For examination of Method 2Q, the symmetric system shown in Fig. 3.3a, was solved in the $3 \times 3 \times 4$ node layout for the average transverse leakages in the four nodes of the central rodded assembly. Figure 4.4 shows the group transverse leakages, \bar{S}_g^{lower} , \bar{S}_g^w , \bar{S}_g^r and \bar{S}_g^{upper} for $h_c = 10$ cm. The $S_g^Q(z)$ represents the quadratic transverse leakage shape in the PRN, and its averages in the subnodes w and r are $\bar{S}_g^{w,Q}$ and $\bar{S}_g^{r,Q}$. Even for the simple $3 \times 3 \times 3$ system, the quadratic approximation results in poor accuracy in estimating the average transverse leakages from the subnodes. For the thermal group the error is nearly 70%, and it is about 40% for the fast group. Because the thermal group neutrons play an important role in the control rod cusping problem in LWR, the quadratic approximation seems to be unfavorable in estimating \bar{S}_g^w and \bar{S}_g^r .

(a) thermal group



(b) fast group

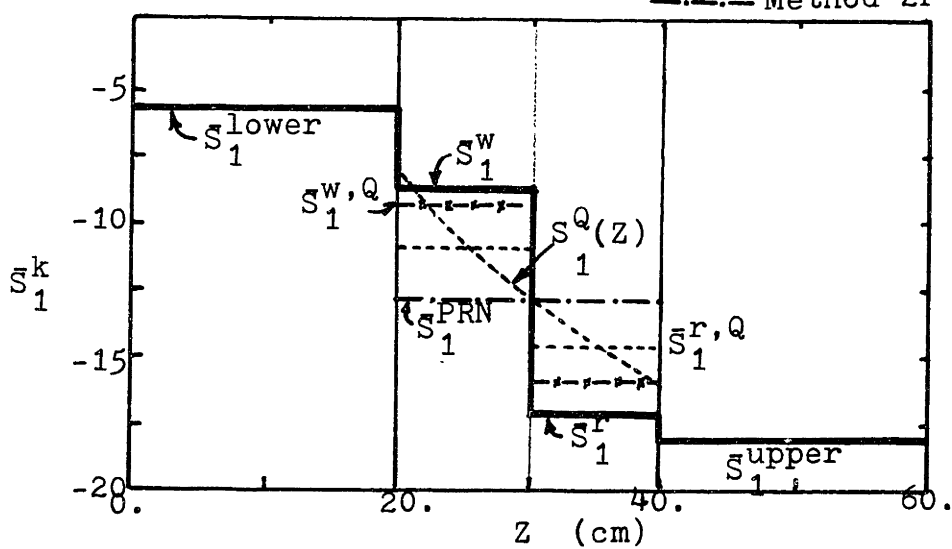


Figure 4.4 Average transverse leakage from the nodes in the rodded assembly of a $3 \times 3 \times 3$ symmetric system ($h_c = 10$ cm and leakages, \bar{S}_g^k , in normalized scale).

Some not consistent improvement in determining \bar{S}_g^W and \bar{S}_g^R from \bar{S}_g^{PRN} can be obtained if \bar{S}_g^W and \bar{S}_g^R are estimated by taking the averages of \bar{S}_g^{PRN} and \bar{S}_g^{lower} and \bar{S}_g^{upper} (called Method 2M) as follows:

$$\bar{S}_g^W \approx \frac{1}{2} (\bar{S}_g^{PRN} + \bar{S}_g^{\text{lower}})$$

$$\bar{S}_g^R \approx \frac{1}{2} (\bar{S}_g^{PRN} + \bar{S}_g^{\text{upper}})$$

For the $3 \times 3 \times 3$ system, one can see from Fig. 4.4 that this average approximation slightly improves the accuracy compared to the quadratic approximation (compare the dotted line with the dotted line with cross). This average approximation does not guarantee that the total transverse leakage of the PRN is preserved when the resultant \bar{S}_g^R and \bar{S}_g^W are themselves averaged. Thus, the average approximation violates neutron balance within the PRN, and may cause unphysical flux reconstruction.

Thus the first three approaches are direct but deficient. A more rigorous but indirect approach can be established if neutron balance within the PRN and some conditions associated with the node face at z_c in Fig. 4.3 are incorporated into a relationship between \bar{S}_g^W , \bar{S}_g^R and \bar{S}_g^{PRN} (called Method 2J):

$$\bar{S}_g^{PRN} = \left(1 - \frac{h_c}{h_z} \right) \bar{S}_g^W + \left(\frac{h_c}{h_z} \right) \bar{S}_g^R \quad (4.14)$$

This relationship specifies the surface averaged transverse leakage of the PRN, and is exact. If one additional relationship between \bar{S}_g^w and \bar{S}_g^r could be found, then the magnitudes of \bar{S}_g^w and \bar{S}_g^r can be determined. To do so, we consider the neutron balance in the subnode r. Rewriting Eq. 2.7 yields

$$\begin{aligned} & \frac{1}{h_c} \left(\bar{J}_g(z_3) - \bar{J}_g(z_c) \right) + \sum_{t_g}^r \bar{\phi}_g^r \\ & - \sum_{g'=1}^2 \left(\frac{1}{k_{\text{eff}}} \chi_g v \sum_{f_g}^r + \sum_{gg'}^r \right) \bar{\phi}_g^r = -\bar{S}_g^r \end{aligned} \quad (4.15)$$

From the available global nodal solution for the Collector step, $\bar{J}_g(z_3)$ and cross sections of the subnode r are known, but $\bar{\phi}_g^r$ and $\bar{J}_g(z_c)$ are not. The average flux, $\bar{\phi}_g^r$, in region r can be obtained from the two equations;

$$\bar{\phi}_g^{\text{PRN}} = \left(1 - \frac{h_c}{h_z} \right) \bar{\phi}_g^w + \left(\frac{h_c}{h_z} \right) \bar{\phi}_g^r \quad (4.16a)$$

and

$$\bar{\Sigma}_{t_g}^{\text{PRN}} \bar{\phi}_g^{\text{PRN}} = \left(1 - \frac{h_c}{h_z} \right) \bar{\Sigma}_{t_g}^w \bar{\phi}_g^w + \left(\frac{h_c}{h_z} \right) \bar{\Sigma}_{t_g}^r \bar{\phi}_g^r \quad (4.16b)$$

In the second equation, the absorption-plus-scattering reaction rate is used because of the significant difference between $\bar{\Sigma}_{t_g}^w$ and $\bar{\Sigma}_{t_g}^r$. Hence the only unknown in Eq. 4.15

is the axial net-current at the control rod tip, $\bar{J}_g(z_c)$. Provided $\bar{J}_g(z_c)$ is found, both \bar{S}_g^W and \bar{S}_g^R will be determined from Eqs. 4.14 and 4.15. Since the exact $\bar{J}_g(z_c)$ is not available, an approximation must be made. One approach is to make use of the fact that $J_g(z_c)$ does not change much if there are small changes in h_c . In the transient problem, the change in h_c per time step is negligible compared with the node size. Hence, $\bar{J}_g(z_c)$ obtained in the Predictor step of the previous time step ($n-1$) can provide the approximate $\bar{J}_g(z_c)$ for the present time step (n):

$$\bar{J}_g^{(n)}(z_c) \approx \bar{J}_g^{(n-1)}(z_c) \left[\begin{array}{c} \text{total power (n)} \\ \text{total power (n-1)} \end{array} \right] \quad (4.17)$$

Normalization by total reactor power is necessary at each time step because of power transient. If the $\bar{J}_g(z_c)$ is predicted accurately by the scheme for every step, the \bar{S}_g^W and \bar{S}_g^R will be estimated correctly.

The accuracy of the methods introduced in this section will be discussed in the next chapter for several transient problems.

4.4.2 Partially Rodded Surface-Nodes

Because the shape of the transverse leakage within a subnode of a PRN is expressed as a quadratic polynomial the shape of which is specified by the node-averaged

transverse leakages of three adjacent nodes, a problem arises for PRN's located on the reactor core surface.

If the top and bottom reflectors are represented as explicit regions, the transverse leakage of the reflector node can be used directly as the third leakage term. For problems without axial reflectors, however, a fictitious external nodal leakage value is necessary, and it must reflect somehow the boundary conditions of the problem.

For problems with a zero-flux boundary condition, the fictitious flux in a fictitious external node might have a negative value if the flux distribution in the surface PRN were extrapolated into the external node. If the transverse leakage from the PRN is to fall off towards zero at the external zero-flux boundary, it seems plausible to set the transverse leakage of the fictitious external node equal to the negative of the transverse leakage of the surface PRN.

For problems with zero net-current boundary conditions, we may construct a fictitious mirror node next to the surface PRN. This mirror node is then taken to have the same average transverse leakage as that of the surface PRN.

An albedo boundary condition may be applied at the interface of the core and top or bottom reflector, having the form [K-3]

$$\bar{\phi}_g^z = \alpha_g \bar{J}_g^z$$

where α_g is the ratio of net-current in z-direction and flux at the interface, and is constant along the interface. For this situation it has been proved [S-4] that the axial power distribution is almost insensitive to the transverse leakage in the reflector node. Hence, the transverse leakage of the fictitious external node can be assumed to be zero to determine the quadratic transverse leakage shape in a subnode within the PRN. Parsons [P-1] has verified that this procedure results in sufficient accuracy for two-dimensional problems with the radial reflector replaced by albedo boundary condition.

4.5 The QUANDRY Code and the Collector-Predictor Method

4.5.1 The QUANDRY Code

QUANDRY solves the two-group, steady-state and transient nodal diffusion equations with thermal-hydraulic feedback. The nodal diffusion equations are coupled to the heat conduction and transfer equations for a simple lumped-heat-capacity fuel pin and coolant channel model.

The steady-state problem is solved by a fission source iteration which is accelerated by use of Wielandt's fractional iteration [W-3], and the time-dependent neutronics solution is found by use of the theta method time-integration scheme. The advanced fluxes at each time step are obtained by solving the point kinetics equations and using the

theta method extrapolation. The node-averaged flux distribution is found by a Gauss-Seidel iteration. To enhance convergence of the flux iteration, the Cyclic Chebychev Semi-Iterative (CCSI) method is applied in both steady-state and time-dependent solution methods. In most transient problems, less than five flux iterations are required to achieve an error-reduction of 10^{-3} in the nodal fluxes. However, a large number of iterations may be required when sudden movements of the control rods take place or in the time domains near power extrema because the extrapolated fluxes by the theta method are poor estimates of the actual fluxes in these cases.

The analytic nodal method embodied in the QUANDRY code provides an accurate solution of the neutronics equations. However, the simple lumped-heat-capacity thermal-hydraulics model is not suitable for realistic LWR analyses, especially for BWR analysis with boiling. Because of this fact, the actual application of the aforementioned methods for resolution of the control rod cusping problem will be limited to transient problems with no thermal-hydraulic feedback. If resolution of the control rod cusping problem is achieved for transient neutronics problems, the same method ought to be accurate when thermal-hydraulic effects are accounted for.

4.5.2 The Transient Routine and its Extension

The subroutine TRAN in the QUANDRY code is the transient calculation driver. This routine controls the initialization of the transient parameters and sets the control logic to be passed to operational subroutines. The neutronics transient control flow is basically the following:

- (1) Set up the matrices for time step (n) by making use of all information calculated in the previous time step.
- (2) Update all the coupling matrices to reflect new homogenization parameters for perturbed nodes such as a partially rodded node.
- (3) Re-estimate the prompt flux and leakage extrapolation frequencies from the point-kinetics solution, and extrapolate the fluxes and leakages.
- (4) Calculate the transient fluxes iteratively using the CCSI method, and calculate the directional net leakages for each node.
;
- (5) Perform the node-wise delayed neutron precursor solutions for the next time step (n+1).
- (6) Normalize node-wise fluxes and leakages prior to commencing the subsequent time step.

In order to account for control rod cusping effects in QUANDRY, new homogenization parameters for the partially rodded node must be found and updated between steps (1)

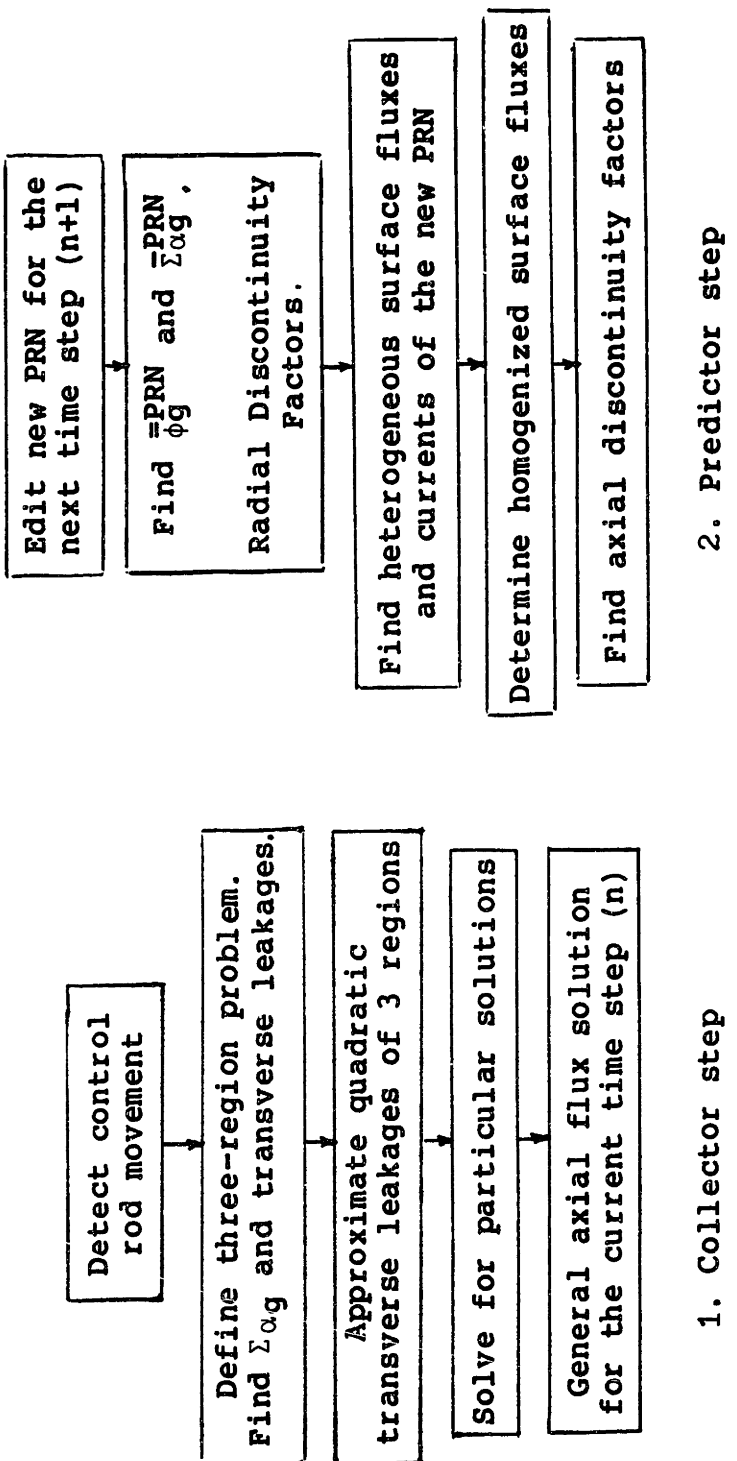


Figure 4.5 The Collector-Predictor method

and (2). In the subroutine PURTO which is called by TRAN, cross section perturbations and a partial coupling matrix update can be performed for a transient calculation with a moving control rod. The Collector-Predictor Method is written in the subroutine PURTO; the functional chart is shown in Fig. 4.5. Programming and calculations were done with the IBM 3033/N computer at M.I.T.

4.6 Summary

In this chapter, two new "Collector-Predictor" methods have been developed for determining the homogenization parameters of a partially rodded node, the aim being to resolve the control rod cusping problem in a practical and systematic way. The first method (Method 1) is rather simple. It is for steady state problems, but requires some local information from a solution of the same system with no partially rodded nodes. For this reason Method 2, which seems to be adequate for both static and transient problems, was introduced. For this scheme all the required information is internal to the QUANDRY solution. The basic idea of the methods is to use the QUANDRY solution to reconstruct the axial flux shape in a partially rodded node, and thereby to determine flux-weighted cross sections and axial discontinuity factors.

In order to apply the two Collector-Predictor schemes, the QUANDRY code has been changed and extended for transient

calculations relating to control rod motion. A brief explanation of the changes and additions was given.

In the next chapter, the Collector-Predictor method will be applied to several light water reactor benchmark problems in both static and transient cases.

Chapter 5

APPLICATION OF THE COLLECTOR-PREDICTOR METHOD

5.1 Introduction

The discussion in the previous two chapters explains that the use of discontinuity factors along with flux-weighted cross sections can eliminate the control rod cusping problem for QUANDRY computations. The possibility of making use of tabulation-interpolation methods was examined, but showed that these methods are problem-dependent, require additional complete global calculations and demand considerable machine memory space - all unattractive features.

In the last chapter, a new method was developed which is simple, systematic, reliable and problem-independent way (the Collector-Predictor method) to solve the control rod cusping problem using data internal to QUANDRY. This Collector-Predictor method as implemented in the QUANDRY code will be examined and evaluated in this chapter for several benchmark problems. Results obtained will be compared with those of both the volume-weighted cross section (VWC) approximation and the quadratic axial flux shape approximation currently programmed into the QUANDRY. Three-dimensional benchmark problems will first be introduced, and the use of the QUANDRY solutions as numerical standards

will then be justified by comparing with PDQ-7 solutions.

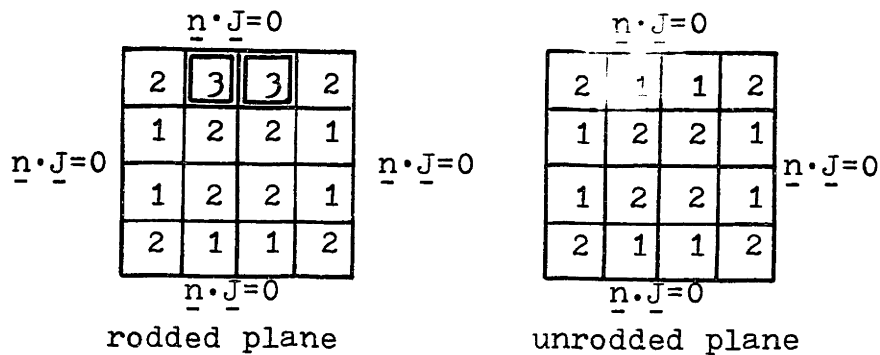
5.2 Three-Dimensional Models

Three three-dimensional benchmark problems are used in this chapter to test the Collector-Predictor method. These problems are representations of the inner portions of a typical PWR and two simplified BWR. The heterogeneous core zones are explicitly modeled. However, zero-current conditions are imposed at the radial boundaries.

5.2.1 The CC3-PWR Model

To examine the Collector-Predictor method for PWR's, a small three-dimensional problem, the CC3-PWR (Core Central region of a 3-dimensional PWR model) benchmark, was chosen [K-2]. Figure 5.1 describes the two distinct horizontal sections and vertical section of the model. The CC3-PWR model consists of the sixteen quarter-assemblies of two different fuel enrichments (compositions 1 and 2 in Fig. 5.1a) which are arranged in a checkerboard pattern. Four quarter-assemblies from a single fuel assembly are shown in Fig. 5.2. Each fuel assembly has 15 x 15 fuel cell locations, sixteen of which are either rodded or filled with coolant water. The central cell is non-fueled and unrodded. The two off-centered quarter-assemblies (designated as composition 3) are altered by the partial insertion of a control rod cluster. Zero

(a) horizontal sections



(b) vertical section

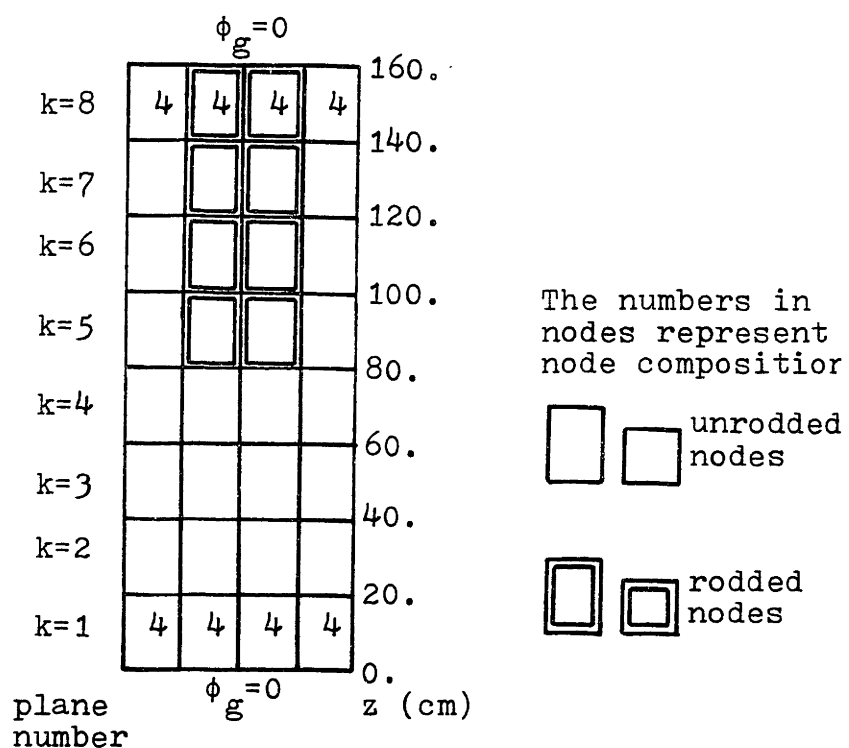
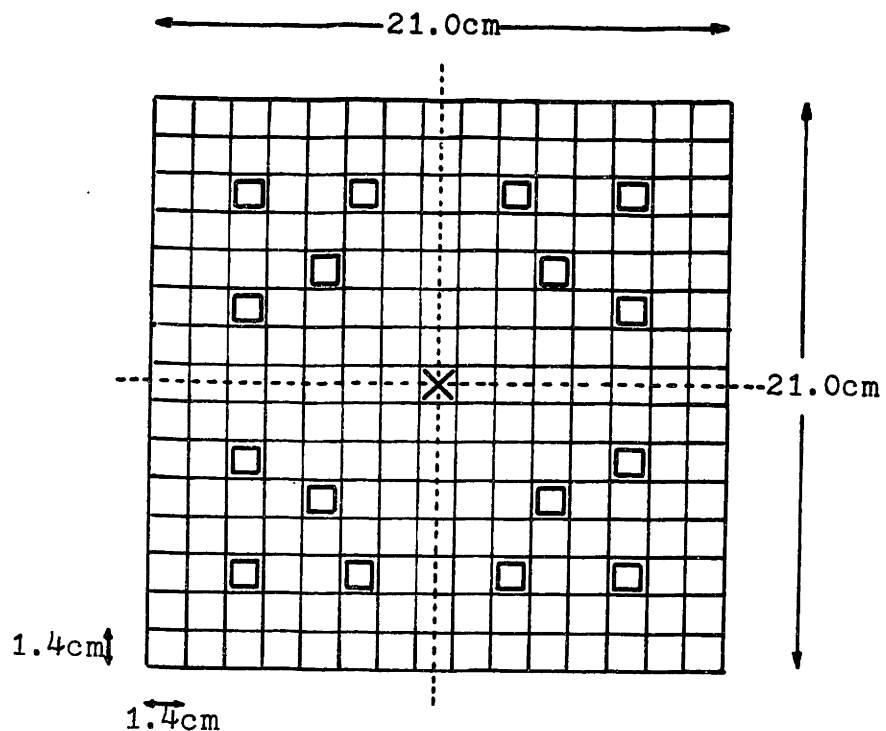


Figure 5.1 Horizontal and vertical sections of the 4 X 4 X 8 CC3-PWR model.



-----quarter assembly boundary

fueled cell

water hole

either rodded cell or water hole

Figure 5.2 Four heterogeneous quarter-assemblies (a single complete assembly) for the CC3-PWR model.

net-current boundary conditions are imposed at the four radial boundaries.

The vertical section of the model is divided into eight 20 cm nodes including reflector nodes at the top and bottom (shown as composition 4). Part of heterogeneous geometric detail of the two-dimensional plane is illustrated in a 16 X 32 mesh layout in Fig. A3.1 of Appendix 3. The heterogeneous two-group cross sections are provided in Table A3.1, Appendix 3. To avoid errors arising from use of isolated assembly calculations to compute radially homogenized cross sections and discontinuity factors, two-dimensional 16 X 32 fine-mesh calculations for full planes (Fig. A3.1 in Appendix 3) were carried out using QUANDRY. This was done for two different types of planes, one rodded and the other unrodded. The resultant homogenized nodal cross sections and corresponding radial discontinuity factors are listed in Table A3.2 of Appendix 3.

5.2.2 BWR Models

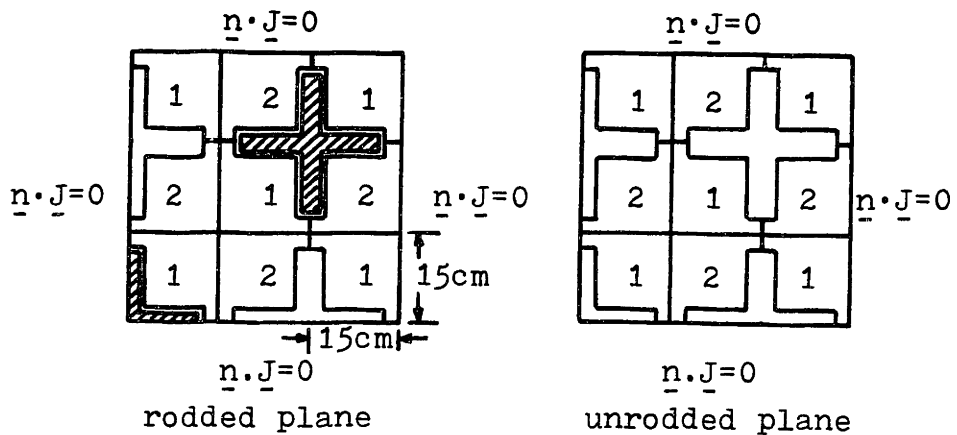
In the course of investigation of the control rod cusping problem in the previous two chapters, only simple homogenized models based on typical PWR properties were considered. From the point of view of radial heterogeneity, a BWR assembly complicated with a control blade, is more heterogeneous than its rodded PWR counterpart. Therefore, it is desirable to test Method 1 for a static BWR problem.

The CISE-BWR benchmark problem [S-5, F-5] was chosen for this purpose. Smith [S-5] showed that the CISE-BWR problem provides an example of the inaccuracy of the conventional flux-weighted parameters, and concluded that use of the discontinuity factors can improve the accuracy significantly. Hence, the CISE-BWR model is a good example for testing the Collector-Predictor method for which the discontinuity factors are an essential tool.

The CISE-BWR core consists of 208 fuel assemblies with widths of 15 cm. However, for the present test, only nine central assemblies are taken to form a 3 X 3 X 3 partially rodded benchmark problem. A detailed description of the model is given in Fig. 5.3. Zero net-current boundary conditions are imposed at all external nodal faces, and the axial node sizes are all 20 cm. Note that the definition of the variable h_c is different from that of Fig. 3.3. Flux-weighted cross sections and radial discontinuity factors are summarized in Table A4.1, Appendix 4. It can be seen that the values of the discontinuity factors are far from unity.

The CISE-BWR problem does not contain any void in the coolant, and this must be accounted for in more realistic BWR problems. There is a benchmark problem, the TRD-BWR model (three-dimensional BWR) composed of the Vermont

(a) horizontal sections (numbers represent fuel types)



(b) $3 \times 3 \times 3$ node system

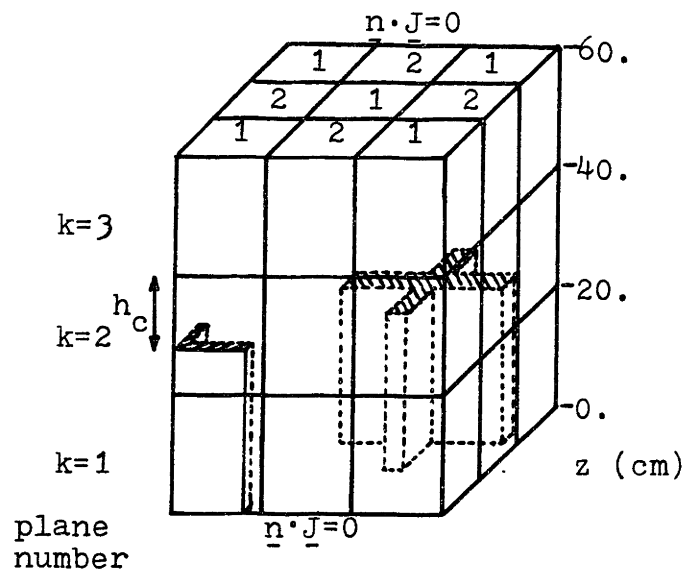
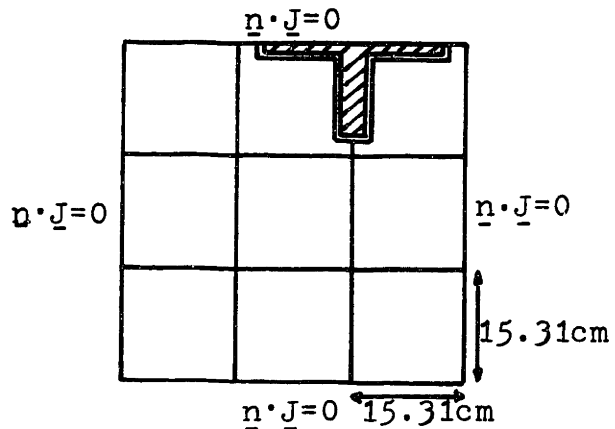


Figure 5.3 The $3 \times 3 \times 3$ CISE-BWR model.

Yankee assemblies, which does explicitly reflect the effects of axial void distribution. Finck [F-5] created and analyzed this model. He examined two-dimensional homogenized parameters, and proved numerically that the use of unity axial discontinuity factors in the TRD-BWR problem does not affect the accuracy of the nodal solutions. This fact is very important at the point of view of justifying the use of QUANDRY solutions as numerical standards in the following sections of this chapter. Because the TRD-BWR model represents well the characteristics of a realistic BWR with a control blade partially inserted and with several different regions of voiding, the TRD-BWR model will be used in evaluating the Collector-Predictor method.

Figure 5.4 shows a 3 X 3 X 10 core configuration for the TRD-BWR model. Two off-centered assemblies are partially rodded, and the core consists of eight planes involving four different regions of voiding. Void fractions of 0%, 40% and 70% are considered as shown in Table A4.3a, Appendix 4. The water reflectors are not voided, and the void fraction increases towards the top of the core. The assembly widths are 15.31 cm, and the axial core node sizes are 15 cm. The thickness of water reflectors were chosen to be 20 cm - enough to justify zero flux boundary conditions. Zero net-current radial boundary

(a) horizontal section



(b) vertical section

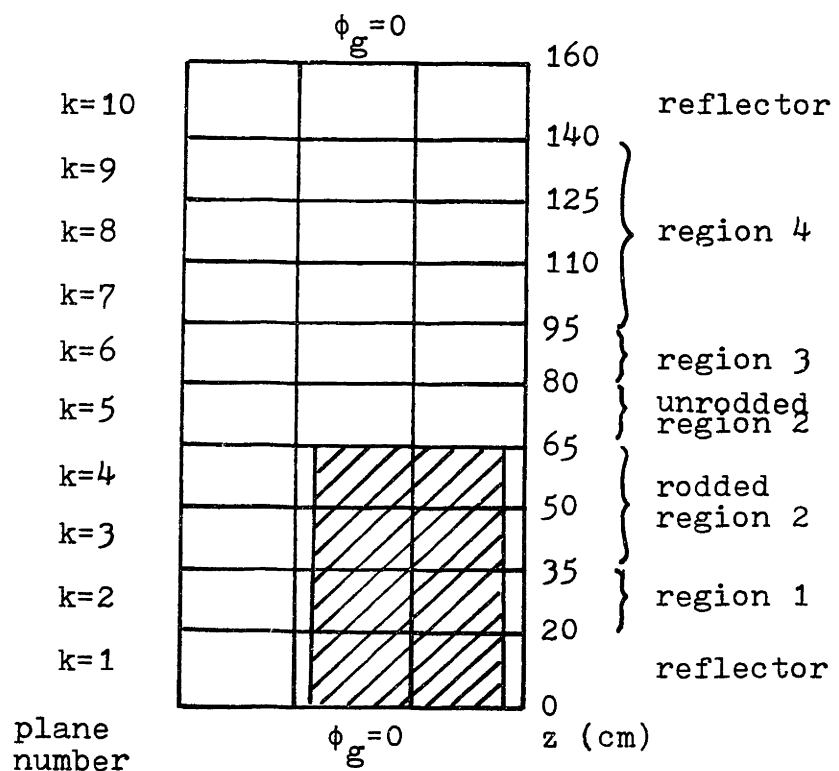


Figure 5.4 Core layout for the TRD-BWR.

conditions were imposed. The major simplifications in the TRD-BWR model are that the actual fuel heterogeneities (different fuel enrichments, gadolinium pins and the water holes) are represented homogeneously. However, all control blades and water gaps which play important roles in the homogenization of a partially rodded node for the control rod cusping problem, are explicitly modeled as illustrated in the 8 X 8 mesh layout of Fig. A4.1, Appendix 4. The heterogeneous cross sections of each composition of the rodded and unrodded assemblies are given in Table A4.2, Appendix 4. With these heterogeneous cross sections, two-dimensional 24 X 24 mesh full plane (Fig. A4.2) calculations were carried out using QUANDRY to determine homogenized nodal cross sections and radial discontinuity factors for the nine nodes. The same 24 X 24 mesh calculations were run for five different planes, and the resultant nodal homogenization parameters are listed in Table A4.3, Appendix 4 for the 45 distinct nodes representing the core of the 3 X 3 X 10 TRD-BWR model. The radial discontinuity factors are spread over a wider range (0.46 ~ 1.71) than those of the CC3-PWR model (0.93 ~ 1.17). Homogenized cross sections for reflector nodes are those of the Vermont Yankee BWR and unity discontinuity factors were taken there.

5.3 Numerical Standards

The application of the Collector-Predictor methods for resolution of the control rod cusping problem requires that accurate standard solutions be provided. Because of the nature of the three-dimensional problem, spatial truncation error from spatial mesh discretization can be major source of inaccuracy. For time-dependent problem, temporal instability problem caused by inadequate choice of the time interval between time steps can be another source of error for the numerical solutions.

5.3.1 Spatial Convergence

The PDQ-7 finite-difference model is generally regarded as capable of providing quite accurate solutions to various light water reactor problems. However, the number of mesh points is restricted to a practical limit such that spatial truncation error is almost unavoidable. Thus, it is necessary to give reconsideration to the fact that PDQ-7 solutions may not be fully converged spatially.

5.3.1.1 Planar Calculations for Radial Homogenization

The spatial convergence problem of the PDQ-7 solutions for a rodded plane of the CC3-PWR model was investigated by solution of the same problem using three different mesh sizes, 1.4 cm, 0.7 cm, and 0.35 cm. A quadratically extrapolated solution was used as a reference. This was estimated as follows:

We define a solution value $A(h)$ as

$A(0.7)$ = PDQ-7 solution for mesh size $h = 0.7$ cm

$A(0.35)$ = PDQ-7 solution for mesh size $h = 0.35$ cm

$A(0.)$ = extrapolated PDQ-7 solution for $h = 0.0$

$A(h) = ah^2 + bh + c$

To determine $A(0.)$, we use two data points, $A(0.7)$ and $A(0.35)$, and impose at $h = 0$ an asymptotically converging condition,

$$\frac{dA(h)}{dh} \Big|_{h=0} = 0$$

Solving for the three unknowns, a , b and c then yields an asymptotically converging solution,

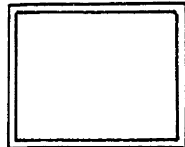
$$A(0.) = \frac{1}{3} [4A(0.35) - A(0.7)]$$

where the A 's may be either power densities or eigenvalues.

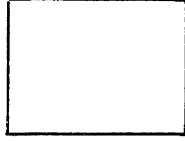
Figure 5.5 presents the PDQ-7 solutions for three mesh sizes along with the extrapolated PDQ-7 solution. Also it gives the corresponding QUANDRY solution with one mesh region per pin cell. As this figure shows, the agreement between the 1.4 cm, 0.7 cm and 0.35 cm PDQ-7 solutions for the unrodded nodes is fairly good. However, for the node in which control rods are present, the results show that the use of even the finer-mesh spacings 0.7 cm and 0.35 cm yields errors of 2.7% and 0.7% in nodal power density. The comparison demonstrates

(a) quarter assembly power density

0.7586	0.6168
0.7686	0.6456
0.7727	0.6589
0.7741	0.6633
0.7750	0.6667
1.0877	0.8417
1.0871	0.8466
1.0870	0.8485
1.0870	0.8491
1.0871	0.8495
1.2498	1.0124
1.2390	1.0070
1.2345	1.0043
1.2330	1.0034
1.2320	1.0027
1.0956	1.3373
1.0851	1.3210
1.0801	1.3141
1.0784	1.3118
1.0772	1.3103



rodded
node



unrodded
node

1.4cm mesh PDQ-7
0.7cm mesh PDQ-7
0.35cm mesh PDQ-7*
extrapolated PDQ-7**
1.4cm mesh QUANDRY

(b) eigenvalue

0.9564
0.9568
0.95703
0.95711
0.95712

* 55 sec computing time

** 21 sec computing time

Figure 5.5 Comparison of PDQ-7 and QUANDRY solutions for a two-dimensional, heterogeneous, rodded 2 X 4 nodal plane of the CC3-PWR.

that the QUANDRY solution with one mesh region per cell provides a far more accurate reference than the same mesh PDQ-7 solution. In fact the extrapolated PDQ-7 solution and the QUANDRY 1.4 cm mesh solution show remarkable agreement in nodal power density and eigenvalue. Even the use of four or sixteen mesh regions per cell for the PDQ-7 solutions do not achieve that accuracy. Note also that the QUANDRY solution with 1.4 cm mesh was obtained in a shorter computing time than the PDQ-7 solution with 0.35 cm mesh (21 sec vs. 55 sec). The main cause of the serious spatial convergence problem of PDQ-7 for the CC3-PWR model is the significant radial heterogeneity caused by the control rod cells and water holes. In QUANDRY, the analytic solution method and the quadratic transverse leakage approximation can resolve the radial heterogeneity problem with pin-sized mesh intervals. Accordingly, in the following sections, the numerical standard solutions for radial homogenization problems will be obtained from fine-mesh QUANDRY computations.

5.3.1.2 Unity Axial Discontinuity Factors

The two-dimensional fine-mesh calculations provide no systematic way of estimating discontinuity factors at nodal interfaces in axial direction, and it is standard to use unity discontinuity factors (UDF) at those locations. It seems prudent, however, to examine the validity of

this approximation.

Straightforward comparison of PDQ-7 and QUANDRY solutions are presented in references K-2 and F-5 for the CC3-PWR and TRD-BWR models. They show that the use of unity discontinuity factors in the axial direction is acceptable (k_{eff} predicted to 0.05% and nodal powers to within 3%). However, because the comparison of the QUANDRY solution with the PDQ-7 solution does not distinguish error caused by radial heterogeneity and spatial convergence from that caused by use of unity axial discontinuity factors, it is advisable to compare two QUANDRY solutions of different axial mesh intervals. To do this, the original 2 X 4 X 8 CC3-PWR mesh system was altered to have twenty-two axial finer-mesh intervals (2 X 4 X 22 system) shown in Fig. A 3.2 of Appendix 3. All the axial discontinuity factors are set to unity for both mesh systems. Results of the finer-mesh solution are edited and compared with those of the 2 X 4 X 8 problem. The comparison is presented in Table A3.3 of Appendix 3. The differences are negligibly small. The deviation in eigenvalue is 0.0012% and the maximum difference in nodal power is only 0.03%, and this occurs in the low-powered rodded node next to the top reflector. Because of this excellent agreement, unity axial discontinuity factors will be used for all axially homogeneous nodes, rodded or unrodded, and a

finer-mesh QUANDRY model will serve as reference solution for three-dimensional benchmark problems.

5.3.2 Temporal Stability

A finite-difference approximation to the temporal derivatives is used in solving time-dependent QUANDRY nodal equations. In Chapter 2, two approximations were introduced for time-dependent QUANDRY solutions. These are the Theta Method and the Frequency Transformation Method expressed in Eq. 2.22 and Eq. 2.23, respectively. For accurate description of delayed neutron behavior, the interval Δt_n between time steps (n) and (n+1) should be small enough not to cause temporal instability. Vota et al. [V-1] suggested a stability condition

$$\lambda_d \cdot \Delta t_n \leq 0.1$$

for all decay constants, λ_d , of delayed neutron precursor of group d. Table A 5.1 of Appendix 5 gives typical delayed neutron data and other input data for transient problems [L-2]. Since the typical range of λ_d for six delayed neutron groups in U²³⁵-fueled LWR is 0.013 - 3.9 sec⁻¹, the time interval in kinetic problem with six delayed neutron groups must be less than 25 msec. In Appendix 5, the acceptability of this limit for prompt neutron behavior will be verified through numerical test. This limit is then imposed in determining numerical standards and testing various methods for resolution of the control

rod cusping problem, and the data in Table A 5.1 will be used in all transient calculations.

5.4 Application to Steady-State Problem

Although the control rod cusping problem is of greatest importance for time-dependent power excursions during which a control rod is being withdrawn, it also causes difficulties in steady-state calculation. During the course of a reactor criticality search, control rod clusters may assume accurate criticality positions that lead to partially rodded nodes, and power shape predictions are desired for this situation. Operational constraints on local power density and its rate of change to insure fuel integrity are of concern for reactor startup procedures. Again accurate power distributions for situations involving partially rodded nodes (PRN) are needed.

This section deals with steady-state problems involving partially rodded nodes. The partially rodded node problems were solved by Method 1, and the criticality eigenvalues and nodal power distributions were compared with finer-mesh QUANDRY reference solutions. The CISE-BWR, TRD-BWR and CC3-PWR models without any feedback effect are examined.

5.4.1 The CISE-BWR Problem

The system which is being analyzed is the simple three-dimensional BWR problem shown in Fig. 5.3. The

diagonally symmetric system is characterized by a cruciform control blade surrounded by four fuel assemblies containing no void, and a part of a control blade at a corner. This problem was devised to examine the accuracy of volume-flux-weighted radial discontinuity factors (VFWRDF) for a PRN in a BWR and to apply Method 1 to a problem with two control blades positioned at different elevations.

For an initial solution, a 3 X 3 X 4 system was created by extending the axial dimension of the CISE-BWR so that there are four axial meshes of 20 cm widths. The lower two planes are completely rodded. First, this 3 X 3 X 4 problem was solved to provide necessary information needed at the Collector stage. The axial flux shape was then edited out for various magnitudes of h_c (the distance the rod is removed from a fully rodded node); Fig. 5.3b. Two cases were tested; one is almost fully rodded ($h_c = 2$ cm), the other halfway rodded ($h_c = 10$ cm). For each case, two different sets of radial discontinuity factors (VFWRDF and UDF) were used for the partially rodded node. Results are shown in Table 5.1. The VFWRDF approximation is clearly superior to the use of unity radial discontinuity factors for a PRN. For VFWRDF, the error in k_{eff} is less than 0.006%; the maximum error in nodal power is 0.25% and occurs at one of the lower nodes in the rodded assemblies. Moreover, there are

Table 5.1

Test Results for Method 1 and the Volume-Flux-Weighted Radial Discontinuity Factors (VFWRDF) for the CISE-BWR.

(a) using VFWRDF approximations for PRN's

comparison		$h_c = 2 \text{ cm}$	$h_c = 10 \text{ cm}$
k_{eff}	reference 3x3x4 calc.	0.992948	1.008414
	Method 1	0.992944	1.008352
	error	-0.0004%	-0.0061%
max. error of nodal power density	top node	-0.12%	-0.16%
	PRN	0.10%	-0.15%
	bottom node	0.14%	0.25%

(b) using unity radial discontinuity factors for PRN's only

comparison		$h_c = 2 \text{ cm}$	$h_c = 10 \text{ cm}$
k_{eff}	Method 1	0.991587	1.007908
	error	-0.14%	-0.050%
max. error of nodal power density	top node	1.1%	0.38%
	PRN	8.2%	6.4%
	bottom node	-0.85%	0.67%

no noticeable errors in power for nodes radially adjacent to the PRN's.

On the other hand, the use of unity radial discontinuity factors yields very poor solutions. The maximum errors in k_{eff} and nodal power exceed 0.1% and 8%, respectively. The error in power of nodes radially surrounding the PRN is also about 8%. These results establish that the VFWRDF approximation is quite acceptable even for BWR problems where the radial heterogeneity is more pronounced than for PWR problems (see Section 4.3.3 for a PWR test result).

The same CISE-BWR model was altered to have the configuration shown in Table 5.2b. In the altered system, two control blades were partially inserted to different elevations. The homogenization parameters of the PRN's were determined by making use of information from the solution of the aforementioned 3 X 3 X 4 extended system. Results are compared with the solution of a 3 X 3 X 5 finer-mesh layout shown in Table 5.2a. They are excellent (<0.005% error in k_{eff} and ~0.2% in nodal power).

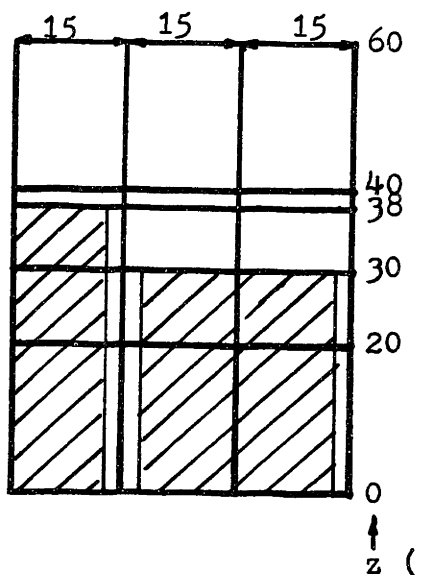
5.4.2 The TRD-BWR Problem

Static tests were performed for two TRD-BWR situations, the particular cases simulated being chosen because of the importance of control rod operational patterns during the startup procedure.

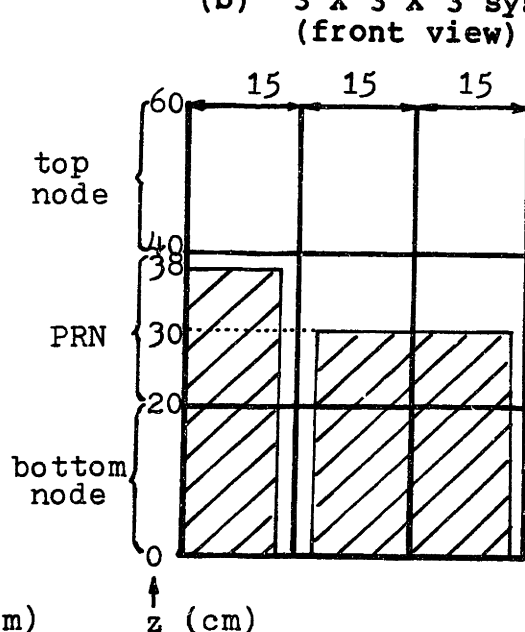
Table 5.2 Comparison of k_{eff} and Nodal Powers of a CISE-BWR Static Problem with Non-uniform Control Blade Levels.

	k_{eff}	error in nodal power density		
		top node	PRN	bottom node
exact 3x3x5(a)	1.004928	1.2128	0.9221	0.7930
Method 1 3x3x3(b)	1.004885	1.2110	0.9206	0.7947
error	-0.0043%	-0.15%	-0.16%	0.21%

(a) 3 X 3 X 5 system
(front view)



(b) 3 X 3 X 3 system
(front view)



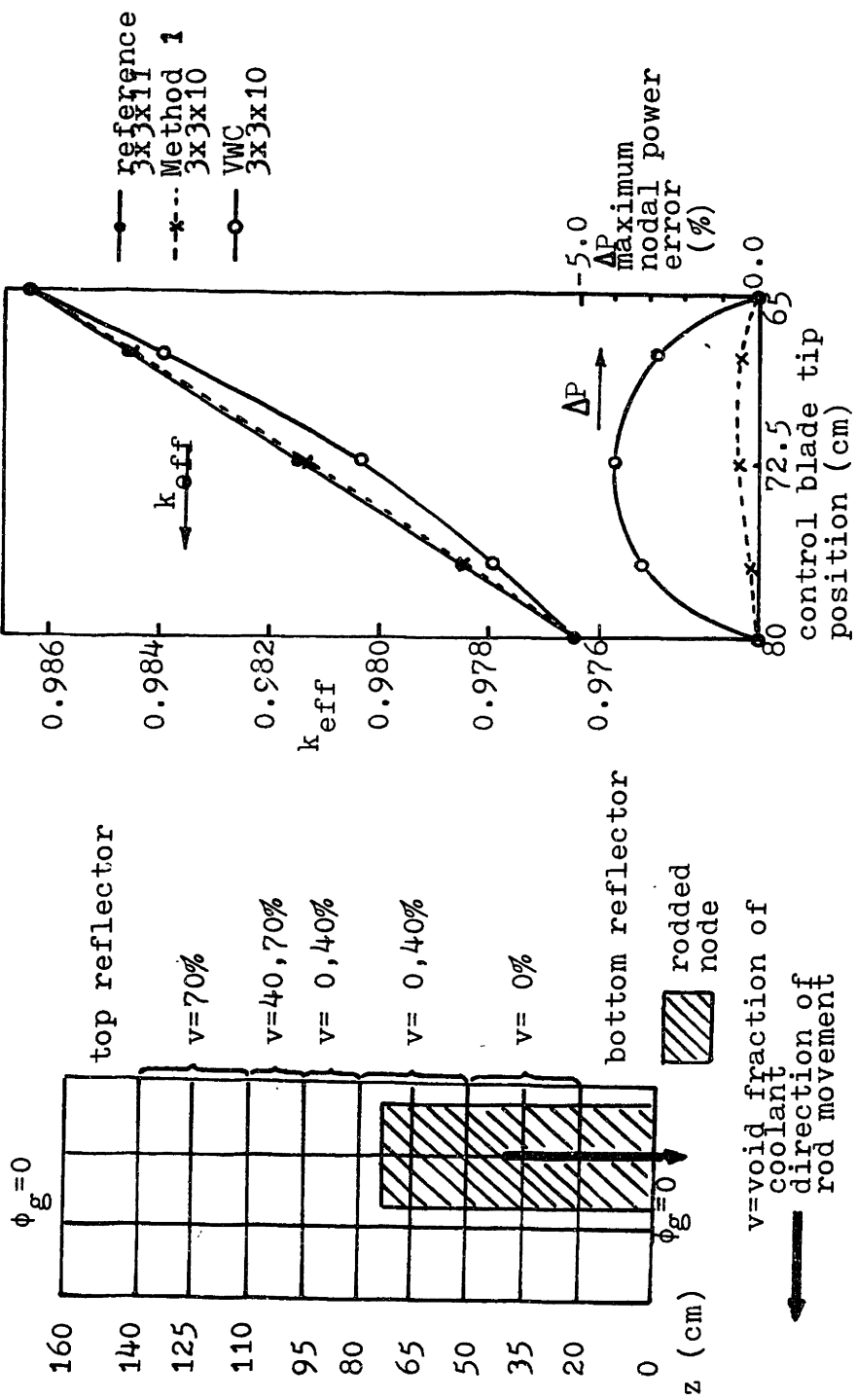
5.4.2.1 A Partially-Rodded Interior Node

The first case examined involved a control rod pattern in the central region of a core as shown in Fig. 5.6. The control rod was withdrawn across an internal node from $z = 80$ cm to $z = 65$ cm. Figure 5.7 and Table 5.3 show the results for three elevations of the control rod. Method 1 predicts k_{eff} within 0.01% error, while VWC method yields maximum error of about 0.1% in k_{eff} . Accuracy of nodal power predicted by Method 1 is also improved by about a factor of 10.

5.4.2.2 A Partially Rodded Node With Shallow Rods

Because of axial void distribution, the axial power distribution in a BWR tends to be skewed toward the lower part of the core. The direct way of reducing the power peak near the bottom water reflector is to use shallow rods. However, if the power distribution is flattened too much by use of the shallow rods, their complete withdrawal can cause a power overshoot in the lower part of core. Therefore, it is important to predict accurate rod worth and power distribution when shallow control rods move through a node next to the bottom reflector in a BWR.

For the purpose of shallow rod simulation in the TRD-BWR model, the original TRD-BWR was slightly modified as specified in Fig. 5.8. With shallow rods, the reactor power near the rods is assumed to be significant.



152

Figure 5.7 Comparisons of k_{eff} and ΔP for the TRD-BWR.

Table 5.3

**Comparison of k_{eff} and Nodal Power Errors
for a TRD-BWR Static Problem with an Internal
PRN.**

comparison	methods	control tip positions		
		77 cm	72.5 cm	68 cm
k_{eff} (% error in parenthe- sis)	reference $3 \times 3 \times 11$	0.97855	0.98149	0.98437
	Method 1 $3 \times 3 \times 10$	0.97853 (-0.0023%)	0.98140 (-0.0093%)	0.98428 (-0.010%)
	VWC $3 \times 3 \times 10$	0.97802 (-0.054%)	0.98053 (-0.097%)	0.98368 (-0.071%)
max. nodal power error	Method 1 $3 \times 3 \times 10$	-0.18%	-0.53%	-0.51%
	VWC $3 \times 3 \times 10$	-3.2%	-4.1%	-3.0%

Consequently, the void fraction was increased as indicated in Fig. 5.8. The tip of the control blade was simulated as being withdrawn from the upper face of the bottom fueled node (i.e., $z = 35$ cm). Method 1 was applied to the system with the tip at $z = 35$ cm. Table 5.4 displays the numerical data, and they are plotted in Fig. 5.9. The results demonstrate that the accuracy of Method 1 is improved by about a factor of 10 in k_{eff} and power density over the conventional VWC method. In contrast to what happens with an internal PRN, Method 1 applied to the shallow rod slightly overpredicts the power density. The difference is due to the effect of the thermal flux peak in the bottom reflector. The effect of the reflector cannot be well reflected by Method 1 when the Collector procedure has been performed with the tip of the control blade far from the core-reflector interface.

Nevertheless, these static benchmark problems demonstrate that Method 1 is superior to VWC method and is quite acceptable when applied to the control rod cusping problem for steady-state BWR calculations.

5.4.3 The CC3-PWR Problem

A similar test was performed to test Method 1 for the static CC3-PWR problem described in Section 5.2.1. Calculations were done for the tip of the control rod located at 13 axial positions ranging from the 80 cm

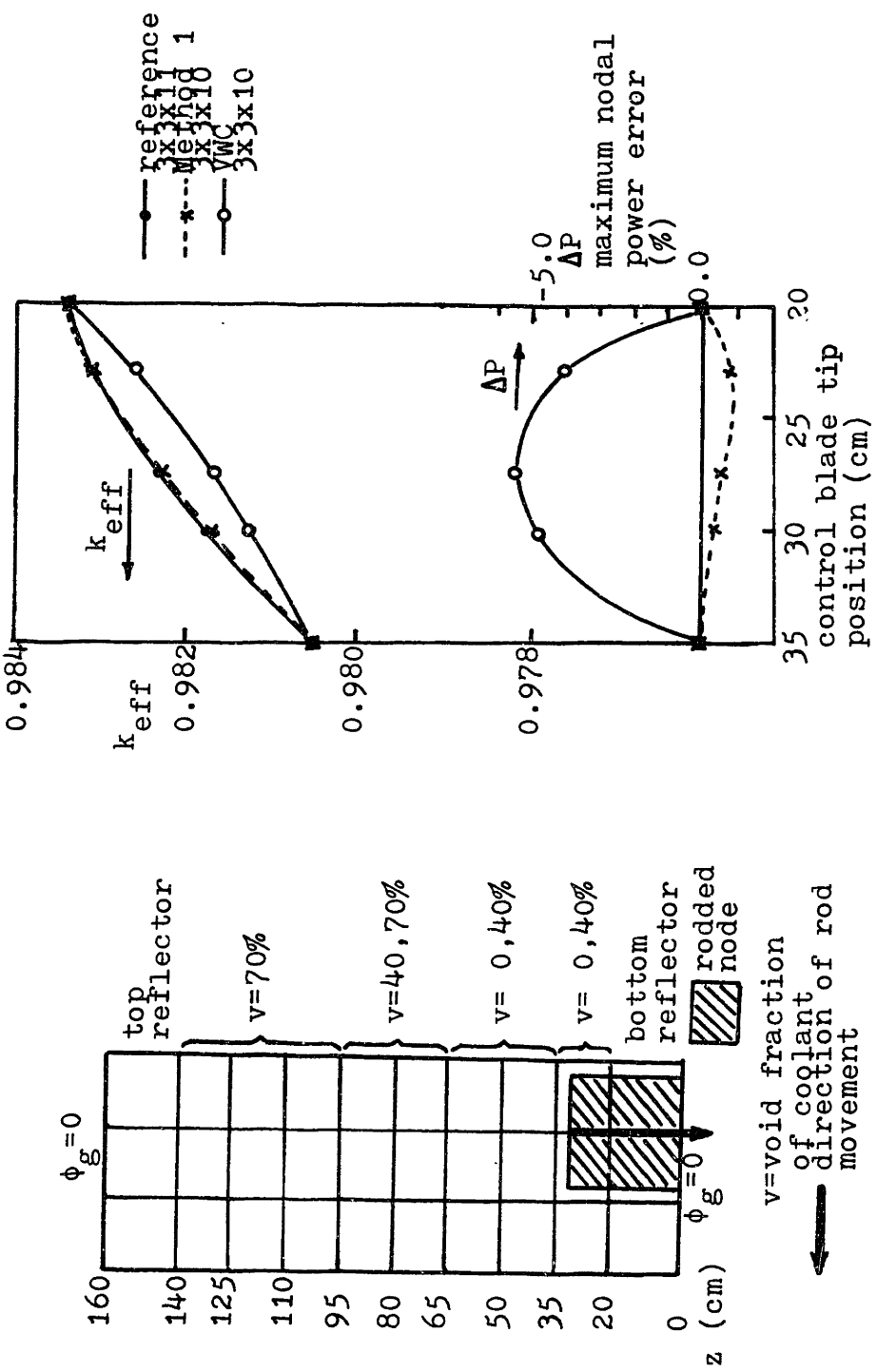


Figure 5.8 An axial configuration of the TRD-BWR with a shallow PRN.

Figure 5.9 Comparisons of k_{eff} and errors in nodal power for the TRD-BWR.

Table 5.4 Comparisons of k_{eff} and Nodal Power Error for a TRD-BWR Static Problem with a PRN Next to the Bottom Reflector.

comparison	methods	control blade tip position	
		27.5 cm	23 cm
k_{eff} (% error in parenthe- sis)	reference $3 \times 3 \times 11$	0.982364	0.983052
	Method 1 $3 \times 3 \times 10$	0.982360 (-0.0004%)	0.983085 (0.0034%)
	VWC $3 \times 3 \times 10$	0.981672 (-0.070%)	0.982609 (-0.045%)
max. nodal power error	Method 1 $3 \times 3 \times 10$	0.55%	0.91%
	VWC $3 \times 3 \times 10$	-5.5%	-4.0%

to the 140 cm (Fig. 5.1). Three auxiliary Collector stage calculations were carried out when the tip of the rod reached the axial nodal interfaces at $z = 80$, 100 and 120 cm. Three-dimensional QUANDRY problems making use of the homogenization parameters given in Table A3.2b of Appendix 3, and with an extra axial plane inserted at the location of the tip of the control rod in the PRN, were taken as reference solutions.

Eigenvalues and power density for the PRN as computed by the VWC method and by Method 1 were compared with these reference solutions. Results are displayed in Table 5.5 and Fig. 5.10. For Method 1, errors in k_{eff} remain below 0.01% in most cases, and those in power density are less than 1% except for one case when the PRN is next to the top water reflector. There the error is -2.1%. Errors arising from use of the volume-weighted constants and unity axial discontinuity factors are much greater. It is interesting to notice that as the tip of the control rod moves toward the bottom of the core, the error pattern in both the VWC method and Method 1 is similar. Peak errors in a node increase steadily. However, the peak error near the reflector does not have serious consequences since the maximum linear heat rate and minimum DNBR (departure from nucleate boiling ratio) do not occur in this region of low power generation.

Table 5.5 Error in k_{eff} and Maximum Nodal Power Error (ΔP) for the CC3-PWR Model (Static Problem).

control rod tip position (cm)	error in k_{eff} (%)		max. error in nodal power (%)	
	VWC 2x4x8	Method 1 2x4x8	VWC 2x4x8	Method 1 2x4x8
85	-0.066	-0.0058	-2.6	-0.23
90	-0.097	-0.011	-4.1	-0.68
98	-0.039	-0.0071	-2.2	-0.50
100	0.0	0.0	0.0	0.0
105	-0.058	-0.0055	-3.3	-0.29
110	-0.057	-0.0099	-5.8	-0.94
118	-0.032	-0.0046	-2.7	-0.57
120	0.0	0.0	0.0	0.0
125	-0.034	-0.0049	-5.7	-0.84
130	-0.046	-0.0082	-8.7	-2.1
138	-0.017	-0.0027	-3.4	-0.67

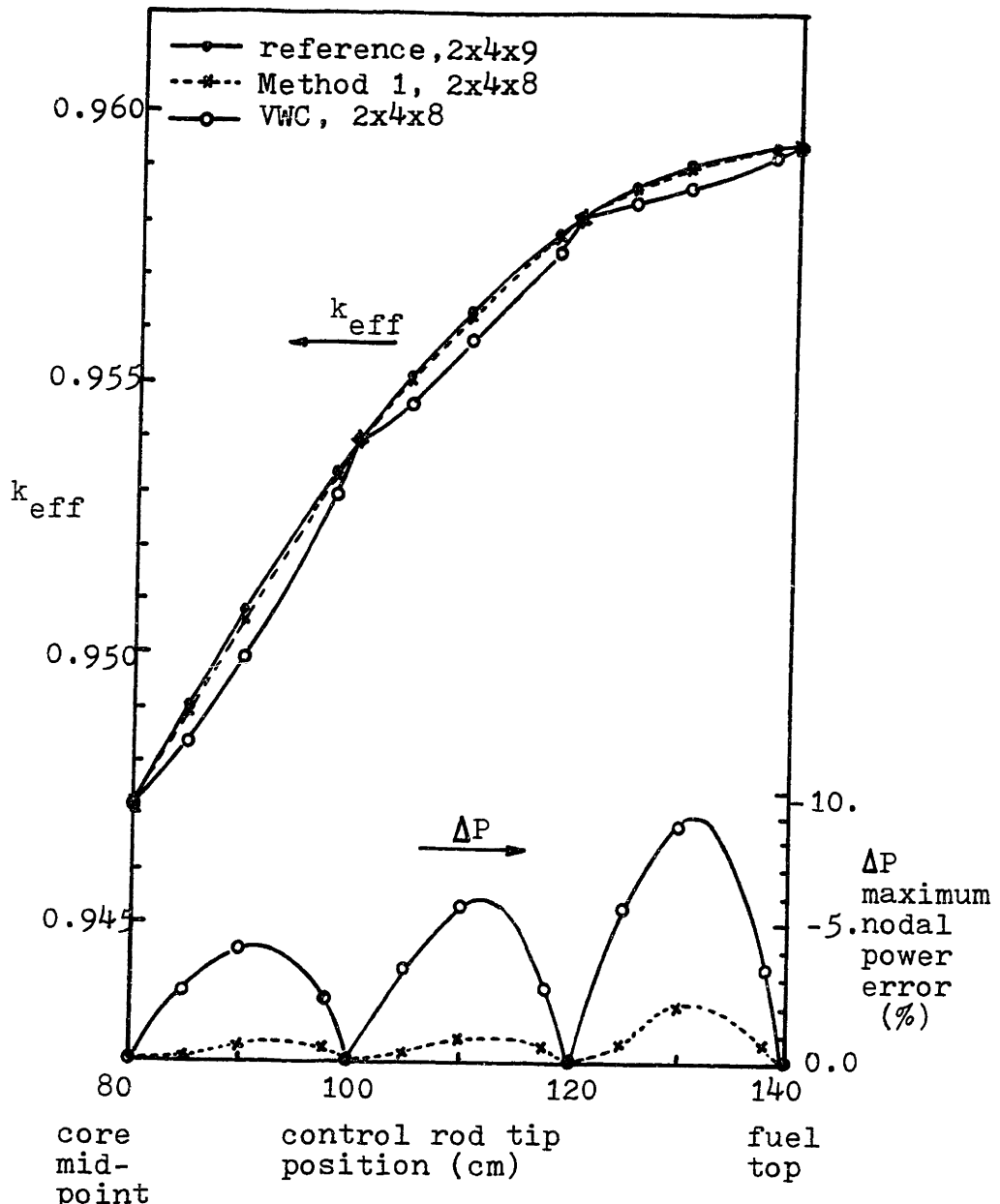


Figure 5.10 Comparisons of k_{eff} and nodal power of the CC3-PWR.

These results, obtained from a series of test calculations, demonstrate that the Collector-Predictor method (Method 1) clearly resolves the control rod cusping problem for various static problems and improves the accuracy by a factor of 5 to 10 over the conventional VWC scheme.

5.5 Time-Dependent Problems

The Collector-Predictor methods are tested in this section for transient TRD-BWR and CC3-PWR benchmark problems. Homogenized cross sections and discontinuity factors for homogeneous nodes have been determined in Section 5.2. Finer-mesh QUANDRY solutions (see Section 5.3) serve as a numerical reference solutions, and the conventional volume-weighted cross section and quadratic axial flux approximation methods along with the Collector-Predictor method (Method 1 and Method 2) are evaluated by reference to those solutions. As mentioned in Section 4.4, Method 2 can be applied with four options depending on the way the transverse leakage rates are estimated for the two subnodes in a partially rodded node:

Method 2F --- flat transverse leakage over a PRN.

Method 2M --- median of transverse leakages of a PRN and an axially neighboring node.

Method 2Q --- quadratic transverse leakage shape over a PRN.

Method 2J --- net surface current in axial direction at the tip of the control rod is employed.

These different approximations will be compared for a CC3-PWR transient case.

Three transient cases associated with the control rod cusping problem were examined: a control rod drop event in the TRD-BWR, a rod insertion in the CC3-PWR and a rod ejection in the CC3-PWR. Because of the similar model configurations and use of common conditions (e.g., boundary conditions, delayed neutron data and no feedback effect), only the results of the third problem, the CC3-PWR rod ejection, are extensively analyzed and evaluated.

Choosing proper time step size is an important task in transient calculations. Justifications of taking the time step interval limit discussed in Section 5.3.2 through numerical solutions for several values of interval size (1.25, 2.5, 5.0 and 10 msec) is presented in Appendix 5.

5.5.1 The TRD-BWR Rod Drop

The first application of the Collector-Predictor method to transient problems is a three-dimensional rod drop simulation for the TRD-BWR model. An important

design-basis accident for boiling water reactor is the control rod drop accident.

The magnitude of the effect depends on reactor conditions. Moderator feedback is particularly important when there are voids in the core or when the core is near saturation conditions. Other factors are power level, flow rate, rod drop speed, rod worth, and delayed neutron fraction. It is known that accident consequences are not sensitive to the delayed neutron fraction and rod drop speed, but sensitive to inlet subcooling and accident rod worth [C-4]. However, our interest concerns only three-dimensional neutronic effects caused by a PRN. Accordingly, feedback effects will not be considered in this thesis.

A typical BWR rod drop speed of 150 cm/sec [C-4] was used for the TRD-BWR calculation. Data for delayed neutron are given in Table A5.1 of Appendix 5.

The reactor (Fig. 5.4) was assumed to be initially critical, and rod withdrawal was accomplished in ten time steps for 100 msec (i.e., 1.5 cm withdrawal per 10 msec time interval) through a node from $z = 65$ cm to $z = 50$ cm. The transient power levels from five different solution methods are summarized in Table 5.6, and are plotted in Fig. 5.11. During the transient, total power level increased rapidly from 100 watts to 1695.5 watts.

Table 5.6 Comparison of Total Power Changes during a TRD-BWR Rod Drop Event.

rod position Z (cm)	time (ms)	reference 3x3x19 calculation (W)	error in total power (%)				
			VWC 3x3x10	quadratic axial flux 3x3x10	Method 1 3x3x10	Method 2W 3x3x10	Method 2Q 3x3x10
65.0	0.	100.0	0.0	0.0	0.0	0.0	0.0
63.5	10	107.01	-1.32	0.26	0.81	0.81	0.81
62.0	20	121.29	-5.05	-1.35	0.64	0.73	0.88
60.5	30	142.26	-9.38	-3.56	0.22	0.51	0.84
59.0	40	172.10	-16.9	-6.18	-0.39	0.31	0.84
57.5	50	215.51	-18.8	-9.03	-1.17	0.04	0.78
56.0	60	281.23	-23.5	-11.9	-2.17	-0.30	0.69
54.5	70	387.36	-27.9	-14.5	-3.37	-0.70	0.53
53.0	80	571.36	-31.2	-16.4	-4.49	-0.97	0.44
51.5	90	924.74	-32.5	-17.0	-5.32	-1.16	0.35
50.0	100	1695.5	-29.0	-14.7	-5.0	-1.03	0.42
computing time (sec)		26.8	12.3	12.5	12.0	12.4	12.4

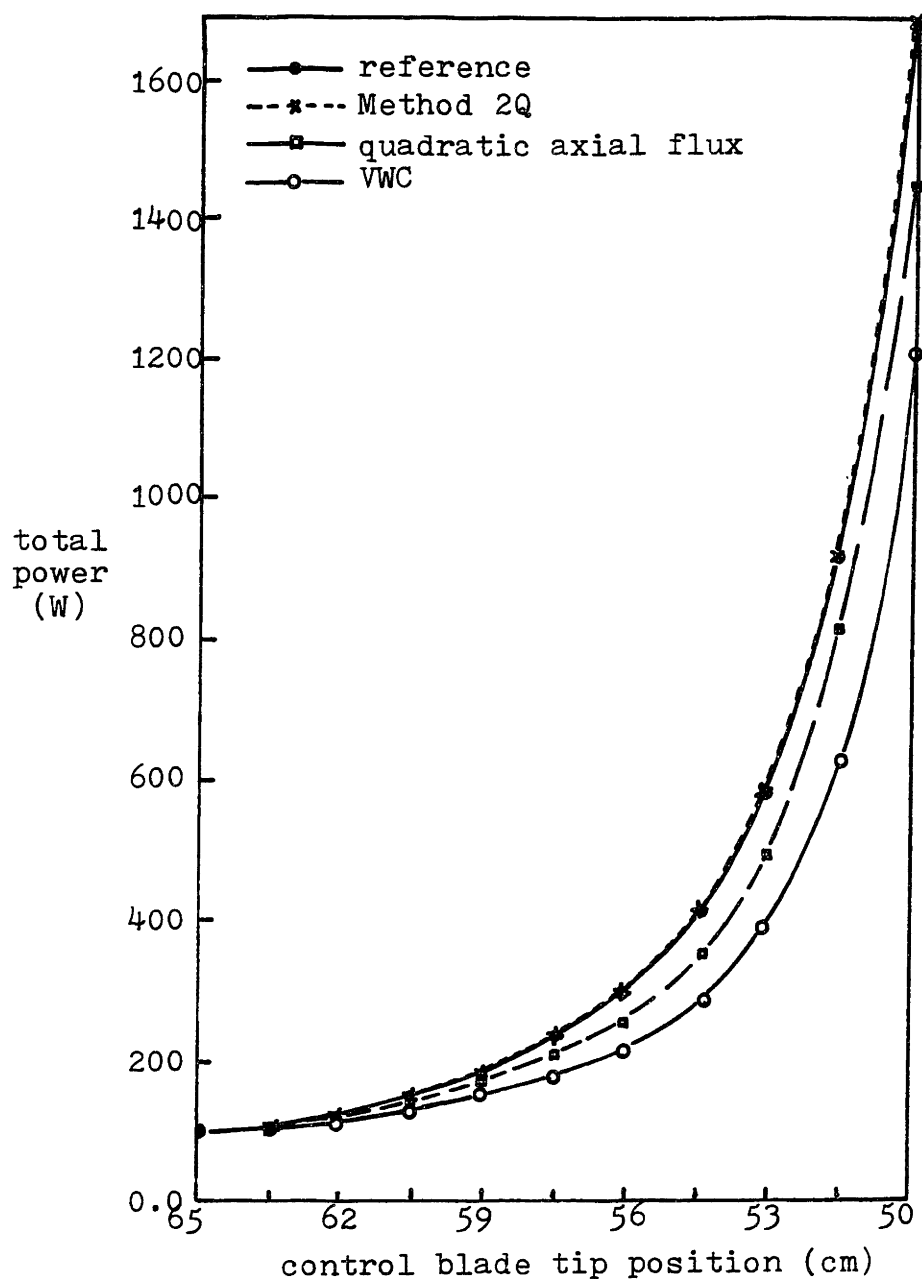


Figure 5.11 Comparison of transient power predictions for the TRD-BWR.

Comparison with finer-mesh solution shows the inadequacy of the VWC scheme and quadratic axial flux approximation method. On the other hand, remarkable accuracy was achieved by the Collector-Predictor method - particularly Method 2. The error throughout the transient has been reduced by a factor of ~20 for Method 2Q, and remains below 1%.

5.5.2 The CC3-PWR Rod Insertion

In this case, a reactor scram is modeled for the CC3-PWR illustrated in Fig. 5.1.

Initially the rod was positioned at $z = 100$ cm, and was then inserted to $z = 80$ cm position during the scram. Scram rod speed was 200 cm/sec, and the control rod was inserted for 0.1 sec after scram was activated. The insertion was completed in ten time steps at a rate of 2 cm/10 msec. Method 2 was tested along with the VWC and quadratic flux approximation methods. Error of total power and maximum error of nodal power at each time step are summarized in Table 5.7. During scram, the power level lowered to a half of the initial power. The quadratic axial flux approximation improves marginally, while Method 2 leads to negligible error (<1%). The computing time of Method 2 is marginally greater than that of VWC method (8.8 sec vs. 9.5 sec). Actually two kinds of Method 2 were tested, and in this rod insertion problem, Method 2M is more accurate than Method 2J (methods

Table 5.7 Comparisons of Power Levels for the CC3-PWR
during Rod Insertion from 100 to 80 cm.

(a) total reactor power

rod tip position z (cm)	reference 2x4x17 calculation (W)	error in total reactor power (%), 2x4x8			
		VWC	quadratic axial flux	Method 2M	Method 2J
100	100.	0.0	0.0	0.0	0.0
98	93.48	-3.42	-1.97	0.18	0.18
96	85.73	-6.10	-3.71	0.28	0.73
94	78.88	-8.03	-5.20	0.37	0.93
92	72.78	-9.00	-6.04	0.46	1.07
90	67.32	-9.02	-6.24	0.46	1.07
88	62.42	-8.31	-5.87	0.43	1.00
86	58.05	-7.06	-5.04	0.33	0.83
84	54.11	-5.39	-3.83	0.21	0.63
82	50.56	-3.39	-2.45	0.18	0.44
80	47.35	-1.17	-0.96	0.16	0.21
computing time(sec)	19.9	8.8	9.2	9.5	9.6

Table 5.7 (continued)
(b) nodal power density of the PRN

rod tip position Z (cm)	reference 2x4x17 calculation (W)	error in nodal power density (%), 2x4x8			
		VMC	quadratic axial flux	Method 2M	Method 2J
100	1.3111	0.20 *	0.20 *	0.20 *	0.20 *
98	1.1922	-4.98	-2.87	0.39	0.39
96	1.0546	-8.42	-4.99	0.29	1.09
94	0.9333	-10.7	-6.58	0.50	1.41
92	0.8252	-11.6	-7.17	0.65	1.66
90	0.7294	-11.1	-6.86	0.74	1.76
88	0.6448	-9.65	-5.71	0.75	1.74
86	0.5708	-7.36	-3.96	0.64	1.53
84	0.5063	-4.43	-1.76	0.47	1.22
82	0.4510	-1.22	+0.40	0.33	0.79
80	0.4062	+1.52	+1.75	0.05	0.10

*due to spatial convergence problem, i.e., 8 and
 17 axial node systems.

2M and 2J for Method 2 were defined in Section 4.4). For all methods, the maximum error occurs when the tip of the control rod passes through the middle of a node.

5.5.3 The CC3-PWR Rod Ejection

The final test of the Collector-Predictor method is to simulate a rod ejection accident in the CC3-PWR model. Initially, the tip of the control rod was located at $z = 100$ cm in the critical CC3-PWR (Fig. 5.1). The rod was then ejected from the node in plane number 6 ($z = 100$ cm to $z = 120$ cm) at a speed of 200 cm/sec for 0.1 sec. During the event, the reactor power rose rapidly from 100 w to 283.8 w. The problem was solved by six different methods. Results are given in Tables 5.8 and 5.9 and illustrated in Fig. 5.12 to 5.14.

First, prediction of the total reactor power transient are compared. The VWC method has a 19.2% maximum error achieved when the control rod has traveled through about two-thirds of the PRN. The quadratic axial flux approximation does not show any significant improvement, while Method 1 reduces the error to less than 5%. Use of the various Method 2 schemes clearly improves the accuracy of the solution, and does not show any cusping in power versus rod position (see Fig. 5.12). As anticipated by the discussion in Section 4.4, Method 2J results in a more accurate prediction than Method 2M or Method 2Q. The

Table 5.8 Comparison of Total Reactor Power for a CC3-PWR Transient with a Control Rod Withdrawn from $z = 100$ cm to 120 cm.

(a) conventional methods and Method 1

rod tip position Z (cm)	reference 2x4x17 calculation (W)	error in total power (%)		
		VWC 2x4x8	quadratic axial flux 2x4x8	Method 1 2x4x8
100	100.	0.0	0.0	0.0
102	106.63	-2.7	-1.6	0.02
104	117.05	-7.0	-4.6	-1.1
106	128.79	-10.6	-7.0	-1.8
108	142.45	-13.7	-9.2	-2.6
110	158.15	-16.3	-11.1	-3.3
112	176.54	-18.2	-12.6	-4.0
114	197.96	-19.2	-13.3	-4.7
116	222.56	-18.8	-13.2	-5.1
118	250.94	-16.4	-11.7	-4.9
120	283.81	-10.9	-8.6	-4.0
computing time(sec)	21.9	7.8	8.3	8.2

Table 5.8 (continued)

(b) Method 2

rod tip position Z (cm)	reference 2x4x17 (W)	error in total power (%)		
		Method 2M 2x4x8	Method 2Q 2x4x8	Method 2J 2x4x8
100	100.	0.0	0.0	0.0
102	106.63	0.02	0.02	0.02
104	117.05	-0.42	-0.61	-0.05
106	128.79	-0.49	-0.63	0.20
108	142.45	-0.58	-0.62	0.32
110	158.15	-0.90	-0.68	0.41
112	176.54	-1.16	-0.03	0.22
114	197.96	-1.51	-0.51	-0.34
116	222.56	-1.92	-0.92	-0.88
118	250.94	-2.30	-1.53	-1.61
120	283.81	-2.70	-2.32	-2.33
computing time(sec)	21.9	8.5	8.7	8.7

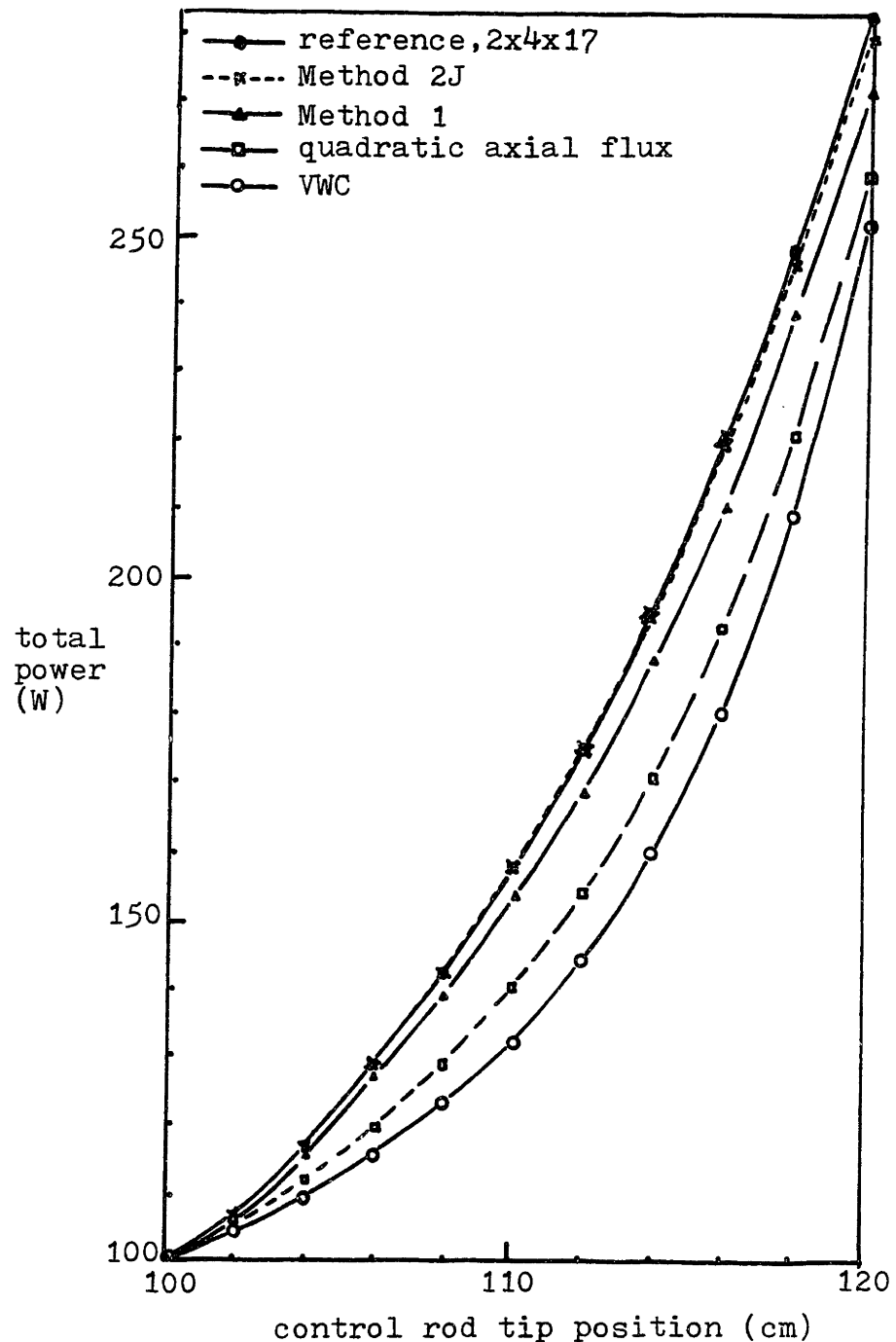


Figure 5.12 Total reactor power during a CC3-PWR transient.

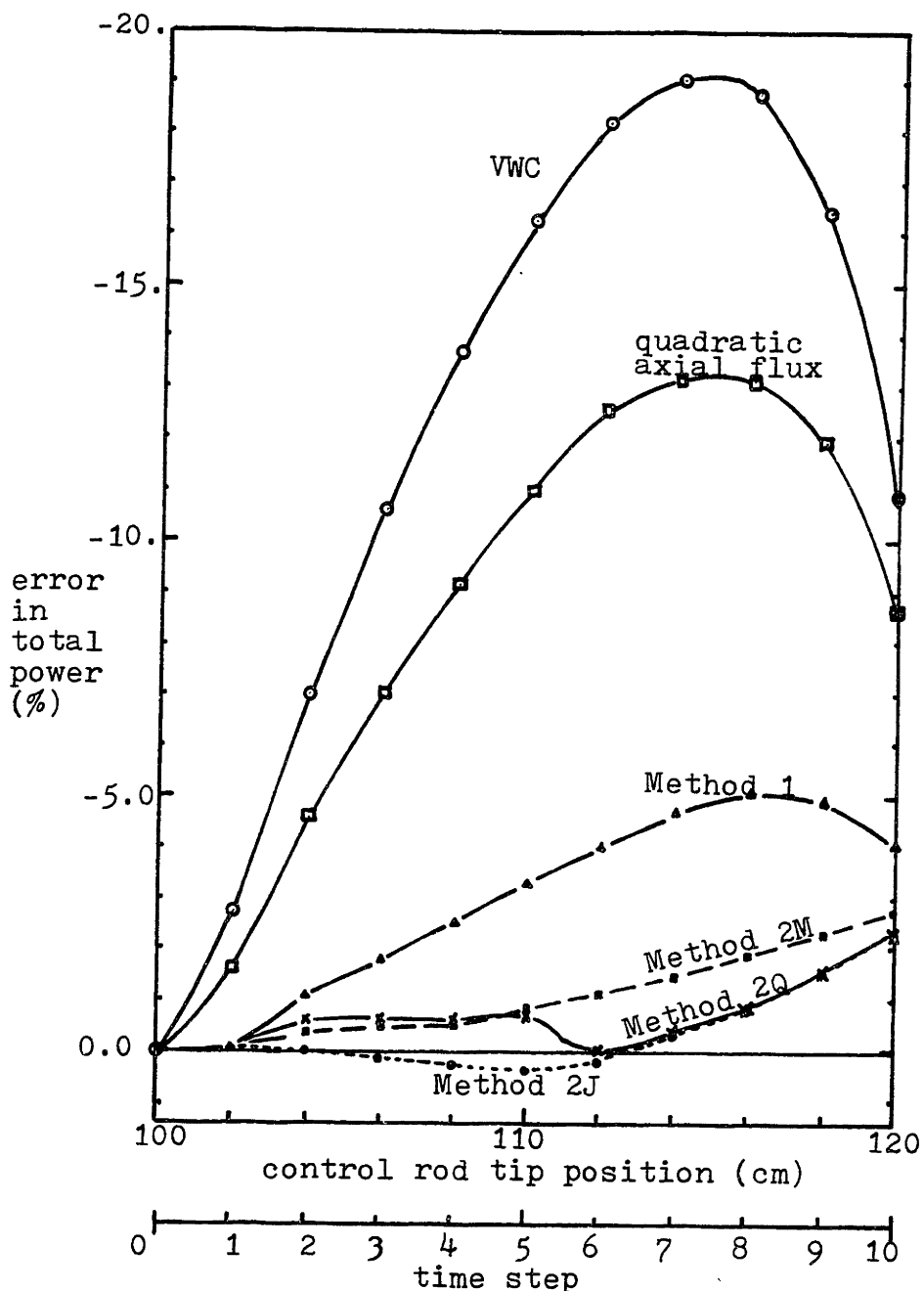


Figure 5.13 Errors in total power predictions during a CC3-PWR transient.

error in total power remains below 0.5% for Method 2J except for the last two time steps. Rapid increases in error are observed for the last few time steps for Method 2Q and Method 2J. These will be discussed below.

The accuracy of the conventional methods is worse for predicting local nodal power than it is for predicting total power level. As summarized in Table 5.9 and Fig. 5.14, the maximum error in nodal power density from VWC scheme is greater than that in total power (25.5% vs. 19.2%). Note that the maximum errors in both total and nodal power densities occur at the same time step for the conventional methods. Method 1 shows a similar error distribution. However, utilizing Method 2 achieves the same accuracy for nodal power density (<0.8% for Method 2J) as for the prediction of total power. This result clearly demonstrates that the use of Method 2 (particularly Method 2J) can resolve the control rod cusping problem in a PWR at a marginal increase in computing time (7.8 sec and 8.7 sec).

In Fig. 5.13, it can be seen that there are sudden rises in the error curves for Method 2Q and Method 2J, which are considered to be the most accurate solutions. Deviations in these two methods fluctuate, but remain within a certain error bound ($\pm 1\%$) until they start to increase at time step 9 ($z = 118$ cm). In order to

Table 5.9 Comparison of Nodal Power Density of the PRN for a CC3-PWR Transient with Control Rod Withdrawn from 100 cm to 120 cm.

(a) conventional methods and Method 1

rod tip position Z (cm)	reference 2x4x17 (normalized)	error in nodal power density (%)		
		VWC 2x4x8	quadratic axial flux 2x4x8	Method 1 2x4x8
100	0.6385	-0.39*	-0.39*	-0.39*
102	0.7150	-4.2	-1.8	-0.31
104	0.8322	-10.2	-5.9	-1.8
106	0.9694	-15.1	-9.2	-2.6
108	1.1336	-19.3	-12.4	-3.6
110	1.3265	-22.4	-14.9	-4.4
112	1.5558	-24.6	-16.9	-5.3
114	1.8260	-25.5	-17.8	-6.0
116	2.1391	-24.5	-17.6	-6.2
118	2.5004	-21.1	-15.8	-5.6
120	2.9089	-13.9	-11.7	-4.1

* due to spatial convergence error.

Table 5.9 . . . (continued)

(b) Method 2

rod tip position Z (cm)	reference 2x4x17 (normalized)	error in nodal power density (%)		
		Method 2M 2x4x8	Method 2Q 2x4x8	Method 2J 2x4x8
100	0.6385	-0.39*	-0.39*	-0.39*
102	0.7150	-0.31	-0.31	-0.31
104	0.8322	-0.50	-1.09	-0.26
106	0.9694	-0.41	-0.94	+0.25
108	1.1336	-0.30	-0.74	+0.55
110	1.3265	-1.23	-0.72	+0.78
112	1.5558	-1.21	+0.76	+0.60
114	1.8260	-1.56	-0.18	-0.05
116	2.1391	-2.00	-0.65	-0.73
118	2.5004	-2.42	-1.44	-1.58
120	2.9089	-2.76	-2.38	-2.40

* due to spatial convergence error.

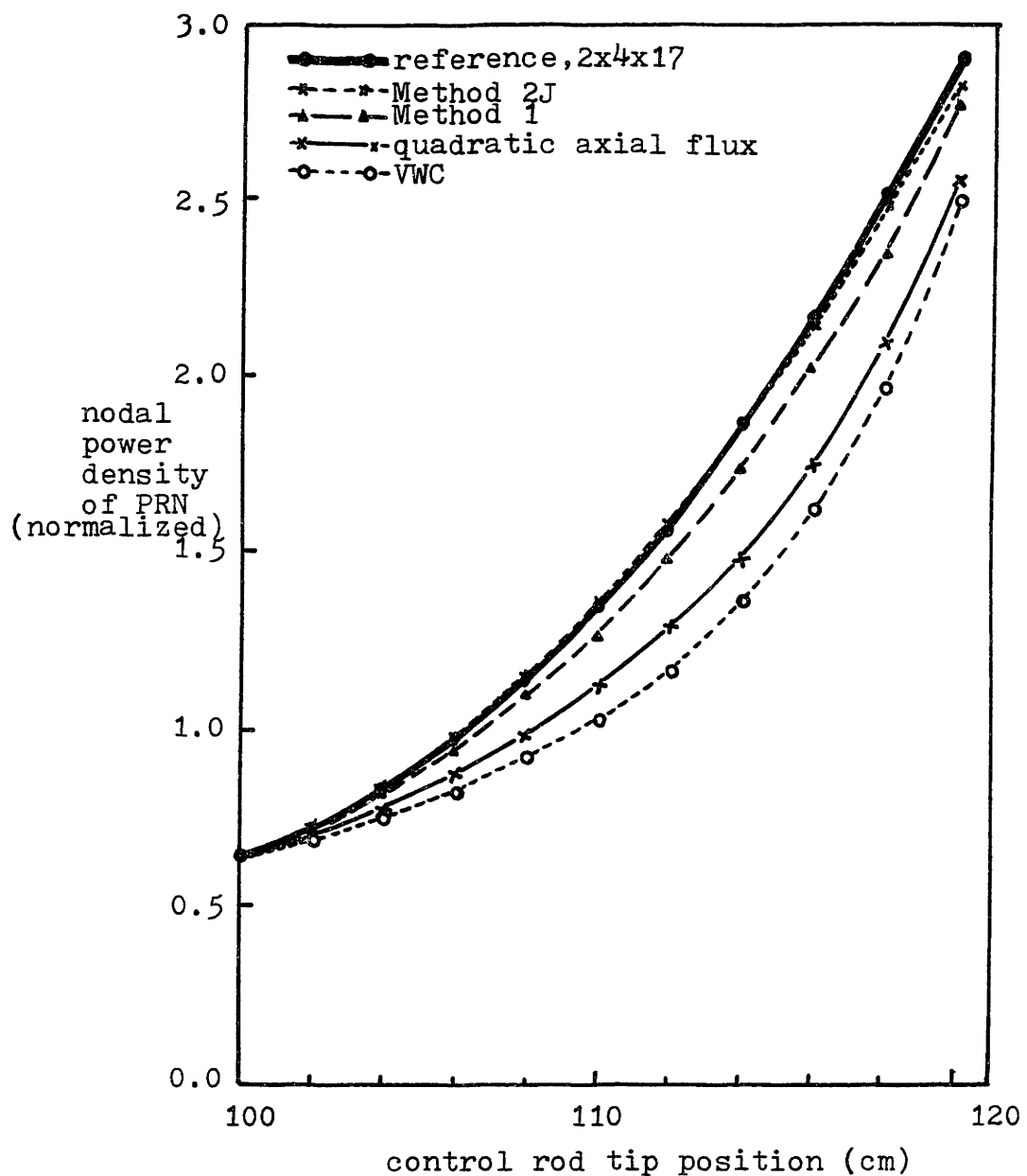


Figure 5.14 Nodal power densities of the PRN during a CC3-PWR transient.

investigate these sudden increases in error, another finer-mesh reference solution was compared with the original reference solution (the 2 X 4 X 17 mesh calculation). In addition to the ten fine meshes within the PRN ($z = 80 \sim 100$ cm in Fig. 5.1) six more fine-meshes were constructed to create a 2 X 4 X 23 mesh system for the CC3-PWR. The mesh layout of the 2 X 4 X 23 system is shown in Table 5.10. This system then was used to analyze a rod ejection event in the same manner as the 2 X 4 X 17 calculation.

Comparison of the total power transients as predicted by the 2 X 4 X 17 and 2 X 4 X 23 calculations is given in Table 5.10, and their relative difference as a function of control rod position (or, function of time) is plotted in Fig. 5.15. The difference is not significant until it reaches time step 9. After time step 9, the difference grows to 0.61%. Comparing Fig. 5.15 with the lower two curves in Fig. 5.13, one is able to see a common behavior, namely the sudden rise at the final stage of transient. In Fig. 5.15, this is regarded as a result of a combination of spatial truncation error (largely from quadratic leakage approximation in QUANDRY model) and accumulated error from time step discretization. It is then reasonable to conclude that the relatively large error (about 2%) in Method 2J (also in Method 2Q) at the final stage of

Table 5.10 Comparison of Total Reactor Powers from Two Fine-Mesh QUANDRY Reference Solutions for a CC3-PWR Transient.

rod tip position Z (cm)	2x4x17* mesh calculation (W)	2x4x23** mesh calculation (W)	difference (%)
100	100.	100.	0.0
102	106.63	106.56	0.07
104	117.05	117.11	0.05
106	128.79	128.89	0.08
108	142.45	142.56	0.08
110	158.15	158.46	0.20
112	176.54	176.72	0.10
114	197.96	197.94	0.01
116	222.56	222.87	0.14
118	250.94	251.96	0.41
120	283.81	285.53	0.61

* axial mesh spacings = 20,20,20,20,20,2,2,2,
2,2,2,2,2,2,2,20,20 cm
from the bottom.

** axial mesh spacings = 20,20,20,20,10,5,3,2,
2,2,2,2,2,2,2,2,2,2,2,2,2,2,2,3,5,10,20 cm from the
bottom.

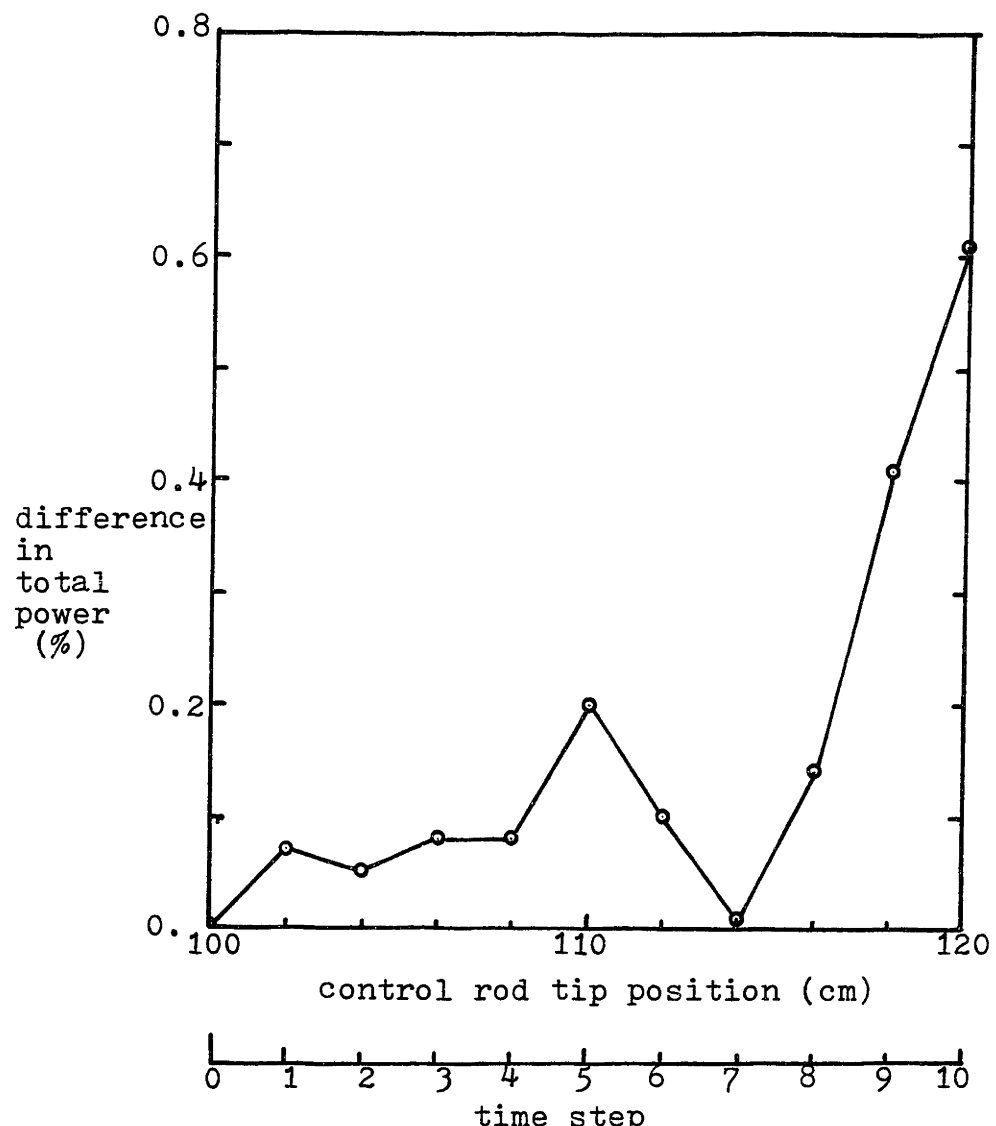


Figure 5.15 Differences in total power levels between $2 \times 4 \times 17$ and $2 \times 4 \times 23$ mesh calculations for a CC3-PWR transient.

**Table 5.11 Axial Power Distributions for the CC3-PWR
with the Rod Tip at 114 cm. $t = 70$ msec.**

(a) plane power density

plane number	reference 2x4x17	error in plane power (%) 2x4x8 calculations		
		VWC	quadratic axial flux	Method 2J
2	1.1547	-18.1	-12.6	-0.33
3	2.1311	-18.3	-12.8	-0.33
4	2.6454	-18.8	-13.2	-0.33
5	2.5477	-19.8	-13.7	-0.33
6	1.8569	-20.7	-14.2	-0.39
7	0.8866	-19.4	-12.8	-0.31

(b) nodal power density of the rodded assembly

plane number	reference 2x4x17	error in nodal power (%) 2x4x8 calculations		
		VWC	quadratic axial flux	Method 2J
2	1.2685	-18.1	-12.6	-0.33
3	2.3393	-18.4	-12.9	-0.31
4	2.8989	-19.0	-13.3	-0.37
5	2.7706	-21.0	-14.8	-0.04
6	1.8260	-25.5	-17.8	-0.05
7	0.6577	-18.0	-10.7	-1.10

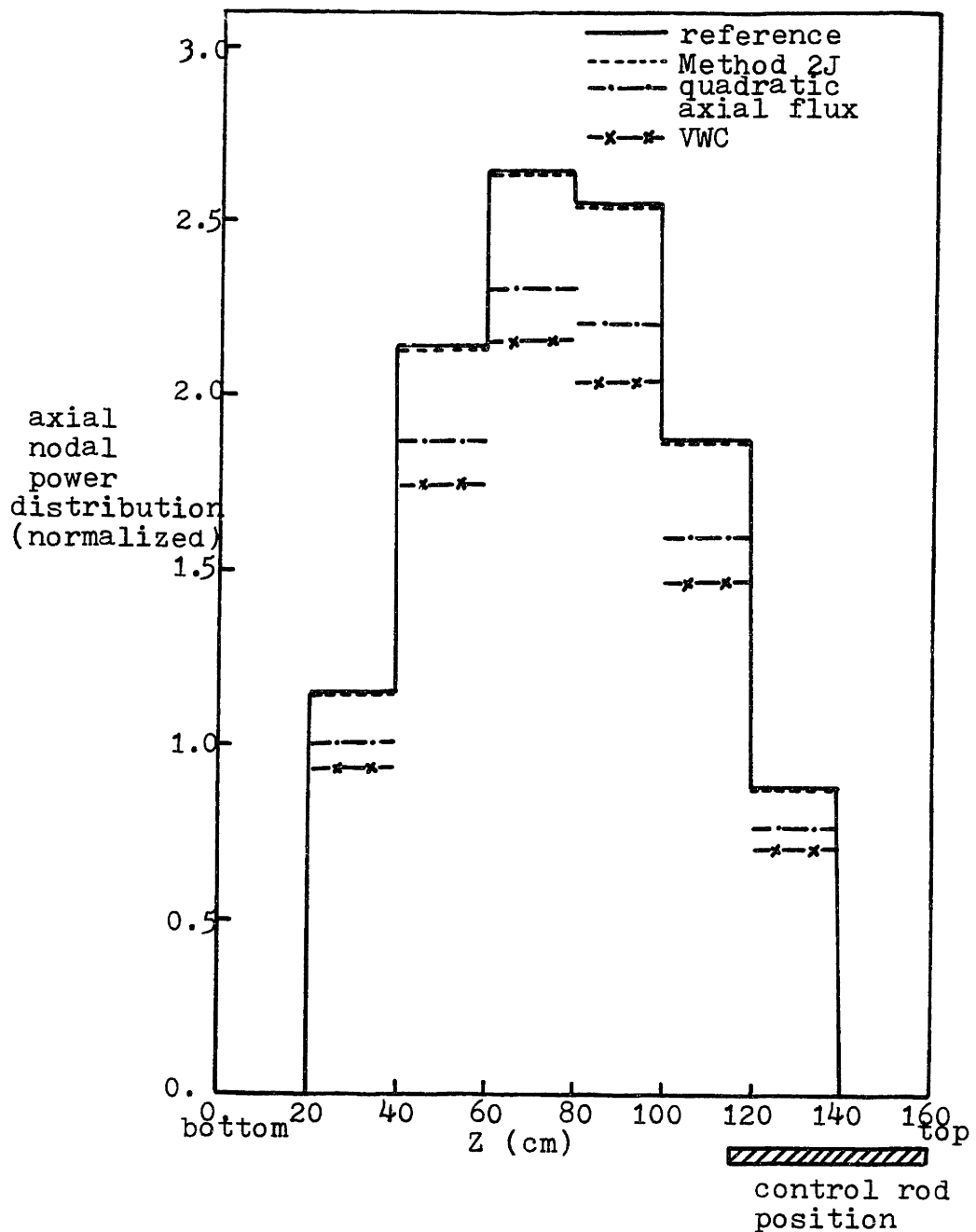


Figure 5.16 Normalized power distributions for the CC3-PWR model at time step 7 during a rod withdrawal.

the transient is at least partially caused by uncertainties in the reference solution rather than totally due to limitations of the Collector-Predictor methodology.

As a final test of the Collector-Predictor method, global power distributions predicted by Method 2J were compared with those predicted by conventional methods. To represent the worst cusping effect, solutions at time step 7 were examined. These are summarized in Table 5.11 and Fig. 5.16. The magnitudes of errors for the conventional methods are unacceptably large and are comparable to those of total reactor power. By Method 2J the axial planar power density was estimated to the accuracy of 99.6%. The same accuracy was obtained in axial nodal power distribution along the rodded assembly except for a rodded node next to the top reflector in which error is -1.1%. And this amount of relative error is not seriously considered because the absolute power density there is far less than those of other nodes.

5.6 Summary

The Collector-Predictor method along with the conventional volume-weighted cross section (VWC) and quadratic axial flux approximation methods, was tested and the results were compared for the CC3-PWR, CISE-BWR and TRD-BWR benchmark problems.

For the CC3-PWR model, static tests were performed for the tip of the control rod located at a wide range of positions. QUANDRY solutions of three-dimensional problems with an extra axial plane inserted at the location of the tip of the control rod in the partially rodded node, were taken as numerical standards. Eigenvalues and power distributions as computed by Method 1 and by the VWC method were compared with these numerical standards. Results showed that Method 1 is far superior to the VWC scheme. The rod cusping effect can be seen to be present for the VWC results but absent when Method 1 is used. The same CC3-PWR model was used for transient tests. The results showed that both Method 1 and Method 2 are much more accurate than the VWC or quadratic axial flux schemes. Since the running time is only marginally greater, Method 2Q or Method 2J (the most accurate) is favored.

A similar study was performed for the TRD-BWR model. Static problems for the rod fixed at various locations in an internal axial node and in an axial node next to the bottom reflector were tested. The acceptability of Method 1 as well as its superiority to the conventional VWC method was again demonstrated. The results of a rod withdrawal transient for the TRD-BWR model showed the inadequacy of the VWC or quadratic flux fix-up schemes and the remarkable accuracy of the two new methods -

particularly Method 2Q. Both for PWR and for BWR benchmark problems the errors in predicted reactor eigenvalues and power distributions decreased by a factor of about 10.

It is believed that these results demonstrate that the new method, the Collector-Predictor method, provides a satisfactory resolution of the control rod cusping problem for the QUANDRY code. The scheme can be applied simply and automatically entirely within the framework of the QUANDRY equations using data already generated during normal operation of the code. It is cheap to implement and appears to yield, consistently, very accurate results.

Chapter 6

SUMMARY AND CONCLUSION

6.1 Overview of the Thesis

The objective of this thesis was to develop and test accurate, reliable and systematic procedures for resolving the control rod cusping problem for nodal methods in light water reactor calculations. Even though the solution of the neutron diffusion equations by finite-difference approximation is standard, obtaining the full-core solution by this method is expensive and computationally inefficient, especially for transient situations. An excellent alternative is the analytic nodal method developed at M.I.T. and embodied in the QUANDRY code. When a reactor is represented by a nodal model, it is customary to homogenize the cross sections over a whole node. The presence of control rods partially inserted in a node and use of inaccurate homogenization parameters there cause the control rod cusping problem. Thus the main task of this study was to develop methods for determining accurate homogenization parameters for a partially rodded node based on the analytic nodal method.

In Chapter 2, nodal equivalence theory and the QUANDRY analytic nodal method for both steady-state and time-dependent problems were reviewed. Also the homogenization parameters

based on equivalence theory and the QUANDRY model were reviewed because of their importance to the resolution of the control rod cusping problem.

Extensive discussion of the control rod cusping problem was presented in Chapter 3. The causes of the cusping problem were analyzed, and several new solution methods were introduced. The feasibility of making use of tabulation-interpolation methods was examined for estimating homogenized cross sections and axial discontinuity factors for a partially rodded node. The volume-weighted cross section approach and an asymptotic axial flux construction method were also introduced. However, it was found that these methods are problem-dependent, and either require complete global calculations or demand considerable machine memory space.

Chapter 4 described a new solution scheme, the Collector-Predictor method. Actually two such methods were developed. The first method (Method 1) is rather simple and useful for steady-state problems, but requires some information from a solution of the same system with no partially rodded nodes. For this reason the second method (Method 2) was introduced. This scheme is adequate for both static and transient problems, and all the required information is internal to the QUANDRY solution. The basic idea of the Collector-Predictor method is to collect

the QUANDRY solution information to predict the axial flux shape in a partially rodded node, and thereby to determine flux-weighted cross sections and axial discontinuity factors. An overall procedure for incorporation of the Collector-Predictor method into the QUANDRY model was described there.

Finally, in Chapter 5, the Collector-Predictor method was employed to solve the control rod cusping problems in steady-state and transient calculations. Several benchmark problems were solved, and the results were examined along with those of the conventional volume-weighted cross section (VWC) and quadratic axial flux approximation methods.

6.2 Results and Conclusion

A partially rodded node (PRN) is present whenever the control rod tip locations do not match exactly the axial nodal interfaces. It was found that if exact homogenized group cross sections and the discontinuity factors (both in radial and in axial directions) for the PRN are given, the control rod cusping problem caused by the presence of the PRN can be eliminated. For the determination of accurate homogenized cross sections and discontinuity factors, four new schemes were devised and examined in this thesis:

- (1) Tabulation and interpolation of the homogenized cross sections and discontinuity factors
- (2) Volume-weighted cross sections and corresponding discontinuity factors
- (3) Asymptotic flux ratio approach
- (4) The Collector-Predictor method
 - Method 1
 - Method 2 --- methods 2F, 2M, 2Q and 2J

For tabulation of flux-weighted cross sections, the relative difference of various types of flux-weighted and volume-weighted cross sections for several positions of the control rod tip in the PRN were approximated by quadratic polynomials. It was found that except for thermal group absorption cross section, the errors in flux-weighted cross sections are negligible. Similarly, an attempt was made to approximate axial discontinuity factors by higher-order polynomials. The motivation for doing this was based on the fact that the general shapes of the discontinuity factor curves are not altered much when the size or composition of the PRN is changed. However, fitting the interpolated curves for the axial discontinuity factors by cubic polynomials or region-wise cubic spline interpolations, resulted in poor agreement, especially in thermal group. Because of the importance of thermal group cross sections and discontinuity factors

in solving the control rod cusping problem, relatively large errors in thermal group parameters make the tabulation-interpolation scheme unattractive. Other drawbacks are that this scheme is strongly problem-dependent, requiring complete global calculations and demands considerable machine memory space.

An approach employing the volume-weighted cross sections and corresponding discontinuity factors was tested for a simple one-dimensional rodded node. The result showed that this approach could not reproduce the exact "individual" reaction rates within the PRN even though it was able to reproduce exact eigenvalue and nodal leakage rate. Along with this drawback, the wide spread in discontinuity factors associated with using simple volume-weighted cross sections provides a potential source of error when these factors must be computed approximately.

Because of the deficiencies of the tabulation and interpolation methods and the inadequacy of volume-weighted cross sections, analytic and problem-independent methods were developed. One of them is an asymptotic axial flux construction method which determines homogenized flux-weighted cross sections by solving for asymptotic one-dimensional flux shape within a PRN neglecting transverse leakages. The accuracy of this method was poor for three-dimensional

problems where the transverse leakages are present. However, this method did lead to an idea for the reconstruction of the axial flux shape by taking the transverse leakage into account -- the Collector-Predictor method.

The Collector-Predictor method can determine accurate homogenized cross sections and the discontinuity factors in axial and radial directions for a partially rodded node. It was embedded in the QUANDRY code, and applied to several static and transient benchmark problems. Numerical standards were taken from fine-mesh QUANDRY solutions of the same problem. For static problems, eigenvalues and power distributions computed by Method 1 and by the VWC method were compared with these numerical standards. Results showed that Method 1 is far superior to the VWC scheme; errors were reduced by a factor of 5 to 10 in the CC3-PWR and the TRD-BWR problems. For transient analyses, both Method 1 and Method 2 were used to estimate total reactor power and nodal power distributions for three transient situations; a rod drop in the TRD-BWR, a rod insertion in the CC3-PWR and a rod ejection event in the CC3-PWR model. The results showed that both Method 1 and Method 2 are much more accurate than the VWC and quadratic axial flux schemes. The control rod cusping effect can be seen to be present in the VWC result and in the quadratic axial flux scheme but absent when Method

2 was used. Both for PWR and for BWR benchmark problems, both global and local errors in predicting power levels caused by making use of the volume-weighted cross sections were reduced by at least a factor of 10, the maximum error being less than 2 % in most cases.

The overall results of application of the Collector-Predictor method to several benchmark problems demonstrated that the Collector-Predictor method is systematic, reliable, problem-independent, and can provide a satisfactory resolution of the control rod cusping problem at a marginal increase in computing time.

6.3 Recommendations for Future Work

Several specific areas of potential interest for the control rod cusping problem have not been explored, and suggestions are made for further study.

1. Additional Testing for an Extended Core

Current application of the Collector-Predictor method was limited to interior sections of reactor cores. Even though the effect of the control rod cusping problem in a low-powered zone such as core periphery is not so serious as in a high-power, interior zone, it would be valuable to extend the testing to a three-dimensional quarter-core or full-core configuration. Because of the difficulty of

gaining access to a three-dimensional, transient, fine-mesh "reference" solution (The memory space of the IBM 3033/N at M.I.T. is 3052K maximum), the investigations in this thesis were restricted to small benchmark problems. However, if such a reference solution were available, the Collector-Predictor method embedded in the QUANDRY code could be examined for an extended core.

2. Application to Thermal-Hydraulic Feedback Problem

The homogenized cross sections and discontinuity factors for fully rodded and completely unrodded nodes involved in the current studies were fixed throughout the transient (no feedback). For more realistic transient problem with thermal-hydraulic feedback effects included, the homogenization parameters will change as the transient proceeds. Conventional tabulation-interpolation seems to be inadequate for this situation because of the large number of cases to be prepared for data acquisition. However, the Collector-Predictor method is expected to be quite efficient even in this situation since all that is required by the Collector-Predictor method is the homogenization parameters for fully rodded and completely unrodded nodes under specific thermal hydraulic conditions. These would be provided by thermal hydraulics model calculations.

3. Non-Unity Axial Discontinuity Factors for Axially Uniform Nodes

It is standard to use unity discontinuity factors in axial direction for an axially uniform (neutronically) node. The use of unity discontinuity factors for a node next to the reflector or for a node of significantly different composition (e.g., fully rodded node and completely unrodded node) has occasionally shown an uncomfortable error in eigenvalue or power distribution, especially in BWR problem. A systematic way of finding accurate non-unity axial discontinuity factors for these nodes is desirable.

REFERENCES

- A-1. A. Ancona, M. Becker, D.R. Harris, A. DaC. Menenzes, M.A. Robinson and D.M. Ver Plank, "Unified Analysis of Nodal Methods," Trans. Amer. Nucl. Soc., 24, 444 (1976).
- B-1. S. Borresen, "A Simplified, Coarse-Mesh, Three-Dimensional Diffusion Scheme for Calculating Gross Power Distributions in a BWR," Nucl. Sci. Eng., 44 (1971).
- B-2. F. Bennewitz, H. Finnemann and M.R. Wagner, "Higher Order Corrections in Nodal Reactor Calculations," Trans. Amer. Nucl. Soc., 22, 250 (1975).
- C-1. W.R. Cadwell, "PDQ-7 Reference Manual," WAPD-TM-678, Bettis Atomic Power Laboratory, Pittsburg, PA, 1967.
- C-2. A.Y. Cheng, A.F. Henry and C.L. Hoxie, "A Method for Determining Equivalent Homogenized Parameters," Proc. of the International Topical Meeting on 'Advances in Mathematical Methods for the Solution of Nuclear Engineering Problems,' Vol.2, April 1981.
- C-3. A.Y. Cheng, "Homogenization of BWR Assemblies by Response Matrix Methods," Ph.D. Thesis, Department of Nuclear Engineering, M.I.T., Cambridge, MA, June 1981.
- C-4. H.S. Cheng and D.J. Diamond, "Analyzing the Rod Drop Accident in a Boiling Water Reactor," Nucl. Tech., 56 (1982).
- D-1. J.J. Dorning, "Modern Coarse-Mesh Methods - A Development of the 70's," Proc. of the ANS Topical Meeting on 'Computational Methods in Nuclear Engineering,' Williamsburg, VA, April 1979.
- D-2. D.L. Delp, D.L. Fischer, J.M. Harriman and M.J. Stedwell, "FLARE - A Three-Dimensional Boiling Water Reactor Simulator," GEAP-4598, General Electric Company, San Jose, CA, July 1964.
- F-1. T.B. Fowler, D.R. Vondy and G.W. Cunningham, "Nuclear Reactor Core Analysis Code: CITATION," ORNL-TM-2406, Oak Ridge National Laboratory, 1969.

REFERENCES
(continued)

- F-2. H. Finnemann, F. Bennewitz and M.R. Wagner, "Interface Current Techniques for Multi-Dimensional Reactor Calculations," Atomkernenergie (ATKE), Bd. 30 (1977).
- F-3. H.D. Fischer and H. Finnemann, "The Nodal Integration Method - A Diverse Solver for Neutron Diffusion Problems," Atomkernenergie (ATKE), Bd. 39 (1981).
- F-4. P.J. Finck, C.L. Hoxie, H.S. Khalil, D.K. Parsons and A.F. Henry, "The Application of Nodal Methods to Light Water Reactors," Proc. of the ANS Topical Meeting on 'Advances in Reactor Physics and Core Thermal Hydraulics,' Vol.1, Kiamesha Lake, NY, September 1982.
- F-5. P.J. Finck, "Homogenization and Dehomogenization Schemes for BWR Assemblies," Ph.D. Thesis, Department of Nuclear Engineering, M.I.T., Cambridge, MA, January 1983.
- F-6. D.R. Ferguson, "Solution of the Space-Dependent Reactor Kinetics Equation in Three Dimensions," MITNE-132, Department of Nuclear Engineering, M.I.T., Cambridge, MA, August 1971.
- F-7. H. Finnemann and W. Gundlach, "Space-Time Kinetics Code IQSBOX for PWR and BWR," Atomkernenergie (ATKE), Bd. 37 (1981).
- G-1. L. Goldstein, F. Nakache and A. Veras, "Calculation of Fuel Cycle Burnup and Power Distribution of the Dresden I Reactor with the TRILUX Fuel Management Program," Trans. Amer. Nucl. Soc., 10 (1967).
- G-2. G. Greenman, K. Smith and A.F. Henry, "Recent Advances in an Analytic Nodal Method for Static and Transient Reactor Analysis," Proc. of the ANS Topical Meeting on 'Computational Methods in Nuclear Engineering,' Vol.1, Williamsburg, VA, April 1979.
- H-1. A.F. Henry, Nuclear-Reactor Analysis, M.I.T. Press, Cambridge, MA, 1975.
- H-2. C.L. Hoxie, "Application of Nodal Equivalence Theory to the Neutronic Analysis of PWR's," Ph.D. Thesis, Department of Nuclear Engineering, M.I.T., Cambridge, MA, June 1982.

REFERENCES
(continued)

- J-1. L.W. Johnson and R.D. Reiss, Numerical Analysis, Addison-Wesley Publishing Company, Reading, MA, 1977.
- K-1. K. Koebke, "A New Approach to Homogenization and Group Condensation," Paper Presented at the IAEA Technical Committee Meeting on 'Homogenization Methods in Reactor Physics,' Lugano, Switzerland, November 1978.
- K-2. H.S. Khalil, "The Application of Nodal Methods to PWR Analysis," Ph.D. Thesis, Department of Nuclear Engineering, M.I.T., Cambridge, MA, January 1983.
- K-3. P.C. Kalambokas and A.F. Henry, "The Replacement of Reflectors by Albedo-Type Boundary Conditions," MITNE-183, Department of Nuclear Engineering, M.I.T., Cambridge, MA, November 1975.
- L-1. R.R. Lee, O. Ozer and W.R. Cobb, "Current Challenges in Light Water Reactors," Proc. of the ANS Topical Meeting on 'Advances in Reactor Physics and Core Thermal Hydraulics,' Vol.1, Kiamesha Lake, NY, September 1982.
- L-2. S. Langenbuch, W. Maurer and W. Werner, "Coarse-Mesh Nodal Diffusion Method for the Analysis of Space-Time Effects in Large Light Water Reactors," Nucl. Sci. Eng., 63 (1977).
- L-3. R.D. Lawrence, "A Nodal Green's Function Method for Multi-Dimensional Neutron Diffusion Calculations," Ph.D. Thesis, Department of Nuclear Engineering, University of Illinois at Urbana-Champaign, Urbana, IL, 1979.
- P-1. D.K. Parsons, "The Replacement of Reflectors and Baffles in Nodal Calculations by Albedo Boundary Conditions," Ph.D. Thesis, Department of Nuclear Engineering, M.I.T., January 1984.
- S-1. F.A.R. Schmidt, "Finite Element Application to Global Reactor Analysis," Proc. of the International Topical Meeting on 'Advances in Mathematical Methods for the Solution of Nuclear Engineering Problems,' Munich, West Germany, April 1981.

REFERENCES
(continued)

- S-2. W.M. Stacey, Jr., Variational Methods in Nuclear Reactor Physics, Academic Press, New York, NY, 1974.
- S-3. R.A. Shober, R.N. Sims and A.F. Henry, "Two Nodal Methods for Solving Time-Dependent Group Diffusion Equations," Nucl. Sci. Eng., 64 (1977).
- S-4. K.S. Smith, "An Analytic Nodal Method for Solving the Two-Group, Multidimensional, Static and Transient Neutron Diffusion Equation," N.E. Thesis, Department of Nuclear Engineering, M.I.T., Cambridge, MA, March 1979.
- S-5. K.S. Smith, "Spatial Homogenization Methods for Light Water Reactor Analysis," Ph.D. Thesis, Department of Nuclear Engineering, M.I.T., Cambridge, MA, June 1980.
- S-6. R.A. Shober, "A Nodal Method for Solving Transient Few-Group Neutron Diffusion Equations," ANL-78-51, Argonne National Laboratory, June 1978.
- S-7. K.S. Smith, A.F. Henry and R.A. Loretz, "The Determination of Homogenized Diffusion Theory Parameters for Coarse Mesh Nodal Analysis," Proc. of the ANS Topical Meeting on '1980 Advances in Reactor Physics and Shielding,' Sun Valley, ID, September 1980.
- V-1. A.V. Vota, N.J. Curlee, Jr. and A.F. Henry, "WIGL3-A Program for the Steady-State and Transient Solution of the One-Dimensional, Two-Group, Space-Time Diffusion Equations Accounting for Temperature, Xenon, and Control Feedback," WAPD-TM-788, Bettis Atomic Power Laboratory, Pittsburgh, PA, February 1969.
- W-1. Z. Weiss and S.O. Lindahl, "High-Order Response Matrix Equations in Two-Dimensional Geometry," Nucl. Sci. Eng., 58 (1975).
- W-2. W. Werner, H. Finnemann and S. Langenbuch, "Two- and Three-Dimensional BWR Kinetics Problem," Trans. Amer. Nucl. Soc., 23 (1976).
- W-3. E.L. Wachspress, Iterative Solution to Elliptic Systems and Applications to the Neutron Diffusion Equations of Reactor Physics, Prentice-Hall, Englewood Cliffs, NJ, 1966.

APPENDICES

- Appendix 1.** **The Homogenization Parameters for a Partially Rodded Node.**
- Appendix 2.** **A Quadratic Expansion for Transverse Leakages and Corresponding Homogenized Surface Flux.**
- Appendix 3.** **Cross Sections and Mesh Layout for the CC3-PWR.**
- Appendix 4.** **Cross Sections and Mesh Layout for BWR Models.**
- Appendix 5.** **Temporal Truncation Error for the CC3-PWR.**

Appendix 1

THE HOMOGENIZATION PARAMETERS FOR A PARTIALLY RODDED NODE

Al.1 Flux-Weighted Cross Sections for a 3 X 3 X 3 System

Table Al.1 **Flux-Weighted Cross Sections vs. Control Rod Tip Position for a Partially Rodded Node in a 3 X 3 X 3 System (Fig. 3.3).**

rod tip position h_c (cm)	group g	\bar{D}_g (cm)	$\bar{\Sigma}_{t_g}$ (cm ⁻¹)	$\bar{\Sigma}_{gg'}$ (cm ⁻¹)	$v\bar{\Sigma}_{f_g}$ (cm ⁻¹)
0.0	1	1.513	0.03045	0.02113	0.004625
	2	0.3951	0.1414	0.0	0.1645
5.0	1	1.5017	0.031283	0.021165	0.0046268
	2	0.39158	0.1510	0.0	0.16567
7.5	1	1.4958	0.031715	0.021184	0.0046277
	2	0.38971	0.15619	0.0	0.16631
10.0	1	1.4898	0.032169	0.021203	0.0046286
	2	0.38764	0.16196	0.0	0.16701
15.0	1	1.4768	0.033156	0.021245	0.0046307
	2	0.38281	0.17570	0.0	0.16869
17.5	1	1.4699	0.033683	0.021267	0.0046319
	2	0.38004	0.18374	0.0	0.16968
20.0	1	1.4630	0.03422	0.02129	0.004633
	2	0.3772	0.19210	0.0	0.1707

$v = 2.5$

A1.2 Interpolations of the Axial Discontinuity Factors

In Fig. 3.5 of Chapter 3, two polynomial interpolations of the axial discontinuity factor for a partially rodded node were illustrated. This section gives those polynomials and data for the curves in Fig. 3.5.

A1.2.1 A Cubic Polynomial Interpolation

A cubic polynomial for approximate discontinuity factors f_g^{\pm} in terms of the position of a control rod tip, h_c , is given by

$$f_g^{\pm} \approx ah_c^3 + bh_c^2 + ch_c + d$$

To determine four unknowns a , b , c and d , two end points at $h_c = 0$ and 20 cm and two additional, arbitrary points at $h_c = 7.5$ and 15 cm (Table 3.3) were interpolated.

Solving for a , b , c and d yields

$$a = -\frac{f_g^{\pm}(15.0) - 1}{562.5} + \frac{f_g^{\pm}(7.5) - 1}{703.125}$$

$$b = \frac{f_g^{\pm}(15.0) - 1}{20.455} - \frac{f_g^{\pm}(7.5) - 1}{20.089}$$

$$c = \frac{f_g^{\pm}(7.5) - 1}{7.5} - 56.25a - 7.5b$$

$$d = 1$$

The interpolated values of the axial discontinuity factors are given in Table A1.2.

Table Al.2 The Axial Discontinuity Factors Interpolated
by a Cubic Polynomial for a Partially
Rodded Node in a 3 X 3 X 3 System (Fig. 3.3).

rod tip position h_c (cm)	f_1^-	f_2^-	f_1^+	f_2^+
0.0	1.0	1.0	1.0	1.0
1.0	1.0113	1.0005	0.9723	0.9308
3.0	1.0335	1.0285	0.9307	0.8289
5.0	1.0542	1.0816	0.9057	0.7702
7.0	1.0716	1.1471	0.8947	0.7475
8.0	1.0787	1.1806	0.8937	0.7476
10.0	1.0884	1.2411	0.8993	0.7661
12.5	1.0905	1.2881	0.9173	0.8147
14.0	1.0852	1.2915	0.9322	0.8522
16.0	1.0691	1.2560	0.9548	0.9060
17.5	1.0493	1.1923	0.9724	0.9452
19.0	1.0224	1.0910	0.9894	0.9803
20.0	1.0	1.0	1.0	1.0

A1.2.2 A Cubic Spline Interpolation

Given a set of points, $x_n = \{x_j\}_{j=0}^n$ where $a = x_0 < x_1 < \dots < x_n = b$, and a set of functional values, $\{F(x_j)\}_{j=0}^n$, a piece-wise cubic spline, $S_j(x)$, interpolating at all x_j is given in $x_j \leq x \leq x_{j+1}$ by [J-1]

$$S_j(x) = \frac{y_j''}{6h_j} (x_{j+1} - x)^3 + \frac{y_{j+1}''}{6h_j} (x - x_j)^3 + \left(\frac{F_{j+1}}{h_j} - \frac{y_{j+1}'' h_j}{6} \right) (x - x_j) + \left(\frac{F_j}{h_j} - \frac{y_j'' h_j}{6} \right) (x_{j+1} - x)$$

$0 \leq j \leq n - 1$

where $F_j = F(x_j)$

$h_j = x_{j+1} - x_j$

$y_j'' = S''(x_j)$

This cubic spline $S(x)$ satisfies the following three properties:

1. $S(x) \in C^2[a, b]$
2. $S(x_j) = F(x_j)$ for $0 \leq j \leq n$
3. $S(x)$ is a cubic polynomial on each subinterval $[x_j, x_{j+1}]$ for $0 \leq j \leq n-1$.

To specify $S_j(x)$, y_j'' must be found. This can be accomplished by requiring $S_j'(x_j) = S_{j-1}'(x_j)$ for $1 \leq j \leq n-1$. This yields the following linear system of $(n-1)$ equations in the unknowns $\{y_j''\}_{j=0}^n$:

$$h_{j-1} y_{j-1}'' + 2(h_j + h_{j-1}) y_j'' + h_j y_{j+1}'' = 6 \left(\frac{\Delta F_j}{h_j} - \frac{\Delta F_{j-1}}{h_{j-1}} \right)$$

where $\Delta F_j = F_{j+1} - F_j$. It is common to set $y_0'' = y_n'' = 0$ in order to form a "natural cubic spline".

A three-region natural cubic spline was chosen for approximating axial discontinuity factors in Fig. 3.5 as the following:

$$x_0 = 0 \quad x_1 = 7.5 \text{ cm} \quad x_2 = 15 \text{ cm} \quad x_3 = 20 \text{ cm}$$

$$h_0 = 7.5 \text{ cm} \quad h_1 = 7.5 \text{ cm} \quad h_2 = 5 \text{ cm}$$

$$F_0 = 1.0 \quad F_3 = 1.0$$

F_1 = discontinuity factors at $h_c = 7.5 \text{ cm}$ (Table 3.3)

F_2 = discontinuity factors at $h_c = 15 \text{ cm}$ (Table 3.3)

The results are tabulated in Table A1.3 for several values of the control rod tip position h_c for a $3 \times 3 \times 3$ system shown in Fig. 3.3.

A1.3 Volume-Weighted Cross Sections and Corresponding Axial Discontinuity Factors

This section provides a test problem examining the use of volume-weighted cross sections ($\bar{\Sigma}_\alpha g$) and their corresponding discontinuity factors as homogenization parameters for a partially rodded node (PRN). (see Section 3.4.2 of Chapter 3). For simplicity, a one-dimensional $1 \times 1 \times 3$ node problem (Fig. 3.3b) is tested:

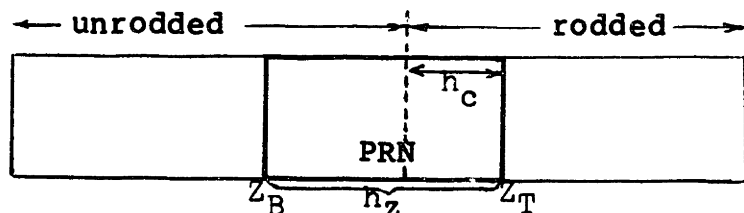


Table A1.3 The Axial Discontinuity Factors Interpolated by a Natural Cubic Spline Function for a Partially Rodded Node in a 3 X 3 X 3 System (Fig. 3.3).

rod tip position h_c (cm)	f_1^-	f_2^-	f_1^+	f_2^+
0.0	1.0	1.0	1.0	1.0
1.0	1.0113	1.0179	0.9807	0.9531
3.0	1.0334	1.0553	0.9444	0.8650
5.0	1.0538	1.0980	0.9147	0.7940
7.0	1.0714	1.1494	0.8962	0.7515
8.0	1.0789	1.1794	0.8925	0.7445
10.0	1.0898	1.2418	0.8961	0.7582
12.5	1.0927	1.2953	0.9156	0.8108
14.0	1.0865	1.2973	0.9318	0.8514
16.0	1.0671	1.2458	0.9547	0.9051
17.5	1.0448	1.1684	0.9718	0.9420
19.0	1.0186	1.0705	0.9887	0.9771
20.0	1.0	1.0	1.0	1.0

Let us assume that an exact heterogeneous solution is known and consequently flux-weighted cross sections for the PRN ($\bar{\Sigma}_{\alpha g}^F$) are determined. When h_c is specified, $\bar{\Sigma}_{\alpha g}^V$ is readily known. From Eq. 2.7, we can obtain two sets of neutron balance equations within the PRN associated with $\bar{\Sigma}_{\alpha g}^F$ and $\bar{\Sigma}_{\alpha g}^V$, respectively. Those are

$$\left\{ \begin{array}{l} \frac{1}{h_z} [\bar{J}_1^F(z_T) - \bar{J}_1^F(z_B)] + \bar{\Sigma}_1^F \bar{\phi}_1^F = \frac{1}{k_{eff}^F} v \bar{\Sigma}_{f_2}^F \bar{\phi}_2^F \\ \frac{1}{h_z} [\bar{J}_2^F(z_T) - \bar{J}_2^F(z_B)] + \bar{\Sigma}_2^F \bar{\phi}_2^F = \bar{\Sigma}_{21}^F \bar{\phi}_1^F \end{array} \right. \quad (Al.1)$$

and

$$\left\{ \begin{array}{l} \frac{1}{h_z} [\bar{J}_1^V(z_T) - \bar{J}_1^V(z_B)] + \bar{\Sigma}_1^V \bar{\phi}_1^V = \frac{1}{k_{eff}^V} v \bar{\Sigma}_{f_2}^V \bar{\phi}_2^V \\ \frac{1}{h_z} [\bar{J}_2^V(z_T) - \bar{J}_2^V(z_B)] + \bar{\Sigma}_2^V \bar{\phi}_2^V = \bar{\Sigma}_{21}^V \bar{\phi}_1^V \end{array} \right. \quad (Al.2)$$

where $\bar{\Sigma}_1 \equiv \bar{\Sigma}_{t_1} - \frac{1}{k_{eff}} v \bar{\Sigma}_{f_1}$, and the superscripts F and V represent properties of the PRN associated with $\bar{\Sigma}_{\alpha g}^F$ or $\bar{\Sigma}_{\alpha g}^V$. Forcing Eq. Al.2 to preserve eigenvalue and surface currents given by Eq. Al.1 yields

$$\begin{bmatrix} \bar{\phi}_1^V \\ \bar{\phi}_2^V \end{bmatrix} = \begin{bmatrix} \bar{\Sigma}_1^V & \frac{-1}{k_{eff}^V} v \bar{\Sigma}_{f_2}^V \\ -\bar{\Sigma}_{21}^V & \bar{\Sigma}_2^V \end{bmatrix}^{-1} \begin{bmatrix} \bar{\Sigma}_1^F & \frac{-1}{k_{eff}^F} v \bar{\Sigma}_{f_2}^F \\ -\bar{\Sigma}_{21}^F & \bar{\Sigma}_2^F \end{bmatrix} \begin{bmatrix} \bar{\phi}_1^F \\ \bar{\phi}_2^F \end{bmatrix}$$

Thus, substituting this $[\bar{\phi}_1 \quad \bar{\phi}_2]^T$ and surface currents $\bar{J}_g^F(z_B)$ and $\bar{J}_g^F(z_T)$ in the last equation of Appendix 2.3 produces homogenized surface fluxes, $\bar{\phi}_g^{V,hom}$, corresponding to the use of $\bar{\Sigma}_{\alpha g}^V$, and consequently discontinuity factors, f_g^V , corresponding to the use of $\bar{\Sigma}_{\alpha g}^V$.

For numerical test, cross sections given in Table 3.1 was used for the PRN of $h_c = 10$ cm and $h_z = 20$ cm. Data and results are summarized below.

	using $\bar{\Sigma}_{\alpha g}^F$		using $\bar{\Sigma}_{\alpha g}^V$	
	g=1	g=2	g=1	g=2
\bar{D}_g	1.4949	0.38951	1.488	0.38615
$\bar{\Sigma}_{tg}$	0.03179	0.15673	0.032335	0.16675
$\bar{\Sigma}_{gg'}$	0.02119	0.0	0.02121	0.0
$v\bar{\Sigma}_{fg}$	0.004628	0.16637	0.004629	0.1676
$\bar{\phi}_g$	2.8236E13	3.8317E12	1.2911E13	1.6560E12
$\bar{J}_g(z_B)$	2.1692E12	8.4595E10	- -	- -
$\bar{J}_g(z_T)$	1.3373E12	3.8720E10	- -	- -
$\bar{\phi}_g(z_B)$	4.4483E13	6.6218E12	2.4844E13	3.2251E12
$\bar{\phi}_g(z_T)$	1.3999E13	1.5682E12	2.8390E12	3.8482E11
$f_g(z_B)$	1.0979	1.1990	1.7905	2.0532
$f_g(z_T)$	0.7855	0.6403	4.9310	4.0750

Using $\bar{\Sigma}_{\alpha g}^V$ and f_g^V in the 1 X 1 X 3 problem resulted in the exact value in k_{eff} . However, individual reaction rates for the PRN were not preserved by introducing $\bar{\Sigma}_{\alpha g}^V$ and f_g^V .

Appendix 2

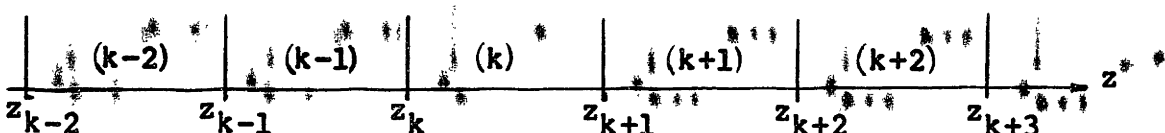
A Quadratic Expansion for Transverse Leaks and Corresponding Homogenized Surface Flux and Corresponding Homogenized Surface Flux

A.1 Expansion Coefficients for a Quadratic Transverse Leakage Approximation

In Section 4.3, for solving Eq. 4.1 for an axial flux shape, the transverse leakage term $S_g^k(z)$ was approximated by Eq. 4.2 as

$$S_g^k(z) \approx \sum_{j=0}^2 Q_{gj}^k z^j$$

The expansion coefficients Q_{gj}^k are determined so that the integrals of the approximated shapes over a region of interest (k) and its two adjacent regions (k-1) and (k+1) preserve the average transverse leakages of these three regions. Here, each region can be either a subnode in the partially rodded node or a whole node next to the partially rodded node as illustrated below.



Thus, the requirement for finding Q_{gj}^k is as follows:

$$(z_k - z_{k-1}) \bar{S}_g^{k-1} = \int_{z_{k-1}}^{z_k} (Q_{g_0}^k + Q_{g_1}^k z + Q_{g_2}^k z^2) dz$$

$$(z_{k+1} - z_k) \bar{S}_g^k = \int_{z_k}^{z_{k+1}} (Q_{g_0}^k + Q_{g_1}^k z + Q_{g_2}^k z^2) dz$$

$$(z_{k+2} - z_{k+1}) \bar{S}_g^{k+1} = \int_{z_{k+1}}^{z_{k+2}} (Q_{g_0}^k + Q_{g_1}^k z + Q_{g_2}^k z^2) dz$$

Solving for the three unknown coefficients, we obtain

$$Q_{g_2}^k = \frac{(\bar{S}_g^{k-1} - \bar{S}_g^k) - (\bar{S}_g^k - \bar{S}_g^{k+1})}{(B_1 - B_2) - (B_2 - B_3)} \frac{(A_1 - A_2)/(A_2 - A_3)}{(A_1 - A_2)/(A_2 - A_3)}$$

$$Q_{g_1}^k = \frac{(\bar{S}_g^{k-1} - \bar{S}_g^k) - (\bar{S}_g^k - \bar{S}_g^{k+1})}{(A_1 - A_2) - (A_2 - A_3)} \frac{(B_1 - B_2)/(B_2 - B_3)}{(B_1 - B_2)/(B_2 - B_3)}$$

$$Q_{g_0}^k = \bar{S}_g^k - A_2 Q_{g_1}^k - B_2 Q_{g_2}^k$$

$$\text{where } A_m \equiv \frac{1}{2} (z_{k+m-1} + z_{k+m-2})$$

$$B_m \equiv \frac{1}{3} (z_{k+m-1}^2 + z_{k+m-1} z_{k+m-2} + z_{k+m-2}^2).$$

A2.2 A Particular Solution for the Axial Flux

The linear nonhomogeneous equation, Eq. 4.1, can be solved completely for an axial flux shape $\bar{\phi}_g^k(z)$ if a particular solution $P_g^k(z)$ in Eq. 4.3 is found in terms of a quadratic polynomial with the nonhomogeneous term $S_g^k(z)$ approximated by a quadratic polynomial as determined in the previous section.

In Section 4.3.1, $p_g^k(z)$ was given in the form,

$$\begin{bmatrix} p_1^k(z) \\ p_2^k(z) \end{bmatrix} = \begin{bmatrix} p_1^k & p_2^k \\ q_1^k & q_2^k \end{bmatrix} \begin{bmatrix} z^2 \\ z \end{bmatrix} + \begin{bmatrix} p_3^k \\ q_3^k \end{bmatrix}$$

To determine the unknowns p_j^k and q_j^k ($j = 1, 2, 3$), we may use the method of undetermined coefficients. Then, Eq. 4.1 can be written as

$$\begin{bmatrix} D_1^k \frac{d^2}{dz^2} - \Sigma_1^k & \frac{1}{k_{\text{eff}}} v \Sigma f_2^k \\ \Sigma_{21}^k & D_2^k \frac{d^2}{dz^2} - \Sigma_2^k \end{bmatrix} \begin{bmatrix} p_1^k & p_2^k \\ q_1^k & q_2^k \end{bmatrix} + \begin{bmatrix} z^2 \\ z \end{bmatrix} + \begin{bmatrix} p_3^k \\ q_3^k \end{bmatrix} \\ = \begin{bmatrix} Q_{12}^k & Q_{11}^k \\ Q_{22}^k & Q_{21}^k \end{bmatrix} \begin{bmatrix} z^2 \\ z \end{bmatrix} + \begin{bmatrix} Q_{10}^k \\ Q_{20}^k \end{bmatrix}$$

Thus, making use of the method of unknown coefficients, we obtain the following six linear equations for six unknowns, p_j^k and q_j^k ($j = 1, 2, 3$):

$$\begin{bmatrix} -\Sigma_1^k & \frac{1}{k_{\text{eff}}} v \Sigma f_2^k \\ \Sigma_{21}^k & -\Sigma_2^k \end{bmatrix} \begin{bmatrix} p_1^k & p_2^k \\ q_1^k & q_2^k \end{bmatrix} = \begin{bmatrix} Q_{12}^k & Q_{11}^k \\ Q_{22}^k & Q_{21}^k \end{bmatrix}$$

and

$$\begin{bmatrix} -\Sigma_1^k & \frac{1}{k_{\text{eff}}} v \Sigma f_2^k \\ \Sigma_{21}^k & -\Sigma_2^k \end{bmatrix} \begin{bmatrix} p_3^k \\ q_3^k \end{bmatrix} = \begin{bmatrix} Q_{10}^k - 2D_1^k p_1^k \\ Q_{20}^k - 2D_2^k q_1^k \end{bmatrix}$$

Finally, solving for p_3^k and q_3^k yields

$$\begin{bmatrix} p_1^k & p_2^k \\ q_1^k & q_2^k \end{bmatrix} = \frac{1}{M} \begin{bmatrix} \Sigma_2^k & \frac{1}{k_{\text{eff}}} v \Sigma f_2^k \\ \Sigma_{21}^k & \Sigma_1^k \end{bmatrix} \begin{bmatrix} Q_{12}^k & Q_{11}^k \\ Q_{22}^k & Q_{21}^k \end{bmatrix}$$

and

$$\begin{bmatrix} p_3^k \\ q_3^k \end{bmatrix} = \frac{1}{M} \begin{bmatrix} \Sigma_2^k & \frac{1}{k_{\text{eff}}} v \Sigma f_2^k \\ \Sigma_{21}^k & \Sigma_1^k \end{bmatrix} \begin{bmatrix} Q_{10}^k - 2D_1^k p_1^k \\ Q_{20}^k - 2D_2^k q_1^k \end{bmatrix}$$

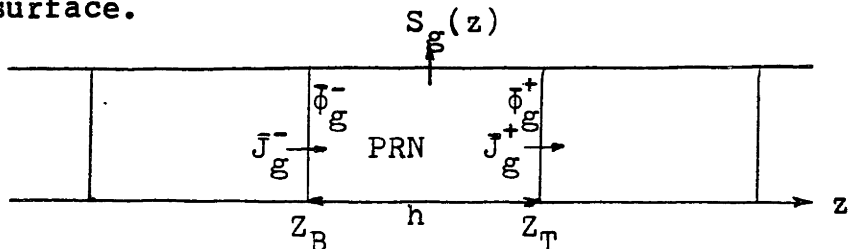
where

$$M \equiv \frac{1}{k_{\text{eff}}} v \Sigma f_2^k \Sigma_{21}^k - \Sigma_1^k \Sigma_2^k.$$

A2.3 Homogenized Surface Flux

As discussed in Section 4.3, for finding the axial discontinuity factors for a partially rodded node (PRN), the homogenized surface fluxes should be determined so that they preserve nodal reaction rates, surface current and reactor eigenvalue. In this section, a formula for the homogenized surface flux for a PRN will be derived. A diagram shown on the following page illustrates a homogenized PRN along with its adjacent nodes. The axial positions z_B and z_T represent the bottom and the top of the PRN. The surface net-currents and homogenized surface fluxes at z_T and z_B are designated as \bar{J}_g^{\pm} and

$\bar{\phi}_g^\pm$: plus sign (+) for z_T surface and minus sign (-) for z_B surface.



The transverse leakage $S_g(z)$ is approximated by a quadratic polynomial, and a particular solution for Eq. 4.3 is found from a formula given in Section A2.2. Then a general solution for an axial flux in the homogenized PRN can be given (from Eq. 4.3) as

$$\begin{bmatrix} \bar{\phi}_1(z) \\ \bar{\phi}_2(z) \end{bmatrix} = \begin{bmatrix} 1 & 1 \\ r & s \end{bmatrix} \left\{ \begin{bmatrix} \frac{1}{K} \sin[Kz_n] & 0 \\ 0 & \frac{1}{U} \sinh[Uz_n] \end{bmatrix} \begin{bmatrix} KC_1 \\ UC_3 \end{bmatrix} + \begin{bmatrix} \cos[Kz_n] & 0 \\ 0 & \cosh[Uz_n] \end{bmatrix} \begin{bmatrix} C_2 \\ C_4 \end{bmatrix} \right\} + \begin{bmatrix} p_1 & p_2 \\ q_1 & q_2 \end{bmatrix} \begin{bmatrix} z^2 \\ z \end{bmatrix} + \begin{bmatrix} p_3 \\ q_3 \end{bmatrix} \quad (A2.1)$$

All constants are found from the homogenized cross sections of the PRN. First, the surface flux $\bar{\phi}_g^-$ at $z = z_B$ is considered. For this, we define $z_n = z - z_B$. At $z = z_B$, Eq. A2.1 then gives

$$\begin{bmatrix} \bar{\phi}_1^- \\ \bar{\phi}_2^- \end{bmatrix} = \begin{bmatrix} 1 & 1 \\ r & s \end{bmatrix} \begin{bmatrix} C_2 \\ C_4 \end{bmatrix} + \begin{bmatrix} p_1 & p_2 \\ q_1 & q_2 \end{bmatrix} \begin{bmatrix} z_B^2 \\ z_B \end{bmatrix} + \begin{bmatrix} p_3 \\ q_3 \end{bmatrix} \quad (A2.2)$$

The corresponding surface current \bar{J}_g^- is

$$\begin{bmatrix} -\frac{1}{D_1} \bar{J}_1^- \\ -\frac{1}{D_2} \bar{J}_2^- \end{bmatrix} = \begin{bmatrix} 1 & 1 \\ r & s \end{bmatrix} \begin{bmatrix} KC_1 \\ UC_3 \end{bmatrix} + \begin{bmatrix} p_1 & p_2 \\ q_1 & q_2 \end{bmatrix} \begin{bmatrix} 2z_B \\ 1 \end{bmatrix}$$

(A2.3)

And node-averaged flux is found by integrating Eq. A2.1:

$$\begin{bmatrix} \bar{\phi}_1 \\ \bar{\phi}_2 \end{bmatrix} = \frac{1}{h} \begin{bmatrix} 1 & 1 \\ r & s \end{bmatrix} \left\{ \begin{bmatrix} \frac{1}{K^2} (1 - \cos [Kh]) & 0 \\ 0 & -\frac{1}{U^2} (1 - \cosh [Uh]) \end{bmatrix} \begin{bmatrix} KC_1 \\ UC_3 \end{bmatrix} + \right.$$

$$\left. \begin{bmatrix} \frac{1}{K} \sin [Kh] & 0 \\ 0 & \frac{1}{U} \sinh [Uh] \end{bmatrix} \begin{bmatrix} C_2 \\ C_4 \end{bmatrix} \right\} + \begin{bmatrix} p_3 \\ q_3 \end{bmatrix}$$

(A2.4)

To find the unknowns C_2 and C_4 for the surface flux in Eq. A2.2, we can eliminate KC_1 and UC_3 in Eqs. A2.3 and A2.4. From Eq. A2.3 we obtain

$$\begin{bmatrix} KC_1 \\ UC_3 \end{bmatrix} = \frac{1}{(s-r)} \begin{bmatrix} s & -1 \\ -r & 1 \end{bmatrix} \left\{ \begin{bmatrix} -\frac{1}{D_1} \bar{J}_1^- \\ -\frac{1}{D_2} \bar{J}_2^- \end{bmatrix} - [B^-] \right\}$$

(A2.5)

where

$$[B^-] \equiv \begin{bmatrix} p_1 & p_2 \\ q_1 & q_2 \end{bmatrix} \begin{bmatrix} 2z_B \\ 1 \end{bmatrix}$$

From Eq. A2.4 we have

$$\begin{bmatrix} C_2 \\ C_4 \end{bmatrix} = \frac{1}{(s-r)} \begin{bmatrix} Kh/\sin[Kh] & 0 \\ 0 & Uh/\sinh[Uh] \end{bmatrix} \begin{bmatrix} s & -1 \\ -r & 1 \end{bmatrix} \left\{ \begin{bmatrix} \bar{\phi}_1 \\ \bar{\phi}_2 \end{bmatrix} - [C] - \frac{1}{h} \begin{bmatrix} 1 & 1 \\ r & s \end{bmatrix} \begin{bmatrix} \frac{1}{K^2} (1 - \cos[Kh]) & 0 \\ 0 & -\frac{1}{U^2} (1 - \cosh[Uh]) \end{bmatrix} \begin{bmatrix} KC_1 \\ UC_3 \end{bmatrix} \right\} \quad (A2.6)$$

where

$$[C] \equiv \begin{bmatrix} p_1 & p_2 \\ q_1 & q_2 \end{bmatrix} \begin{bmatrix} \frac{1}{3} (z_T^2 + z_T z_B + z_B^2) \\ \frac{1}{2} (z_T + z_B) \end{bmatrix} + \begin{bmatrix} p_3 \\ q_3 \end{bmatrix}$$

Eliminating KC_1 and UC_3 from Eqs. A2.5 and A2.6, and substituting the resultant C_2 and C_4 into Eq. 2.2 yields

$$\begin{bmatrix} \bar{\phi}_1 \\ \bar{\phi}_2 \end{bmatrix} = \frac{1}{(s-r)} \begin{bmatrix} 1 & 1 \\ r & s \end{bmatrix} \begin{bmatrix} Kh/\sin[Kh] & 0 \\ 0 & Uh/\sinh[Uh] \end{bmatrix} \begin{bmatrix} s & -1 \\ -r & 1 \end{bmatrix} \left\{ \begin{bmatrix} \bar{\phi}_1 \\ \bar{\phi}_2 \end{bmatrix} - [C] \right\}$$

$$- \frac{h}{(s-r)} \begin{bmatrix} 1 & 1 \\ r & s \end{bmatrix} \begin{bmatrix} \frac{1 - \cos[Kh]}{Kh \sin[Kh]} & 0 \\ 0 & \frac{-1 + \cosh[Uh]}{Uh \sinh[Uh]} \end{bmatrix} \begin{bmatrix} s & -1 \\ -r & 1 \end{bmatrix} \left\{ \begin{bmatrix} -\frac{1}{D_1} \bar{J}_1 \\ -\frac{1}{D_2} \bar{J}_2 \end{bmatrix} \right\}$$

$$- [B^-] + [A^-]$$

where

$$[A^-] \equiv \begin{bmatrix} p_1 & p_2 \\ q_1 & q_2 \end{bmatrix} \begin{bmatrix} z_B^2 \\ z_B \end{bmatrix} + \begin{bmatrix} p_3 \\ q_3 \end{bmatrix}$$

Next, the surface flux $\bar{\phi}_g^+$ at $z = z_T$ can be found in the same manner by defining $z_n = z_T - z$ in Eq. A2.1. Thus defining

$$[A^+] \equiv \begin{bmatrix} p_1 & p_2 \\ q_1 & q_2 \end{bmatrix} \begin{bmatrix} z_T^2 \\ z_T \end{bmatrix} + \begin{bmatrix} p_3 \\ q_3 \end{bmatrix}$$

and

$$[B^+] \equiv \begin{bmatrix} p_1 & p_2 \\ q_1 & q_2 \end{bmatrix} \begin{bmatrix} 2z_T \\ 1 \end{bmatrix},$$

we can have a final formula for group surface fluxes,

$$\begin{bmatrix} \bar{\phi}_1^+ \\ \bar{\phi}_2^+ \end{bmatrix} = \frac{1}{(s-r)} \begin{bmatrix} 1 & 1 \\ r & s \end{bmatrix} \begin{bmatrix} Kh \csc[Kh] & 0 \\ 0 & Uh \csch[Uh] \end{bmatrix} \begin{bmatrix} s & -1 \\ -r & 1 \end{bmatrix} \left\{ \begin{bmatrix} \bar{\phi}_1 \\ \bar{\phi}_2 \end{bmatrix} \right.$$

$$\left. - [C] \right\} \pm \frac{h}{(s-r)} \begin{bmatrix} 1 & 1 \\ r & s \end{bmatrix} \begin{bmatrix} \frac{1}{Kh} \tan[\frac{Kh}{2}] & 0 \\ 0 & \frac{1}{Uh} \tanh[\frac{Uh}{2}] \end{bmatrix} \begin{bmatrix} s & -1 \\ -r & 1 \end{bmatrix}$$

$$\left\{ \begin{bmatrix} -\frac{1}{D_1} \bar{J}_1^+ \\ -\frac{1}{D_2} \bar{J}_2^+ \end{bmatrix} - [B^+] \right\} + [A^+].$$

For $K^2 < 0$, it is necessary to replace as follows:

$$Kh \csc [Kh] \rightarrow \sqrt{|K^2|} h \csch [\sqrt{|K^2|} h]$$

$$\frac{1}{Kh} \tan [\frac{Kh}{2}] \rightarrow \frac{1}{\sqrt{|K^2|} h} \tanh [\frac{1}{2} \sqrt{|K^2|} h]$$

Appendix 3
CROSS SECTIONS AND MESH LAYOUT FOR THE CC3-PWR

**Table A3.1 Heterogeneous, Two-Group Cross Sections
for Pin Cells of the CC3-PWR.**

type	group g	D _g (cm)	Σ _{tg} (cm ⁻¹)	Σ _{gg'} (cm ⁻¹)	vΣ _{fg} (cm ⁻¹)
fuel 1	1	1.50	0.033	0.02	0.0065
	2	0.40	0.18	0.0	0.24
fuel 2	1	1.50	0.03	0.02	0.005
	2	0.40	0.15	0.0	0.18
control rod	1	1.113	0.0838	0.0038	0.0
	2	0.184	0.96	0.0	0.0
water	1	1.70	0.036	0.035	0.0
	2	0.35	0.050	0.0	0.0

$$v = 2.5$$

$$\Sigma_{tg} = \Sigma_{ag} + \Sigma_{gg'}$$

$$x_1 = 1.0$$

$$x_2 = 0.0$$

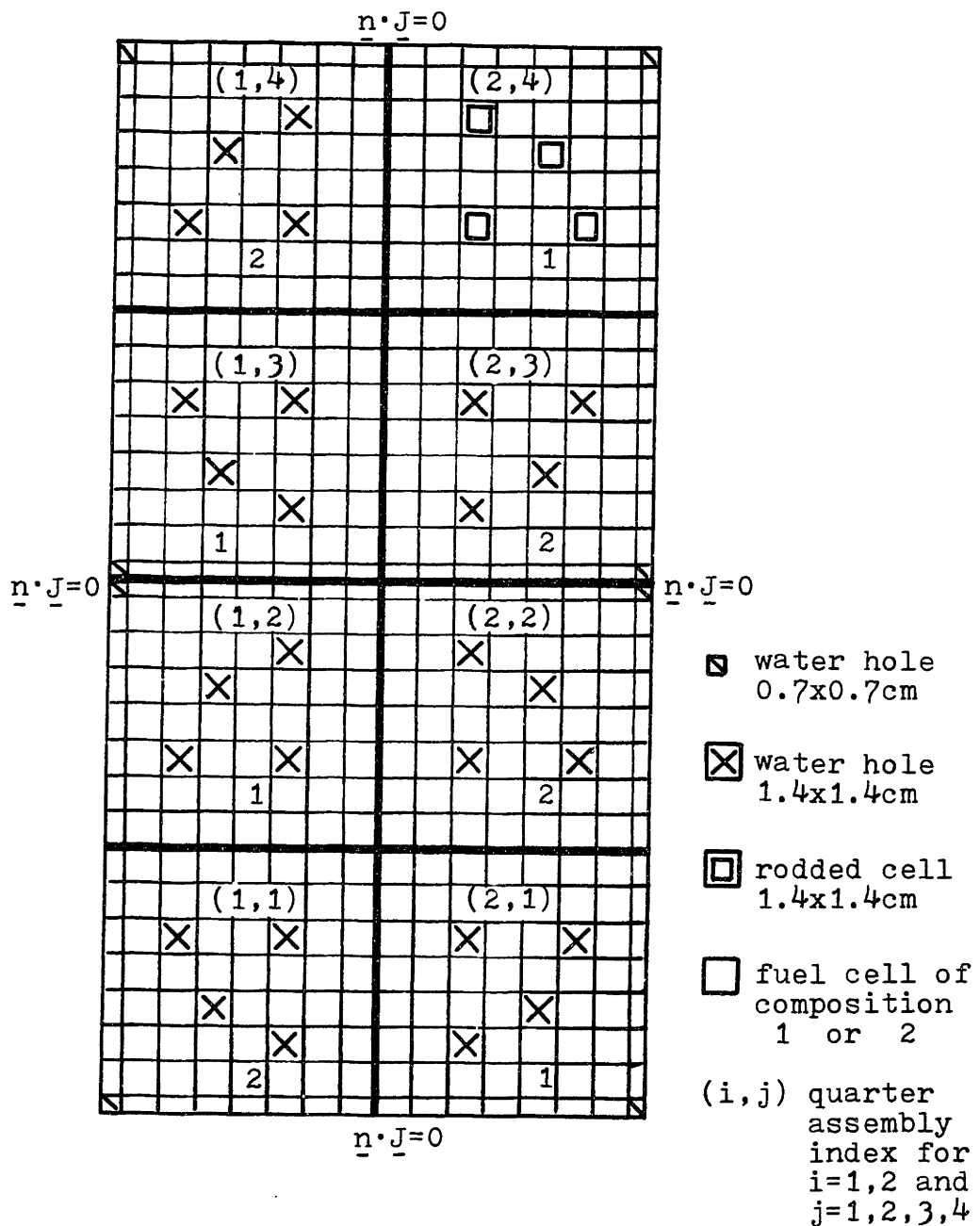


Figure A3.1 The 16 x 32 mesh layout of rodded plane of the CC3-PWR model. Zero net-current boundary conditions are imposed.

Table A3.2 Flux-Weighted Cross Sections and Radial Discontinuity Factors for the CC3-PWR (16 X 32 mesh calculation result).

(a) node layout for the CC3-PWR

• water reflector

17	17
17	17
17	17
17	17

• unrodded lower plane (node 8 is unrodded)

7	8
5	6
3	4
1	2

• rodded upper plane (node 16 is rodded)

15	16
13	14
11	12
9	10

Table A3.2 (continued)

(b) flux-weighted cross sections and radial discontinuity factors

node	D_1	Σ_{t_1}	Σ_{12}	$v\Sigma_{f_1}$	Σ_{f_1}
	D_2	Σ_{t_2}	Σ_{21}	$v\Sigma_{f_2}$	Σ_{f_2}
	f_1^{x-}	f_2^{x-}	f_1^{x+}	f_2^{x+}	
	f_1^{y-}	f_2^{y-}	f_1^{y+}	f_2^{y+}	
1	1.5133 0.39508	0.030449 0.14128	0.021123 0.0	0.0046258 0.16431	0.0018503 0.065724
	1.0015 1.0015	0.97534 0.97534	1.0032 1.0032	0.93344 0.93344	
2	1.51340 0.39508	0.033226 0.16866	0.021128 0.0	0.0060113 0.219070	0.0024045 0.087628
	1.0034 1.0012	0.93384 0.96777	1.0012 1.0034	0.96769 0.93384	
3	1.5134 0.39508	0.033226 0.16866	0.021128 0.0	0.0060113 0.219070	0.0024045 0.087628
	1.0012 1.0034	0.96770 0.93384	1.0034 1.0012	0.93384 0.96769	
4	1.5133 0.39508	0.030449 0.14128	0.021123 0.0	0.0046258 0.16431	0.0018503 0.065724
	1.0032 1.0032	0.93344 0.93344	1.0014 1.0014	0.97534 0.97534	
5	1.5134 0.39508	0.033226 0.16866	0.021128 0.0	0.0060113 0.219070	0.0024045 0.087628
	1.0012 1.0012	0.96770 0.96769	1.0034 1.0034	0.93384 0.93384	
6	1.5133 0.39508	0.030449 0.14128	0.021123 0.0	0.0046258 0.16431	0.0018503 0.065724
	1.0032 1.0014	0.93344 0.97534	1.0014 1.0032	0.97534 0.93344	
7	1.5133 0.39508	0.030449 0.14128	0.021123 0.0	0.0046258 0.16431	0.0018503 0.065724
	1.0015 1.0032	0.97534 0.93344	1.0032 1.0015	0.93344 0.97534	

Table A3.2 (continued)

node	D_1	Σ_{t_1}	Σ_{12}	$v\Sigma f_1$	Σf_1
	D_2	Σ_{t_2}	Σ_{21}	$v\Sigma f_2$	Σf_2
	f_1^{x-}	f_2^{x-}	f_1^{x+}	f_2^{x+}	
	f_1^{y-}	f_2^{y-}	f_1^{y+}	f_2^{y+}	
8	1.51340 0.39508	0.033226 0.16866	0.021128 0.0	0.0060113 0.219070	0.0024045 0.087628
	1.0034 1.0034	0.93384 0.93384	1.0012 1.0012	0.96769 0.96770	
9	1.51330 0.39507	0.03045 0.14127	0.021125 0.0	0.004625 0.164280	0.001850 0.065713
	1.0015 1.0015	0.97544 0.97485	1.0032 1.0032	0.93332 0.93344	
10	1.5134 0.39506	0.033226 0.16864	0.02113 0.0	0.0060102 0.21902	0.0024041 0.087608
	1.0035 1.0012	0.93377 0.96760	1.0012 1.0034	0.96818 0.93333	
11	1.51340 0.39508	0.033225 0.16867	0.021127 0.0	0.0060118 0.219090	0.0024047 0.087637
	1.0015 1.003	0.96667 0.93365	1.0032 1.0017	0.93370 0.96813	
12	1.51330 0.39509	0.030448 0.14130	0.021120 0.0	0.0046266 0.164330	0.0018507 0.065733
	1.0035 1.0036	0.93370 0.93367	1.0012 1.001	0.97412 0.97541	
13	1.51350 0.39504	0.033227 0.16858	0.021135 0.0	0.0060082 0.218920	0.0024033 0.087569
	1.0011 1.0008	0.96854 0.96692	1.0034 1.0037	0.93336 0.93345	
14	1.5134 0.39504	0.030452 0.14121	0.02113 0.0	0.0046235 0.164190	0.0018494 0.065674
	1.0044 1.0018	0.93481 0.97426	1.0011 1.0028	0.97860 0.93071	

Table A3.2 (continued)

node	D_1	Σt_1	Σ_{12}	$v\Sigma f_1$	Σf_1
	D_2	Σt_2	Σ_{21}	$v\Sigma f_2$	Σf_2
	f_1^{x-}	f_2^{x-}	f_1^{x+}	f_2^{x+}	
	f_1^{y-}	f_2^{y-}	f_1^{y+}	f_2^{y+}	
15	1.5133 0.39506	0.03045 0.14125	0.021124 0.0	0.0046253 0.16424	0.0018501 0.065696
	1.0013 1.0048	0.97413 0.93518	1.0035 1.0008	0.93100 0.97783	
16	1.46590 0.38329	0.036478 0.20765	0.018956 0.0	0.0060297 0.229860	0.0024119 0.091943
	1.0147 1.0149	1.1253 1.1252	1.0123 1.0116	1.1691 1.1688	
17	1.7 0.35	0.036 0.05	0.035 0.0	0.0 0.0	0.0 0.0
	1.0 1.0	1.0 1.0	1.0 1.0	1.0 1.0	

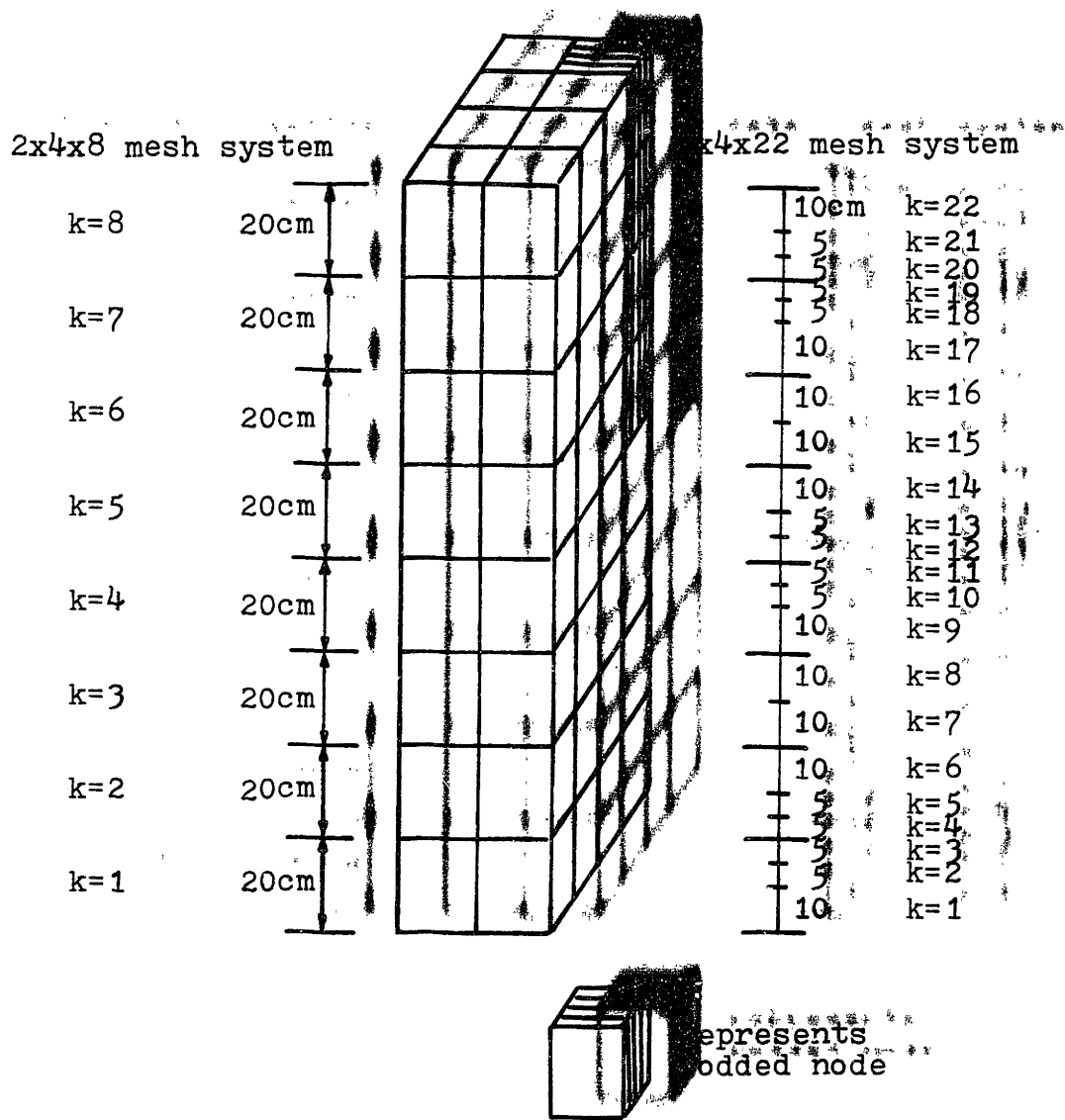


Figure A3.2 Axial mesh layout used to test unity axial dimensionless factors for the CC3-PWR benchmark problem.

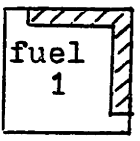
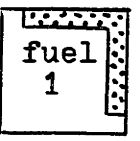
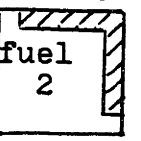
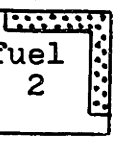
Table A3.3 Comparison of Nodal Power Densities from QUANDRY Solutions for the $2 \times 4 \times 8$ and $2 \times 4 \times 22$ Mesh Systems with Unity Axial Discontinuity Factors.

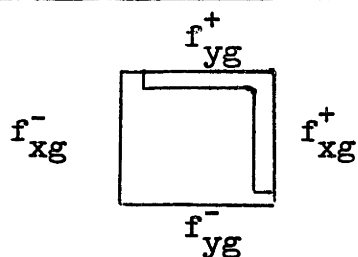
k	(i, j)	(1,1)	(1,2)	(1,3)	(1,4)	(2,1)	(2,2)	(2,3)	(2,4)	2x4x22 difference
7	0.4587	0.5276	0.4688	0.3358	0.5589	0.4286	0.3659	0.2916	0.03%	
	0.4586	0.5276	0.4688	0.3358	0.5589	0.4286	0.3659	0.2915		
6	0.9056	1.0451	0.9349	0.6741	1.1020	0.8500	0.7298	0.5801	0.947122 0.947133 0.0012%	
	0.9056	1.0450	0.9349	0.6741	1.1020	0.8500	0.7298	0.5801		
5	1.2533	1.4670	1.3503	1.0048	1.5257	1.1951	1.0631	0.8975	0.947122 0.947133 0.0012%	
	1.2533	1.4670	1.3503	1.0048	1.5257	1.1951	1.0631	0.8975		
4	1.3844	1.6546	1.5985	1.2707	1.6868	1.3548	1.3004	1.5085	0.947122 0.947133 0.0012%	
	1.3844	1.6546	1.5985	1.2707	1.6868	1.3548	1.3004	1.5085		
3	1.1830	1.4315	1.4160	1.1522	1.4419	1.1742	1.1610	1.4031	0.947122 0.947133 0.0012%	
	1.1830	1.4315	1.4160	1.1523	1.4419	1.1742	1.1611	1.4031		
2	0.6638	0.8077	0.8040	0.6566	0.8102	0.6617	0.6587	0.8013	0.947122 0.947133 0.0012%	
	0.6638	0.8077	0.8041	0.6566	0.8103	0.6617	0.6587	0.8013		

Appendix 4

CROSS SECTIONS AND MESH LAYOUT FOR BWR MODELS

Table A4.1 AXS and ADF for the 3 x 3 x 3 CISE Model.

assembly type AXS and ADF	unrodded 	rodded 	unrodded 	rodded 
\bar{D}_1	1.8440	1.8580	1.8440	1.8580
$\bar{\Sigma}_{t1}$	0.02481	0.02576	0.02482	0.02576
$\bar{\Sigma}_{21}$	0.01864	0.01772	0.01874	0.01772
$v\bar{\Sigma}_{f1}$	0.004556	0.004565	0.003796	0.003804
\bar{D}_2	0.4284	0.4283	0.4284	0.4283
$\bar{\Sigma}_{t2}$	0.05946	0.07416	0.05946	0.07415
$\bar{\Sigma}_{12}$	0.0	0.0	0.0	0.0
$v\bar{\Sigma}_{f2}$	0.07254	0.07558	0.06595	0.06870
f_{x1}^+	0.9623	1.0150	0.9625	1.0160
f_{x2}^-	1.4510	1.8880	1.4510	1.8890
f_{x1}^+	0.9623	0.8955	0.9625	0.8949
f_{x2}^+	1.4510	0.6492	1.4510	0.6488
f_{y1}^-	0.9623	1.0150	0.9625	1.0160
f_{y2}^-	1.4510	1.8880	1.4510	1.8890
f_{y1}^+	0.9623	0.8955	0.9625	0.8949
f_{y2}^+	1.4510	0.6492	1.4510	0.6488



$$v = 2.5$$

$$\bar{\Sigma}_{tg} = \bar{\Sigma}_{ag} + \bar{\Sigma}_{gg},$$

$$x_1 = 1.0$$

$$x_2 = 0.0$$

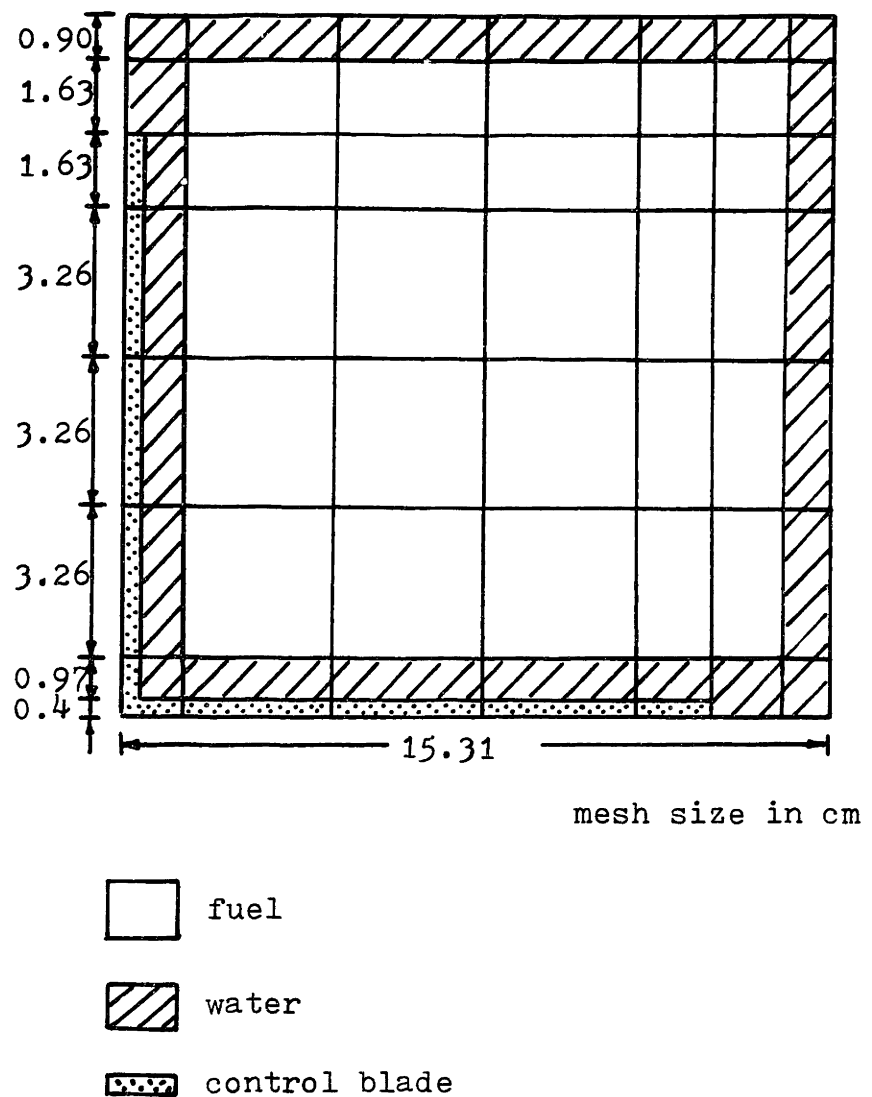


Figure A4.1 Heterogeneous quarter assembly of the TRD-BWR model (8 X 8 mesh layout).

Table A4.2 Heterogeneous, Two-Group Cross Sections
for the TRD-BWR Model (v = void fraction).

(a) for unrodded assemblies

material & void fraction, v	group g	D_g (cm)	Σt_g (cm $^{-1}$)	$\Sigma gg'$ (cm $^{-1}$)	$v\Sigma f_g$ (cm $^{-1}$)
fuel, v= 0 %	1	1.417	0.02618	0.01696	0.005983
	2	0.3696	0.07986	0.0	0.1019
fuel, v=40 %	1	1.696	0.01883	0.01015	0.005715
	2	0.5276	0.07658	0.0	0.09909
fuel, v=70 %	1	1.696	0.01443	0.005739	0.005694
	2	0.5262	0.07688	0.0	0.1006
water, v=0 %	1	1.531	0.03131	0.03074	0.0
	2	0.2942	0.00916	0.0	0.0
water, v=40 %	1	1.610	0.02827	0.02772	0.0
	2	0.3166	0.00855	0.0	0.0
water, v=70 %	1	1.610	0.02826	0.02771	0.0
	2	0.3167	0.008547	0.0	0.0

$$v = 2.5$$

$$\Sigma t_g = \Sigma_{ag} + \Sigma_{gg'}$$

$$x_1 = 1.0$$

$$x_2 = 0.0$$

Table A4.2 (continued)

(b) for rodded assemblies

material & void fraction, v	group g	D _g (cm)	Σt _g (cm ⁻¹)	Σ _{gg'} (cm ⁻¹)	vΣf _g (cm ⁻¹)
fuel, v=0 %	1	1.406	0.02596	0.01667	0.005963
	2	0.3735	0.08025	0.0	0.1048
control blade, v=0%	1	1.113	0.08742	0.00375	0.0
	2	0.1840	0.9673	0.0	0.0
water, v=0%	1	1.523	0.02685	0.02625	0.0
	2	0.3123	0.008559	0.0	0.0

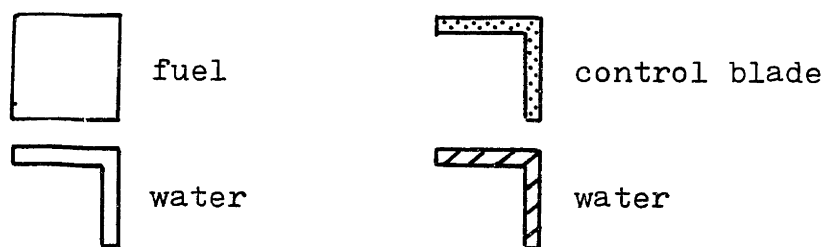
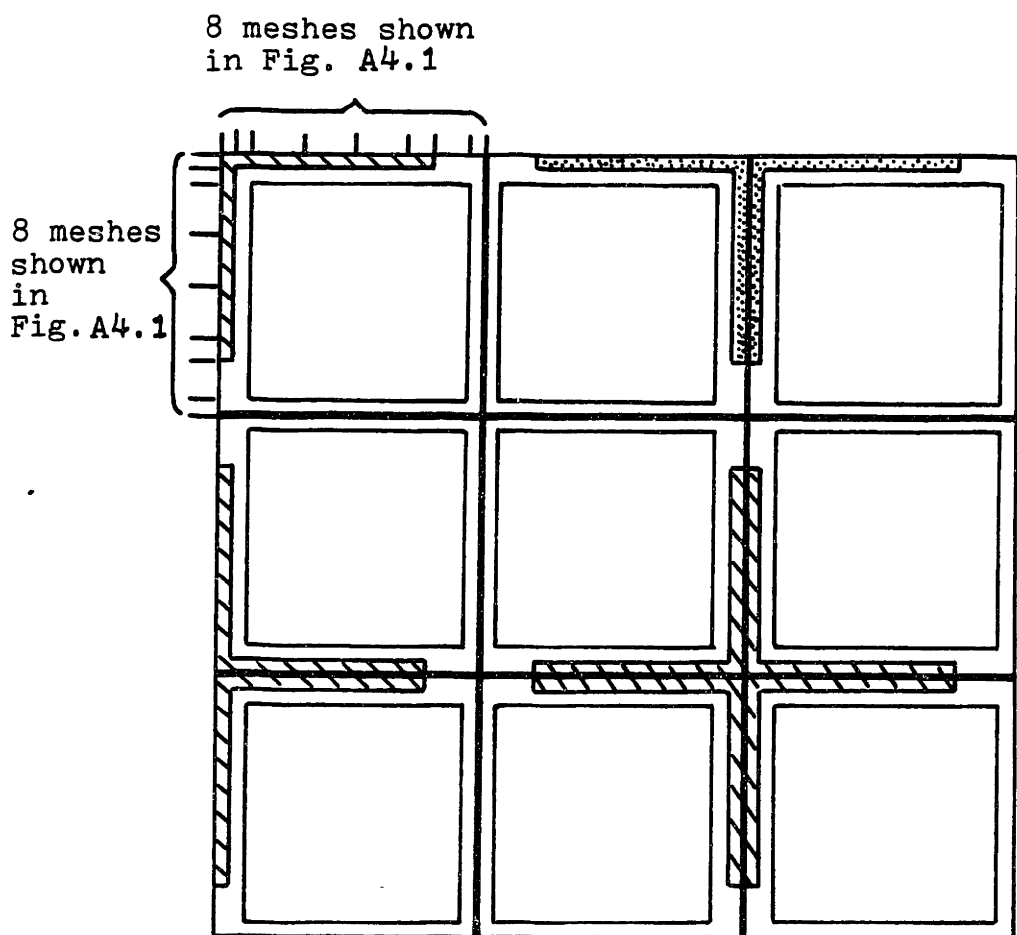


Figure A4.2 Horizontal section of the TRD-BWR model (24 X 24 mesh layout).

Table A4.3 FWC and ADF of Nodes of the TRD-BWR Model.
 FWC and ADF are Found from Two-Dimensional
 24 X 24 Fine-Mesh Calculations.

(a) node index system and node-wise void fractions for
 3 X 3 planes

	node index			void fraction (%)		
region 4	7	8	9	70	70	70
	4	5	6	70	70	70
	1	2	3	70	70	70
region 3	16	17	18	70	40	40
	13	14	15	70	70	70
	10	11	12	70	70	70
region 2 (unrodded)	25	26	27	40	0	0
	22	23	24		40	40
	19	20	21		40	40
region 2 (rodded)	34	35	36	40	40	40
	31	32	33		40	40
	28	29	30		40	40
region 1	43	44	45	0	0	0
	40	41	42	0	0	0
	37	38	39	0	0	0
water reflector	46	46	46			
	46	46	46			
	46	46	46			

Table A4.3 (continued)

(b) flux-weighted cross sections and radial discontinuity factors

node	D_1	Σ_{t_1}	Σ_{12}	$v\Sigma f_1$	Σf_1
	D_2	Σ_{t_2}	Σ_{21}	$v\Sigma f_2$	Σf_2
	f_1^{x-}	f_2^{x-}	f_1^{x+}	f_2^{x+}	
	f_1^{y-}	f_2^{y-}	f_1^{y+}	f_2^{y+}	
1	1.6722 0.41695	0.018110 0.049814	0.011585 0.0	0.0041791 0.060754	0.0016716 0.024301
	0.95219 0.97922	1.70600 1.32020	0.97920 0.95219	1.32020 1.70600	
2	1.6722 0.41695	0.018110 0.049814	0.011585 0.0	0.0041791 0.060754	0.0016716 0.024301
	0.97920 0.97921	1.32020 1.32020	0.95219 0.95219	1.70600 1.70600	
3	1.6722 0.41695	0.018110 0.049814	0.011585 0.0	0.0041791 0.060754	0.0016716 0.024301
	0.95217 0.97921	1.70600 1.32020	0.97921 0.95217	1.32020 1.70590	
4	1.6722 0.41695	0.018110 0.049814	0.011585 0.0	0.0041791 0.060754	0.0016716 0.024301
	0.95219 0.95218	1.70600 1.70590	0.97919 0.97920	1.32020 1.32020	
5	1.6722 0.41695	0.018110 0.049814	0.011585 0.0	0.0041791 0.060754	0.0016716 0.024301
	0.97919 0.95217	1.32020 1.70590	0.95218 0.97919	1.70590 1.32020	
6	1.6722 0.41695	0.018110 0.049814	0.011585 0.0	0.0041791 0.060754	0.0016716 0.024301
	0.95218 0.95219	1.70600 1.70600	0.97921 0.97920	1.32020 1.32020	
7	1.6722 0.41695	0.018110 0.049814	0.011585 0.0	0.0041791 0.060754	0.0016716 0.024301
	0.95219 0.97920	1.70600 1.32020	0.97920 0.95219	1.32020 1.70600	

Table A4.3b (continued)

node	D_1	Σt_1	Σ_{12}	$v\Sigma f_1$	Σf_1
	D_2	Σt_2	Σ_{21}	$v\Sigma f_2$	Σf_2
	f_1^{x-}	f_2^{x-}	f_1^{x+}	f_2^{x+}	
	f_1^{y-}	f_2^{y-}	f_1^{y+}	f_2^{y+}	
8	1.6722 0.41695	0.018110 0.049814	0.011585 0.0	0.0041791 0.060754	0.0016716 0.024301
	0.97920 0.97920	1.32020 1.32020	0.95219 0.95219	1.70590 1.70600	
9	1.6722 0.41695	0.018110 0.049814	0.011585 0.0	0.0041791 0.060754	0.0016716 0.024301
	0.95218 0.97920	1.70500 1.32020	0.97921 0.95219	1.32020 1.70500	
10	1.6722 0.41691	0.018113 0.049802	0.011589 0.0	0.0041779 0.060736	0.0016712 0.024295
	0.95230 0.97941	1.70530 1.31960	0.97933 0.95233	1.32020 1.70500	
11	1.6722 0.41688	0.018114 0.049791	0.011591 0.0	0.0041773 0.060719	0.0016709 0.024288
	0.97929 0.97935	1.31920 1.31870	0.95233 0.95241	1.70530 1.70530	
12	1.6722 0.41690	0.018113 0.049797	0.011590 0.0	0.0041776 0.060729	0.0016711 0.024291
	0.95228 0.97940	1.70540 1.31890	0.97928 0.95241	1.32010 1.70500	
13	1.6722 0.41699	0.018108 0.049827	0.011583 0.0	0.0041796 0.060773	0.0016718 0.024309
	0.95234 0.95230	1.70820 1.70850	0.97916 0.97909	1.31810 1.31880	
14	1.6722 0.41694	0.018107 0.049811	0.011580 0.0	0.0041802 0.060749	0.0016721 0.024299
	0.97943 0.95263	1.31790 1.70330	0.95179 0.97783	1.69260 1.30820	

Table A4.3b (continued)

node	D_1	Σt_1	Σ_{12}	$v\Sigma f_1$	Σf_1
	D_2	Σt_2	Σ_{21}	$v\Sigma f_2$	Σf_2
	f_1^{x-}	f_2^{x-}	f_1^{x+}	f_2^{x+}	
	f_1^{y-}	f_2^{y-}	f_1^{y+}	f_2^{y+}	
15	1.6723 0.41700	0.018104 0.049829	0.011575 0.0	0.0041816 0.060775	0.0016726 0.024310
	0.95181 0.95268	1.69580 1.70640	0.97915 0.97763	1.31640 1.30630	
16	1.6722 0.41690	0.018108 0.049800	0.011582 0.0	0.0041797 0.060732	0.0016719 0.024293
	0.95275 0.97934	1.70330 1.31760	0.97786 0.95180	1.30690 1.69300	
17	1.6722 0.42339	0.021342 0.051454	0.014826 0.0	0.0041940 0.062493	0.0016776 0.024997
	0.98077 0.98072	1.26150 1.26190	0.95059 0.95050	1.56420 1.56420	
18	1.6723 0.42336	0.021338 0.051447	0.014818 0.0	0.0041966 0.062483	0.0016786 0.024993
	0.95088 0.98080	1.56220 1.26090	0.97921 0.95000	1.25690 1.55630	
19	1.6722 0.42316	0.021342 0.051385	0.014824 0.0	0.0041946 0.062392	0.0016778 0.024957
	0.95113 0.97958	1.55490 1.25340	0.97953 0.95115	1.25360 1.55450	
20	1.6722 0.42313	0.021342 0.051377	0.014826 0.0	0.0041942 0.062380	0.0016777 0.024952
	0.97953 0.97957	1.25310 1.25270	0.95111 0.95115	1.55490 1.55520	
21	1.6722 0.42314	0.021342 0.051381	0.014825 0.0	0.0041945 0.062386	0.0016778 0.024955
	0.95112 0.97961	1.55490 1.25290	0.97952 0.95118	1.25350 1.55470	

Table A4.3b (continued)

node	D_1	Σ_{t_1}	Σ_{12}	$v\Sigma_{f_1}$	Σ_{f_1}
	D_2	Σ_{t_2}	Σ_{21}	$v\Sigma_{f_2}$	Σ_{f_2}
	f_1^{x-}	f_2^{x-}	f_1^{x+}	f_2^{x+}	
	f_1^{y-}	f_2^{y-}	f_1^{y+}	f_2^{y+}	
22	1.6722 0.42317	0.021339 0.051389	0.014820 0.0	0.0041959 0.062397	0.0016784 0.024959
	0.95112 0.95110	1.55790 1.55840	0.97921 0.97915	1.25120 1.25140	
23	1.6723 0.42292	0.021337 0.051313	0.014815 0.0	0.0041975 0.062287	0.0016790 0.024915
	0.97952 0.95182	1.25220 1.55030	0.95010 0.97667	1.54380 1.24430	
24	1.6723 0.42292	0.021335 0.051313	0.014812 0.0	0.0041987 0.062288	0.0016795 0.024915
	0.94999 0.95185	1.54740 1.55380	0.97923 0.97630	1.25040 1.24210	
25	1.6723 0.42289	0.021337 0.051306	0.014816 0.0	0.0041972 0.062277	0.0016789 0.024911
	0.95188 0.97947	1.55060 1.25190	0.97670 0.95008	1.24340 1.54430	
26	1.4455 0.33816	0.027539 0.054208	0.020610 0.0	0.0043981 0.064928	0.0017592 0.025971
	0.97888 0.97885	1.26470 1.26510	0.94140 0.94142	1.52230 1.52230	
27	1.4454 0.33804	0.027536 0.054103	0.020602 0.0	0.0044016 0.064777	0.0017606 0.025911
	0.94222 0.97886	1.51760 1.26440	0.97577 0.94026	1.25540 1.51520	
28	1.6724 0.42347	0.021327 0.051478	0.014798 0.0	0.0042033 0.062527	0.0016813 0.025011
	0.94991 0.97827	1.55720 1.25750	0.97888 0.94979	1.25320 1.55680	

Table A4.3b (continued)

node	D_1	Σt_1	Σ_{12}	$v\Sigma f_1$	Σf_1
	D_2	Σt_2	Σ_{21}	$v\Sigma f_2$	Σf_2
	f_1^{x-}	f_2^{x-}	f_1^{x+}	f_2^{x+}	
	f_1^{y-}	f_2^{y-}	f_1^{y+}	f_2^{y+}	
29	1.6724 0.42373	0.021320 0.051556	0.014785 0.0	0.0042074 0.062641	0.0016829 0.025056
	0.97900 0.97838	1.25850 1.25940	0.94957 0.94928	1.55630 1.55810	
30	1.6724 0.42358	0.021324 0.051512	0.014792 0.0	0.0042051 0.062577	0.0016820 0.025031
	0.94974 0.97812	1.55640 1.25970	0.97942 0.94930	1.25420 1.55780	
31	1.6722 0.42280	0.021344 0.051279	0.014829 0.0	0.0041930 0.062238	0.0016772 0.024895
	0.94900 0.94898	1.55310 1.55310	0.97977 0.98074	1.25180 1.24730	
32	1.6723 0.42308	0.021338 0.051362	0.014819 0.0	0.0041965 0.062358	0.0016786 0.024943
	0.98479 0.95069	1.27340 1.55890	0.94200 0.97824	1.51920 1.22990	
33	1.6721 0.42249	0.021354 0.051184	0.014848 0.0	0.0041869 0.062099	0.0016748 0.024839
	0.94150 0.94880	1.51680 1.55270	0.98695 0.98126	1.26750 1.22970	
34	1.6723 0.42337	0.021331 0.051450	0.014804 0.0	0.0042011 0.062487	0.0016804 0.024995
	0.94951 0.98620	1.55950 1.27630	0.97836 0.94114	1.23830 1.51610	
35	1.4189 0.35003	0.028145 0.072035	0.018446 0.0	0.0044063 0.074694	0.0017625 0.029878
	1.03690 1.03710	1.63730 1.63600	0.85475 0.85736	0.52648 0.52804	

Table A4.3b (continued)

node	D_1	Σt_1	Σ_{12}	$\nu \Sigma f_1$	Σf_1
	D_2	Σt_2	Σ_{21}	$\nu \Sigma f_2$	Σf_2
	f_1^{x-}	f_2^{x-}	f_1^{x+}	f_2^{x+}	
	f_1^{y-}	f_2^{y-}	f_1^{y+}	f_2^{y+}	
36	1.4180 0.34988	0.028278 0.072626	0.018414 0.0	0.0043954 0.074730	0.0017582 0.029892
	0.86186 1.04570	0.54074 1.67180	1.05110 0.83965	1.65800 0.46131	
37	1.4452 0.33801	0.027527 0.054073	0.020577 0.0	0.0044126 0.064733	0.0017650 0.025893
	0.94006 0.97453	1.51390 1.25670	0.97510 0.94009	1.25250 1.51450	
38	1.4451 0.33811	0.027522 0.054169	0.020566 0.0	0.0044176 0.064872	0.0017670 0.025949
	0.97524 0.97475	1.25780 1.25930	0.93948 0.93971	1.51270 1.51550	
39	1.4452 0.33805	0.027525 0.054115	0.020572 0.0	0.0044149 0.064794	0.0017660 0.025917
	0.93953 0.97445	1.51240 1.25920	0.97562 0.93986	1.25350 1.51590	
40	1.4455 0.33773	0.027538 0.053827	0.020608 0.0	0.0043991 0.064378	0.0017596 0.025751
	0.93936 0.93926	1.50870 1.50790	0.97621 0.97711	1.25200 1.24710	
41	1.4455 0.33790	0.027537 0.053977	0.020604 0.0	0.0044011 0.064595	0.0017604 0.025838
	0.98053 0.94013	1.26910 1.51740	0.93315 0.97838	1.48850 1.23870	
42	1.4457 0.33766	0.027547 0.053767	0.020631 0.0	0.0043891 0.064292	0.0017557 0.025717
	0.93186 0.93875	1.48090 1.51020	0.98386 0.98138	1.26690 1.23900	

Table A4.3b (continued)

node	D_1	Σt_1	Σ_{12}	$v\Sigma f_1$	Σf_1
	D_2	Σt_2	Σ_{21}	$v\Sigma f_2$	Σf_2
	f_1^{x+}	f_2^{x+}	f_1^{x+}	f_2^{x+}	
	f_1^{y+}	f_2^{y+}	f_1^{y+}	f_2^{y+}	
43	1.4453 0.33804	0.02751 0.054106	0.020585 0.0	0.0044033 0.064781	0.17829 0.025913
	0.9393 0.98180	1.51960 1.27190	0.97848 0.93184	1.24900 1.48450	
44	1.4189 0.34953	0.028129 0.070554	0.018444 0.0	0.0044109 0.073559	0.017544 0.029423
	1.03520 1.03510	1.57330 1.57140	0.85292 0.85606	0.53381 0.53529	
45	1.4180 0.34955	0.028280 0.071755	0.018414 0.0	0.0043952 0.074010	0.0017581 0.029604
	0.86153 1.04280	0.55650 1.60440	1.05180 0.84084	1.64330 0.45550	
46	2.010 0.3259	0.03569 0.009963	0.03516 0.0	0.0 0.0	0.0 0.0
	1.0 1.0	1.0 1.0	1.0 1.0	1.0 1.0	

Appendix 5

TEMPORAL TRUNCATION ERROR FOR THE CC3-PWR

Time step interval plays an important role in evaluating transient problem solutions. In Section 5.3.2, it was suggested that the time step size be less than 25 msec for a transient problem employing six delayed neutron groups to assure temporal stability. However, because the limit of time step sizes is strongly restricted by power rate during a transient, it is prudent to examine the temporal truncation error before a time step size is set for transient problems in Section 5.5 of Chapter 5. For the test, the delayed neutron data given in Table A5.1 was used.

The CC3-PWR (Fig. 5.1) was activated to remove the control rod from $z = 100$ cm to $z = 120$ cm for 0.1 sec. The control rod was withdrawn 2 cm per 10 msec step by step as shown in Fig. A5.1. The period of 10 msec was then divided into 2, 4 and 8 fine intervals (i.e., 5, 2.5 and 1.25 msec). Four different time step sizes were tried to predict total reactor power for a 2 X 4 X 17 mesh CC3-PWR which had 10 fine meshes within a plane extended from $z = 100$ to $z = 120$ cm. The results are summarized in Table A5.2. The fluctuations in power levels from different time steps (ranging from 1.25 msec

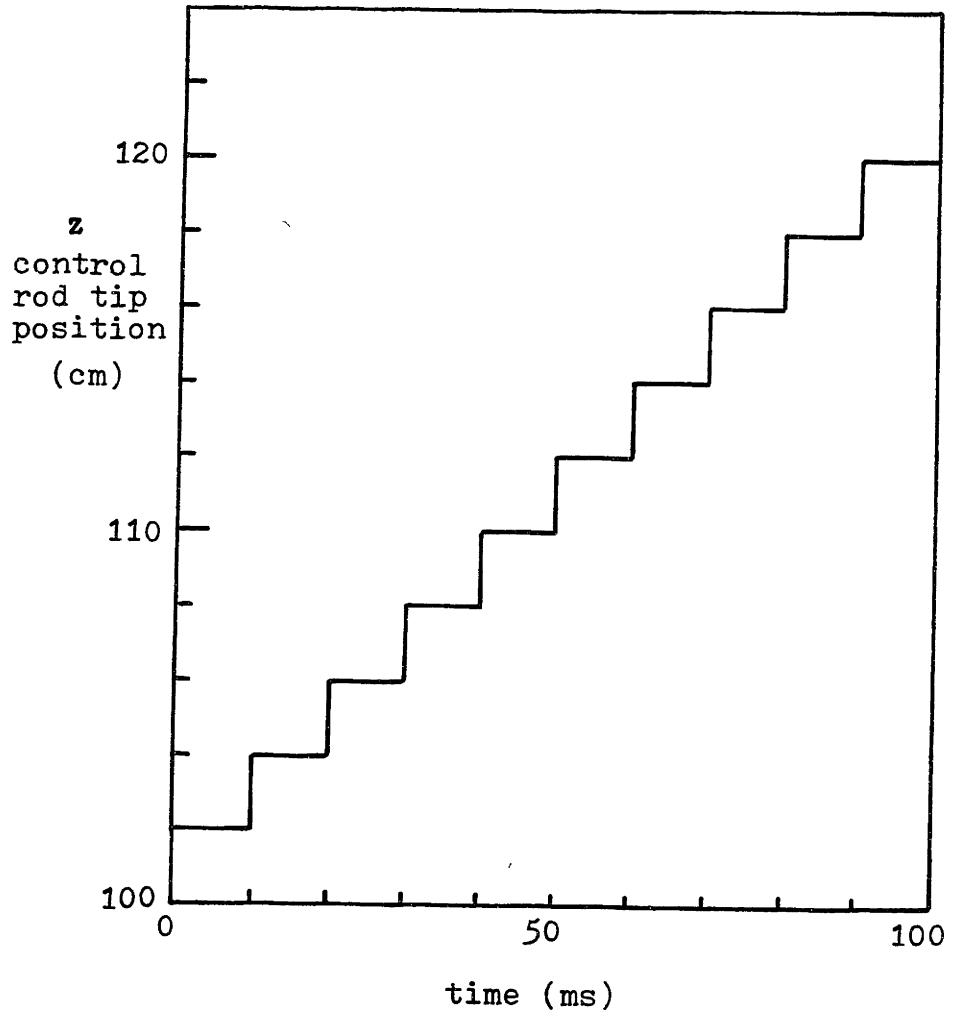


Figure A5.1 Control rod tip position (z) vs. time steps for 2 X 4 X 17 CC3-PWR mesh system.

to 10 msec) remain within 2%, and decrease almost linearly as time step size decreases. Thus, it seems to be reasonable to set the time step at 10 msec for the transient problem in Chapter 5.

Also, for a direct justification of use of 10 msec as a time step size for the CC3-PWR, a 2.5 msec time step size was chosen to solve the same CC3-PWR problem in Section 5.5.3. Because the axial node extended from $z = 100$ cm to $z = 120$ cm contains now 40 time steps, the node was sliced into forty very thin planes to create

Table A5.1 Delayed-Neutron Data [L-2].

group, d	decay constant, λ_d (sec ⁻¹)	yield β_d
1	0.0127	0.000247
2	0.0317	0.0013845
3	0.115	0.001222
4	0.311	0.0026455
5	1.4	0.000832
6	3.87	0.000169

$$v_1 = 1.25 \times 10^7 \text{ cm/sec}$$

$$v_2 = 2.5 \times 10^5 \text{ cm/sec}$$

Table A5.2 Comparison of Total Power Transient for CC3-PWR for Different Time Step Sizes. A 2 X 4 X 17 Mesh System was Used.

Δt t(ms)	1.25 ms	2.5 ms	5.0 ms	10 ms
0	100.0 W	100.0 W	100.0 W	100.0 W
10	108.63	108.36 (-0.25)	107.84 (-0.73)	106.63 (-1.8)
20	119.20	118.80 (-0.34)	118.09 (-0.93)	117.05 (-1.8)
30	131.35	130.89 (-0.35)	130.04 (-1.0)	128.79 (-1.9)
40	145.28	144.75 (-0.36)	143.82 (-1.0)	142.45 (-1.9)
50	161.30	160.71 (-0.37)	159.69 (-1.0)	158.15 (-2.0)
60	179.74	179.08 (-0.37)	178.02 (-0.96)	176.54 (-1.8)
70	201.03	200.32 (-0.35)	199.25 (-0.89)	197.96 (-1.5)
80	225.67	224.92 (-0.33)	223.89 (-0.79)	222.56 (-1.4)
90	254.46	253.69 (-0.30)	252.64 (-0.72)	250.94 (-1.4)
100	288.35	287.63 (-0.25)	286.26 (-0.72)	283.81 (-1.6)
computing time (sec)	70.5	42.5	28.5	21.9

Percent error is given in parenthesis.

Table A5.3 Comparisons of Total Power for CC3-PWR Transient for Time Step = 2.5 msec. Withdrawal Rate = 0.5 cm/2.5 msec (percent error in parenthesis).

time (ms)	fine mesh 2x4x4? standard	VWC 2x4x8	quadratic axial flux 2x4x8	Method 1 2x4x8	Method 2M 2x4x8	Method 2Q 2x4x8	Method 2J 2x4x8
0	100.0 W	100.0 W	100.0 W	100.0 W	100.0 W	100.0 W	100.0 W
10	107.59 (-3.41)	104.55 (-2.8)	106.41 (-1.4)	106.19 (-1.3)	106.43 (-1.1)	106.94 (-0.6)	106.94 (-0.6)
20	117.66 (-9.62)	111.34 (-5.4)	115.39 (-1.3)	115.82 (-1.6)	116.45 (-1.0)	116.95 (-0.6)	116.95 (-0.6)
30	129.32 (-11.1)	119.39 (-7.7)	126.19 (-2.4)	127.39 (-1.6)	128.35 (-0.7)	128.93 (-0.3)	128.93 (-0.3)
40	142.73 (-14.1)	128.78 (-9.8)	138.49 (-3.0)	140.33 (-1.3)	142.19 (-0.4)	143.39 (+0.4)	143.39 (+0.4)
50	158.38 (-16.6)	132.04 (-11.6)	152.56 (-3.7)	155.45 (-1.8)	157.85 (-6.3)	160.33 (+1.2)	160.33 (+1.2)
60	176.68 (-18.6)	143.46 (-13.1)	168.82 (-4.4)	172.86 (-2.2)	175.81 (-5.5)	177.88 (-1.6)	177.88 (-1.6)
70	197.76 (-19.6)	159.05 (-13.9)	170.21 (-13.9)	182.78 (-5.0)	192.91 (-2.5)	196.84 (-0.8)	193.81 (-2.0)
80	222.07 (-19.3)	179.29 (-13.8)	191.44 (-5.4)	210.47 (-2.7)	219.44 (-1.2)	216.24 (-2.6)	216.24 (-2.6)
computing time (sec)	174.6	17.7	18.0	19.3	19.2	19.3	19.7

a 2 X 4 X 47 node system for a reference solution calculation. Solutions from six different methods along with the reference solution are summarized in Table A5.3. We notice that the error distribution in 2.5 msec solutions are almost identical to those in 10 msec solutions given in Table 5.9, and that Method 2 demonstrates its consistency and reliability. Also note the computing time taken in reference solution and in Method 2 (175 sec vs. 19.5 sec).